# Mesoscopic Aspects of Solid Friction

Vom Fachbereich Physik
der Universität Duisburg–Essen
(Campus Duisburg)

zur Erlangung des akademischen Grades eines
Doktors der Naturwissenschaften
genehmigte Dissertation

von

**Guido Bartels**

aus Moers

Referent: Prof. Dr. D. E. Wolf
Korreferent: Prof. Dr. P. Entel

Tag der Einreichung: 29. September 2005
Tag der mündlichen Prüfung: 23. Januar 2006

# Abstract

The phenomenon of friction is on the one hand useful, for example for walking, which would not be so easy without friction, and on the other hand disturbing, for example in wheel bearings, where it slows down desired motion. Therefore, the origin and effect of friction is under intense research.

One main point in this work is the analytic investigation of the coupling between friction force and (torsion) friction torque of a sliding and spinning disk. The local friction force at a contact area element was chosen to be an algebraic function of the local relative velocity with an exponent $\alpha > 0$. It could be shown, that for $\alpha < 1$ sliding and torsion friction dynamically reduce each other, while for $\alpha > 1$ they amplify each other. In case of $\alpha = 1$ sliding and torsion friction are decoupled.

With respect to the velocity ratio of sliding and angular velocity, the final motion mode has been investigated, i.e. whether both motions stop together or whether one motion gets dominant. For $\alpha < 1$ both motions stop together, while for $\alpha > 1$ it depends on the initial velocity ratio.

The mass distribution and contact area radius, which are encoded in the key parameter $C$ of the corresponding differential equation, are the second important influence on the final motion mode. A "phase diagram" shows for given values $C$ and $\alpha$ the possible final motion modes.

The influence of an inhomogenous pressure distribution within the contact area on the coupling was investigated exemplarily for $\alpha = 0$ with a cylinder as object. In contrast to the disk (homogenous pressure distribution) the cylinder is deflected from its initial sliding direction. In this context the motion of a curling rock on ice is discussed, as it is deflected towards the opposite direction compared to that of the cylinder.

Another focal point is the investigation of the role of friction torques (rolling and torsion friction) in the compaction of nano-powders. For this three dimensional contact dynamics simulations with phenomenologically chosen contact laws were performed. With this it could be shown that torsion and rolling friction contribute significantly to the final porosity. Furthermore, these contributions of torsion and rolling friction are independent of each other and can be represented by a sum.

In the chapter "Conclusions and Outlook" a brief introduction on recent research of atomic scale torsion friction is presented.

# Zusammenfassung

Das Phänomen der Reibung ist einerseits nützlich, z.B. beim Laufen, welches ohne Reibung nicht so einfach möglich wäre, andererseits ist sie aber in manchen Bereichen störend, z.B. in Radlagern, wo sie erwünschte Bewegung "ausbremst". Die Ursache und Wirkung von Reibung ist Gegenstand intensiver Forschung.

Einen Schwerpunkt in dieser Arbeit bildet die analytische Untersuchung der Kopplung zwischen Gleit- und Torsionsreibung einer gleitenden und drehenden Scheibe. Dazu wurde ein Reibungsgesetz gewählt, bei dem die Reibung an einem Kontaktflächenelement eine algebraische Funktion der lokalen Relativgeschwindigkeit mit Exponent $\alpha > 0$ ist. Es zeigte sich, dass sich Gleit- und Torsionsreibung für $\alpha < 1$ gegenseitig verringern, während sie sich für $\alpha > 1$ gegenseitig verstärken. Im Falle von $\alpha = 1$ sind Gleit- und Torsionsreibung entkoppelt.

Mit Hilfe des Geschwindigkeitsverhältnisses zwischen Gleit- und Drehgeschwindigkeit wurde der finale Bewegungsmodus untersucht, d.h. ob die Scheibe beide Bewegungen gleichzeitig stoppt, oder ob eine der beiden Bewegungsarten dominieren wird. Während für $\alpha < 1$ beide Bewegungen gleichzeitig zum Stillstand kommen, hängt der finale Bewegungsmodus für $\alpha > 1$ vom anfänglichen Geschwindigkeitsverhältnis ab. Die Massenverteilung und der Kontaktradius, welche in dem Parameter $C$ der entsprechenden Differentialgleichung enthalten sind, sind der zweite wichtige Einfluss auf den finalen Bewegungsmodus. Ein "Phasendiagramm" zeigt für gegebene Werte $C$ und $\alpha$ die möglichen finalen Bewegungsmoden.

Der Einfluss einer inhomogenen Druckverteilung in der Kontaktfläche auf die Kopplung wurde exemplarisch für $\alpha = 0$ anhand eines Zylinders untersucht. Im Gegensatz zur Scheibe (homogene Druckverteilung) wird der Zylinder von seiner ursprünglichen Gleitrichtung abgelenkt. In diesem Zusammenhang wird die Bewegung eines Curling Steins auf Eis diskutiert, welcher verglichen mit dem Zylinder in die entgegengesetzte Richtung abgelenkt.

Einen anderen Schwerpunkt bildet die Untersuchung des Einflusses von Torsions- und Rollreibung auf die Kompaktierung von Nano-Pulvern. Dazu wurden dreidimensionale Kontakt-Dynamik Simulationen mit phänomenologisch gewählten Kontaktgesetzen durchgeführt. Es zeigte sich, dass die Torsions- und Rollreibung signifikante Beiträge zur Porosität nach der Verdichtung liefern. Diese Porositätsbeiträge sind jeweils unabhängig voneinander und tragen additiv zur bei der Kompaktierung erreichten Porosität bei.

Im Kapitel "Ausblick und Zusammenfassung" wird ein kurzer Überblick über aktuelle Forschung von Torsionsreibung auf atomarer Ebene vorgestellt.

# Contents

# List of Figures

# List of Tables

# Chapter 1

# Introduction

*"In short, the study of sliding friction, which is one of the oldest problems in physics, is in a phase of rapid and exciting development."*

B.N.J. Persson, 1996 [1]

## 1.1 Friction

Friction plays an important part in life: Without friction it would not be possible to walk or drive a car on the street. Music instruments, like guitars or violins, would not produce sound, while even high friction is desired in braking systems. Carefully noted, friction was not unimportant in the development of civilization: No fire without rubbing woods or flints. But (high) friction can also be disturbing. For example in high-tech components such as computer storage and recording systems, miniature motors or aerospace devices, low-friction surfaces are desired [2]. Already Leonardo da Vinci constructed ball bearings to minimize friction. In fact, there sliding friction is substituted by rolling friction, which is usually lower. Or one can think of combustion motors, where oil provides as lubricant low friction between piston and cylinder. These examples show that there is a need for understanding friction and its origin, not only for practical but also for fundamental reasons. The study of friction is one topic covered by tribology, which is the science and technology of interacting surfaces in relative motion. The word "tribology" is based upon the Greek word "tribos", meaning rubbing [2]. Tribology covers not only the study of friction, but also that of lubricants, lubrication, bearings and wear. A large number of books on tribology and friction have

been published and the REFS. [2–7] are giving a good introduction to this field. A brief historical review on friction will be given in CHAP. 2.

From a general point of view, friction can be defined as a resistive force that acts between two bodies and tends to oppose and damp out relative motion between them. Usually one can distinguish between static friction, which is a frictional force opposing setting a body at rest into relative motion, and dynamic friction, which means the frictional force that damps out the relative motion. In general, the force needed to set a resting body into relative motion, that means overcoming the static friction force, is larger than the force needed to keep a body in motion, i.e. static friction is larger than dynamic friction.

Sliding friction forces are nonconservative and transform part of the mechanical energy into heat, i.e. they dissipate energy. For dry, flat surfaces sliding over each other it is found empirically that the friction force is proportional to the load and independent of the (apparent) contact area, relative sliding velocity and surface roughness [1].

How can this empirical friction law for macroscopic bodies be explained and can it be derived from fundamental atomic principles? Can one observe the macroscopic friction laws also on the microscopic or nanoscopic scale? Macroscopic bodies seen on the micrometer length scale show usually many asperities due to their surface roughness. These asperities can have extents at the nanometer length scale. In fact, when two macroscopic bodies slide relatively to each other, they interact via these asperities and the observed macroscopic friction is considered as the sum of the frictional effects occurring at all these asperities. This relation between macroscopic effect and microscopic origin is the reason why the study of frictional properties of a single asperity on a surface is paid notable attention. This field of tribology, called *nanotribology*, has grown fast in the last years theoretically and experimentally. One important experimental development was the atomic force microscope (AFM) in 1986 [8, 9], which allows to detect frictional forces on the length scale of atomic dimensions. For an overview of further experimental techniques see for e.g. REFS. [2, 9].

On the theoretical side, the rapid increase in computational power within the last decades made it possible to simulate atomic scale systems with a large number of atoms, so that single asperities sliding on a substrate could be modeled and compared with experimental results. On the nanoscale, where

[1] The roughness of surfaces show little effect on the friction force, except when they are perfectly smooth or extremely rough [2].

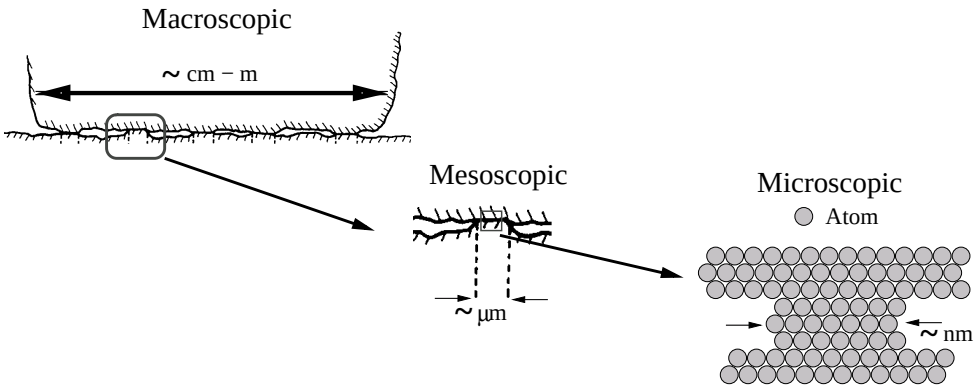


Figure 1.1: This illustration shows exemplarily different length scales on which friction is commonly investigated.

the surface-to-volume ratio is high, the old, simple macroscopic friction laws are inadequate and, conventional tribological and lubrication techniques used on the macroscopic scale can not easily be transferred to the nanoscale. This is relevant for many technological nanodevices. Recent advances in research have shown the enormous complexity of even simple tribological processes at the nanoscale [9]. In Fig. 1.1 different length scales are sketched on which friction is commonly investigated.

Not only the origin of friction is investigated, but also its effects are of interest, for example in a collective arrangement of particles or the frictional coupling between different degrees of freedom of relative motion. In cartesian space the relative motion, for example of two solid spheres, has three translational and three rotational degrees of freedom. The translational degrees of freedom are characterized by a velocity vector with one normal component (deformation mode) and two tangential components (sliding mode), while the three rotational ones are characterized by an angular velocity vector, again with one normal component (spinning mode) and two tangential components (rolling mode). On the one hand the viscoelastic dissipation mechanism of normal restitution couples the deformation and rolling mode [10, 11] and on the other hand the sliding and spinning mode are coupled due to dissipation of sliding and torsion friction [12], where torsion friction means dissipation of the spinning mode.

Sliding friction and incomplete normal restitution are normally the main dissipation mechanisms at the contact between two solid particles. Therefore, rolling and torsion friction are indispensable for a unified view of the dissipation mechanisms at the contact of two (viscoelastic) spheres. The reason,

why torsion friction is often neglected, is that it involves the radius of the contact area between the two spheres and hence is small compared to the other dissipation mechanisms.
But in case of a flat disk sliding and spinning on a flat surface, torsion friction can not be neglected, which has significant influence on the dynamics of the disk, which will be shown in Chap. 3. In this context friction with an inhomogeneous stress distribution inside the contact area is considered. These stresses are not resolved atomistically, but described by means of continuum mechanics. This means, that here friction is considered on a mesoscopic scale.

Friction plays also a crucial role in the compaction of granular packings or (nano-)powders consisting of many single particles. It helps to stabilize the packing against the external pressure by damping (dynamic friction) and hindering (static friction) relative motion of contacting particles. Therefore, packings are possible, which have a large free volume between the particles (high porosity packings). As the influence of rolling and torsion friction is commonly regarded as negligible, they have been much less investigated so far. However, it turns out that in certain situations they may become crucial, for instance for the stabilization of pores in cohesive powders [13–15]. The powder as a many particle system is considered to be macroscopical and the single particles and contacts between them are considered as mesoscopic, as they are not resolved atomistically.

## 1.2 Outline of this thesis

This thesis is organized as follows. In Chap. 2 a brief historical review on macroscopic dry friction laws is given, and the difference between apparent and real area of contact (Bowden and Tabor approach) is explained. Further the velocity dependence of dry friction and hydrodynamic friction is introduced.

That friction also provides (nontrivial) interesting phenomena on the macroscopic scale is shown in this thesis by discussing the frictional coupling between the two relative motions of sliding and spinning, which is the topic of Chap. 3: For a sliding and spinning disk the sliding friction force and friction torque are calculated. The local friction force of each contact area surface element have a power-law dependence on the local relative velocity, which is the superposition of sliding and spinning velocity. The dynamic effect of the frictional coupling is discussed in terms of final motion modes of the disk.

The differences a sliding and spinning cylinder shows compared to the disk is also discussed exemplarily for velocity independent friction. The chapter closes with a review on the recent research in the physics of ice curling and a summary.

The effect of friction torques (rolling and torsion friction) on the stability of nano-packings under uniaxial compression is the main concern of CHAP. 4. After a short introduction to cohesive granular media and nano-powders, a threshold model for the friction torques (rolling and torsion) in case of nano-particles is presented. The basics of contact dynamics (CD), probably the most suitable simulation method for this case, are described. Finally, the simulation results of uniaxially compacted ballistic deposits are discussed.

In the closing chapter "Outlook and Conclusions" (CHAP. 5) additionally a brief description of ongoing research on atomic-scale torsion friction is given.

# Chapter 2

# Friction

In this chapter a short historical review of the macroscopic dry friction law, namely the daVinci-Amontons-Coulomb friction law, is given, which in literature is also often referred to as Coulomb's dry friction law. One central statement of this law is the independence of dry friction of the (apparent) contact area. Further, dry friction is often assumed to be velocity independent, which is true for steady sliding. For rather low velocities the friction force undergoes so called velocity weakening and strengthening, which is also shortly presented. In contrast to dry friction, wet friction is introduced, where a liquid film separates the contact areas of two objects. Wet friction is usually velocity dependent.

## 2.1 Brief historical review on macroscopic dry friction

The first recorded systematic and quantitative studies about friction come from Leonardo da Vinci (1452-1519) in the time of the Renaissance. From experiments with a block on horizontal and inclined planes he found fundamental properties of friction. Some sketches of his experiments are shown in Fig. 2.1. He formulated his results as follows: [2]:

- "The friction made by the same weight will be of equal resistance at the beginning of its movement although the contact may be of different breadths and lengths."

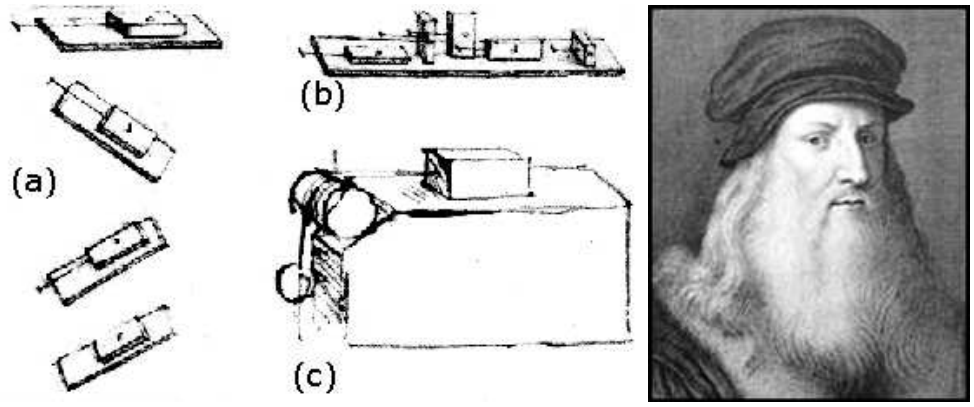


Figure 2.1: A portrait of Leonardo da Vinci (right) and sketches of his experiments (left) he performed to determine a) the force of friction in case of horizontal and inclined planes, b) the influence of the (apparent) contact area on the friction force and c) the force of friction on a horizontal plane by means of a pulley. The sketches are taken from "Codex Atlanticus" and "Codex Arundel" [2] .

- "Friction produces double the amount of effort if the weight be doubled."

In summary, the frictional resistance is proportional to the load and independent of the (apparent) sliding area. Leonardo da Vinci defined a coefficient of friction, $\mu$, which is the ratio of the frictional resistance and the weight of the slider (load). From his experiments he found a *universal* value of 1/4 for polished and smooth surfaces: "every friction body has a resistance of friction equal to one-quarter of its weight". Afterwards it was learned, that no universal coefficient of friction exists. But one can explain how Leonardo could come to such a conclusion if the materials used, e.g. in bearings, at that age are considered. Because for these materials the value of 1/4 for the coefficient of friction is a typical one.

Leonardo da Vinci's two statements are referred to as the first two laws of friction, which are often attributed to Guillaume Amontons (1663-1705). Nearly two hundred years after da Vinci's observations, the French physicist Amontons investigated friction and postulated [16]:

- The resistance caused by rubbing only increases or diminishes in proportion to greater or lesser pressure (load) and not according to the greater or lesser extent of the surfaces.

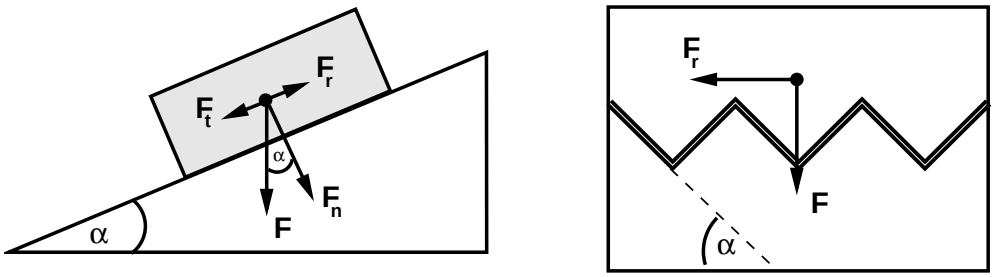


Figure 2.2: On the left a sketch of the inclined plane with relevant forces is shown, while on the right Euler's idea of the origin of static friction due to interlocking asperities is illustrated.

- The resistance caused by rubbing is more or less the same for iron, lead, copper and wood in any combination if the surfaces are coated with pork fat
- The resistance is more or less equal to one-third of the pressure (load).

His first statement validates the results of da Vinci, i.e. the two first laws of friction. From his second statement one can assume that Amontons investigated (surface) lubricated friction as well. The third statement shows that he believed in the existence of a universal friction coefficient $\mu$ like da Vinci, but with a value of 1/3.
The statements of da Vinci and Amontons make no clear distinction between the frictional resistance of *setting* a resting body into relative motion or *keeping* a sliding body in relative motion.

This distinction was first made by Leonhard Euler (1707-1783). He considered a block on an inclined plane on which a force $\mathbf{F}$ due to gravity acts, see Fig. 2.2. From purely geometrical aspects he derived a relation between the inclination angle and friction coefficient $\mu$: The plane is inclined to a critical angle $\alpha$ just before the block starts to move. The force tangential to the plane, $\mathbf{F}_t$, trying to accelerate the block is still completely compensated by the friction force $\mathbf{F}_r(= -\mathbf{F}_t)$. Together with the load (which is here the normal force value $|\mathbf{F}_n|$) and the definition of $\mu$ as ratio of friction force and load (as proposed by da Vinci) Euler got:

$$\left.\begin{aligned} |\mathbf{F}_r| &= |\mathbf{F}| \sin\alpha \\ |\mathbf{F}_n| &= |\mathbf{F}| \cos\alpha \end{aligned}\right\} \mu = \frac{|\mathbf{F}_r|}{|\mathbf{F}_n|} = \tan\alpha$$

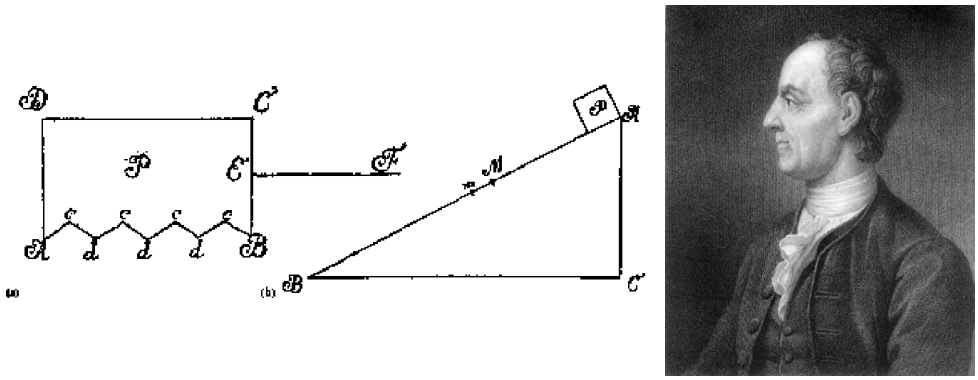

Figure 2.3: A portrait of Leonhard Euler (right) and sketches of his model for static friction (left) [17].

Assuming that $\mu$ does not depend on the velocity and that the plane is inclined to an inclination angle which is just a little bit larger than $\alpha$, then the block should start to slide with a certain velocity. But in experiments it is observed, that the block starts to slide with a larger velocity than expected. Euler solved this problem by distinguishing between static and dynamic friction. The force needed to set a body into relative motion is larger than that to keep it in relative motion. That means, that once the block has started its motion, it experiences a smaller resistance (dynamic friction). Static and dynamic friction exist for a block on a horizontal plane as well. For the static friction Euler developed a "microscopic" model of the contact area. It is illustrated in FIG. 2.2 and an original sketch together with a portrait of Euler is shown in FIG. 2.3.

Euler thought, that due to microscopically rough surfaces the asperities of the block and plane are interlocked. A simple model would be to envisage these asperities as wedges whose edges have a slope of $\tan(\alpha)$ related to the horizontal. To initiate relative motion, the block has to be lifted over these wedges with a certain force against its weight, neglecting other forces of microscopic origin. Once it is in relative motion, the asperities do not interlock so deeply and a smaller force is needed to keep the relative motion. So Euler tried, nearly as the first, to explain the phenomenon of static and dynamic friction on a microscopic level. Bélidor modeled in 1737 rough surfaces as spherical asperities and obtained a value $\mu \approx 0.35$ [18], which is a typical experimental value and near to the value from Amontons (1/3).

Charles Augustin Coulomb (1736-1806) investigated friction in a wide range and had a similar imagination of microscopic interlocking as Euler, FIG. 2.4.

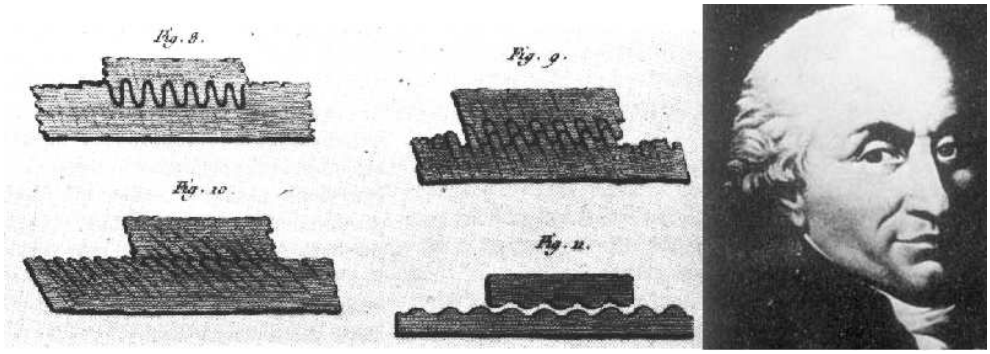


Figure 2.4: Illustrations of rough surfaces (1785) from C. A. Coulomb (Portrait at the right) . Pictures taken from [2, 20]

In several experiments he investigated factors which could influence the friction, like the normal pressure (load), the kind of materials and their surfaces, the area of contact, the time in stationary contact and environmental conditions like temperature and humidity. He expressed his main results in the following four statements, known as the *Coulomb's law of friction* [16] [1]:

- For wood sliding on wood under dry conditions, the friction rises initially but soon reaches a maximum. Thereafter, the force of friction is essentially proportional to load."
- "For wood sliding on wood the force of friction is essentially proportional to load at any speed, but kinetic friction is much lower than the static friction to long periods of repose.
- For metals sliding on metals without lubricant the force of friction is essentially proportional to load and there is no difference between static and kinetic friction.
- For metals on wood under dry conditions the static friction rises very slowly with time of repose and might take four, five or even more days to reach its limit. With metal-on-metal the limit is reached almost immediately and with wood-on-wood it takes only one or two minutes. For wood-on-wood or metal-on-metal under dry conditions speed has very little effect on kinetic friction, but in the case of wood-on-metal the kinetic friction increases with speed.

[1] Coulomb published these results in the *Essai sur la theorie du frottement* [19]

In these statements the laws of da Vinci and Amontons are enclosed and the difference between static and kinetic (dynamic) friction, too. In the last statement Coulomb says, that the friction coefficient can be (nearly) velocity-independent (wood-on-wood, metal-on-metal) or velocity dependent (wood-on-metal). But Coulomb assumed that $\mu$ is generally independent of velocity as long as it is not too low or too high. He assumed further, that the friction coefficient is independent of the load and contact area. These assumptions made on $\mu$ are well known as *Coulomb's friction law*.

Defining now a static friction coefficient $\mu_s$ for the (maximal) static friction force $F_{\mathrm{s,max}}$ and a dynamic friction coefficient $\mu_d$ for the dynamic friction force $F_{\mathrm{d}}$, one can express Coulomb's law of friction as the following two equations:

$$\begin{aligned} F_{\mathrm{d}} &= -\operatorname{sgn}(v)\mu_d L \ , \\ |F_{\mathrm{s,max}}| &= \mu_s L \end{aligned}$$

with $L$ as load. The minus sign takes into account, that friction always acts in the opposite direction of the motion. If one relates the static and dynamic friction force to the relative sliding velocity $v$ one obtains the so called "Coulomb graph" shown one the left side in FIG. 2.5. On the right side in FIG. 2.5 the dependency of the static friction force on the time of stationary contact is displayed. Coulomb's experimental data fit very well to the function $F = A + B\ln(t)$. This relation has been shown to be of general validity [2]. More about historical findings on friction can be found in [2, 16, 21]

These macroscopic laws describe the phenomenon of dry friction in a wide range of material pairs. But the independence of the friction from the contact area seemed to be paradoxical: J.T. Desagulier found that polished smooth surfaces show increased friction compared to unpolished rougher surfaces, which is in contradiction to the model of interlocked asperities. A solution was the introduction of adhesion between the surfaces, but then the friction force should be proportional to the contact area.

It took some decades till this contradiction was solved by Bowden and Tabor around 1940. For understanding this a closer look at the contact area is necessary.

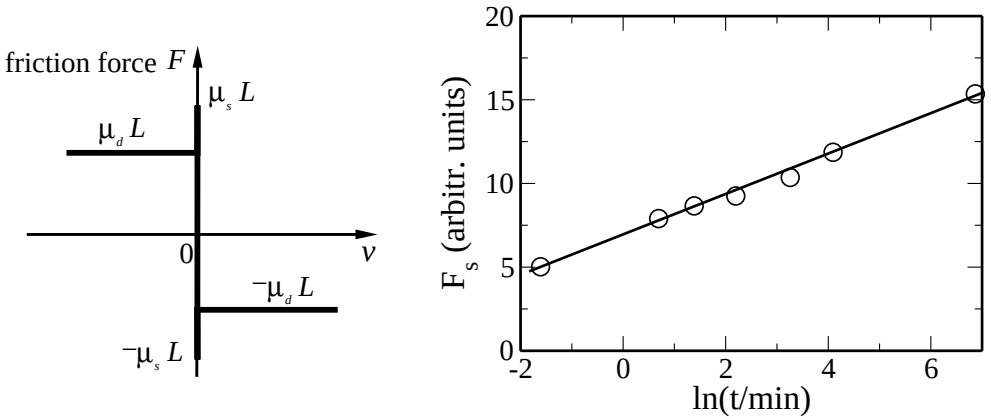


Figure 2.5: On the left the "Coulomb graph" is shown relating the maximal static friction force $|F_{\mathrm{s,max}}| = \mu_s L$ and the dynamic friction force $F_{\mathrm{d}} = \mu_d L$ to the relative sliding velocity $v$. On the right side the static friction force $F_s$ is displayed as function of the natural logarithm of the time in stationary contact (Data from [2]).

## 2.2 Area of contact: apparent and real

Usually solid macroscopic objects have rough surfaces, what appears at least on the microscopic scale. If two of such objects are brought into contact then at some regions surface atoms of one object touches the atom(s) of the other, while in other regions relatively large distances can lie between surface atoms. FIG. 2.6 shows a schematic view of the contact area between two solids. Different experimental techniques are used to get information about the surface topography: for e.g. the profilometer, scanning tunneling microscopy (STM) and atomic force microscopy (AFM) [2]. Usually the profilometer has a resolution at the micrometer scale, while STM and AFM allow resolution at the atomic scale (nanometer scale).
The diameter of regions in contact, often called junctions, are in most practical applications of the order of $\sim 10$ $\mu$m and the separation distance between non-contacting regions is $\sim 1$ $\mu$m. Due to the relatively large separation distance of the non-contact regions they play no role in determining the sliding friction. So, only the sum over all junctions as the real contact area $\Delta$A needs to be considered. Consider the following situation: As a block is lowered toward a substrate, somewhere within the apparent contact area a single junction is formed. The perpendicular pressure increases in that junction and leads to plastic deformation while the block lowers further and more junctions are formed which also deform plastically. The block lowers further

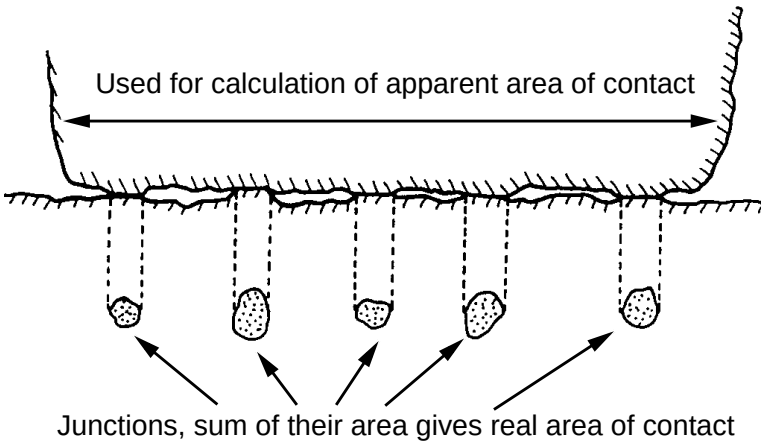


Figure 2.6: The difference of apparent and real area of contact is illustrated: the real area of contact is smaller than the apparent one (modified, original from [2]).

until the real area of contact $\Delta$A reaches a size where the load $L$ is balanced by the contact pressure integrated over $\Delta$A (contact forces) and no further plastic deformations at the junctions occur. Now it can be assumed, that every junction is in a state of incipient plastic flow, where the compressive stress is equal to the penetration hardness $\sigma_c$. This is the largest compressive stress a material can bear without plastic deformation (plastic yielding). Values of $\sigma_c$ can be obtained from indentation hardness tests, where a pyramid of very hard material (e.g. diamond) is pressed into a flat surface. The penetration hardness, or yield stress, is defined as $\sigma_c = L/\mathrm{A}$, where A is the measured impression area [2]. With this, one can now relate the load $L$ to the real contact area by

$$L = \sigma_c \Delta \mathrm{A} \tag{2.1}$$

To shear the junctions of area $\Delta$A tangentially a shear stress $\tau_c$, is needed, that means a force $F$ of

$$F = \tau_c \Delta \mathrm{A} \ .$$

Solving Eq. (2.1) for $\Delta$A and using this for the last equation gives:

$$F = \frac{\tau_c}{\sigma_c} L = \mu L, \qquad \text{with} \quad \mu = \frac{\tau_c}{\sigma_c}. \tag{2.2}$$

[2] This relation can be used to estimate the real area of contact: consider a steel cube of side 10 cm, that is brought in contact with a steel plane. $\sigma_c$ is for steel $10^9 \mathrm{N/m^2}$ [2] and the load is approx. $L = 100$ N, then $\mathrm{A} \sim 0.1\mathrm{mm}^2$, which is a fraction of $10^{-5}$ of the apparent area.

Finally, $F$ considered as friction force is proportional to the real area of contact, manifested in $\sigma_c$, but *not* to the apparent area of contact. Further, the proportionality of $F$ to the load $L$, found in Coulomb's friction law (and in Amontons' and da Vinci's as well) is established. As $\tau_c$ and $\sigma_c$ are of similar magnitude it follows that $\mu \sim 1$, which is a 1typical value for clean surfaces. This concept considers plastic deformations and works for most "natural" surfaces, but for very smooth surfaces the pressure in a large fraction of the junctions is below the penetration hardness $\sigma_c$ and it is expected, that the real area of contact is larger than predicted by $\Delta A = L/\sigma_c$. Furthermore, for a relatively small elastic deformation of a single spherical asperity (the contact radius $a$ is then much smaller than the radius of the spherical asperity) one can apply Hertzian contact mechanics, where the real contact area varies nonlinearly with the load, i.e. the contact radius $a$ is proportional to $L^{1/3}$ [22] and therefore $\Delta \mathrm{A} \propto L^{2/3}$. But Greenwood showed with a model calculation with elastic deformations of asperities, where the asperity height distribution is assumed to decrease fast for high asperities, that the area of real contact varies linearly with the load [23]. Thus, the equation Eq. (2.2) is valid for not too rough or too smooth surfaces. This holds for many practical cases and can be used for example for the calculation of the radius of the junctions [2]. It is worth noting that the discussion above applies for microscale junctions with diameters in the order of $\sim 10\mu m$. For nanoscale junctions, where the diameters of contact area are just a few atom radii, the physical processes of formation and their behavior are different.

## 2.3 Velocity dependence of friction

Coulomb's dry friction law states that friction is velocity independent, although Coulomb noticed a slight velocity dependence of the dynamic friction force. Furthermore, he noted a time dependence of the static friction force. The velocity dependence of dry, solid friction, which can be observed in experiments for small relative sliding velocities, will be briefly presented below.

A linear and quadratic velocity dependence of friction is derived with a dimensional analysis considering the frictional drag on a sphere in a fluid. Although the scenario of hydrodynamic friction is not considered in this work, it is introduced for reasons of completeness, as hydrodynamic friction is also present, if a fluid layer between two solid surfaces exists (wet friction).

This presentation of velocity dependence of friction is taken here as a motivation for the friction law introduced in the next Chap. 3, which velocity dependency is described by a power-law.

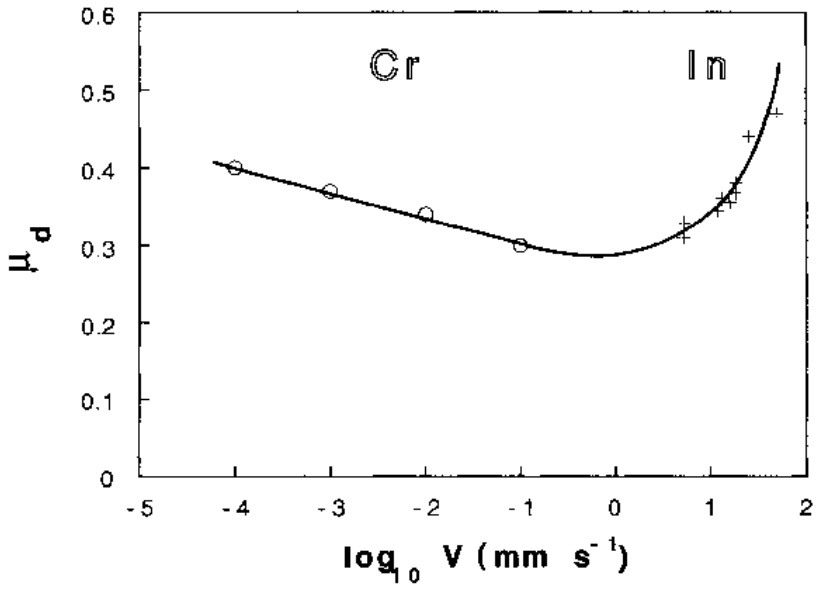


Figure 2.7: Dynamic friction coefficient $\mu_d$ vs. logarithm of pulling velocity in the steady sliding regime from experimental data (circles and crosses). The velocity weakening, decreasing $\mu_d$, and velocity strengthening, increasing $\mu_d$, of the dynamic friction coefficient can be seen. "Cr" and "In" are abbreviations for creep regime and inertial regime, respectively. The solid line is drawn as a guide for the eyes. (Taken from [24]). For further details see text.

### 2.3.1 Velocity dependence of dry friction

Heslot et al. studied dry-friction dynamics of a paper-on-paper system [24]. The experimental setup can be imagined (simplified) as a block, called slider, which bottom surface is covered with the paper, lying on a fixed paper surface. The block is connected to a spring, which free end moves with velocity $v$ parallel to the fixed paper surface. The paper used in the experiments is Bristol board of 2 mm strength, providing regular dynamical behavior over many periods of use [24]. In FIG. 2.7 the dynamic friction coefficient $\mu_d$ is shown as function of the logarithmic pulling velocity $v$ in the steady sliding regime, in which the slider (center of mass) moves steadily at the pulling velocity $v$, while in the so called stick-slip regime the motion of the slider is oscillatory. In FIG. 2.7 the velocity dependence of $\mu_d$ obtained from the experiments is displayed. The graph shows the *velocity weakening*, where

$\mu_d$ decreases approximately linearly with $\ln(v)$ over three decades, and the *velocity strengthening*, where $\mu_d$ increases linearly with $v$. The abbreviations "CR" and "IN" in FIG. 2.7 stand for creep regime and inertial regime, respectively. Heslot et al. [24] introduced a heuristic model which takes into account plastic relaxation of micro-contacts under load, where the static coefficient of friction $\mu_s$ increases logarithmically with the stick time $\tau_{stick}$, i.e. the time prior to the onset of sliding. Furthermore, a characteristic creep length $D_0$ was defined, which can be understood as an average sliding displacement needed to reset the micro-contacts. $D_0$ is also called *creep memory length* and for the paper-paper system it is found that $D_0 \approx 1\mu$m [25]. The model describes creep as noise-activated motion in a pinning potential, biased by the pulling force. If the pulling force increases and motion accelerates, the age of contacts decreases, which reduces the pinning strength. This leads to a so-called "self-acceleration" of the slider, where friction is reduced [24] and the velocity weakening in the creep regime, "CR", can be observed. For a larger pulling force the sliding velocity has become large enough, so that the system is considered as depinned enough to move quasifreely and crosses into the inertial regime, "IN", where a linear velocity dependendcy of friction is approached [24] and velocity strengthening is observed.

Despite these observations dry friction is usually considered (and often modeled in applications) as velocity independent.

With a dimensional analysis the frictional force acting on a sphere in a fluid will now be derived.

### 2.3.2 Hydrodynamic friction

Consider a sphere with radius $r$ moving at velocity $v$ through a fluid of density $\varrho$ and viscosity $\eta$. What is now the friction force $F$ exerted by the fluid on the sphere? With the given quantities one can define a dimensionless friction force $F/\varrho v^2 r^2$, which can only depend on the dimensionless parameter $R = \varrho v r/\eta$, thus:

$$F = \varrho v^2 r^2 f(R) \tag{2.3}$$

$R$ is the Reynolds number [2]. A critical Reynolds number, which depends on the geometry of the system, can be defined. If $R$ is much below that critical value the flow is laminar, while for much larger $R$ turbulent flow occurs. In fact, the Reynolds number is the relation between the inertia force $\varrho v^2 r^2$ and the viscous force $\eta v r$. Low Reynolds numbers mean, that the viscous force

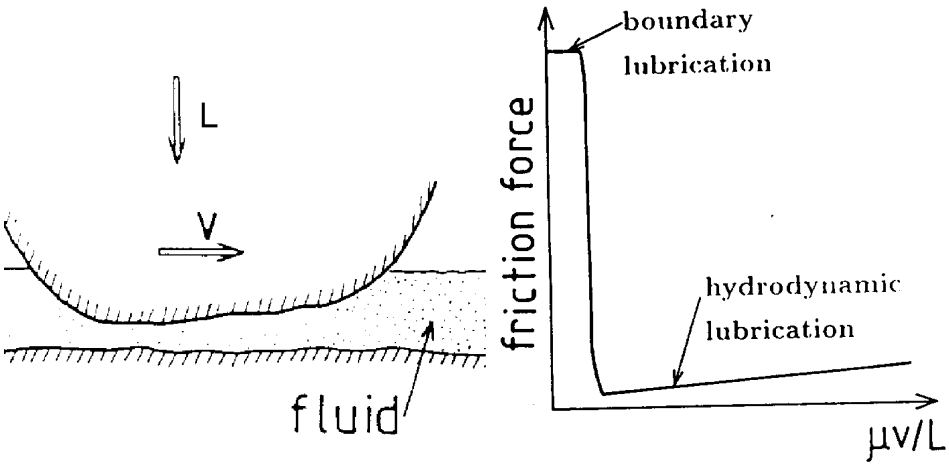


Figure 2.8: Left: A solid body is sliding with velocity $v$ on a lubricated surface. Right: The relation between the friction force and the parameter $\mu v/L$ containing $\mu$ as the viscosity, which is here rather denoted with $\eta$, the sliding velocity $v$ and the load $L$. (Sketches from [2]).

dominates, thus the friction force in Eq. (2.3) should not contain inertia effects.This can be achieved by a function of $f(R) = C_1/R$ in Eq. (2.3), thus

$$F = C_1 \eta v r \equiv F_{\text{viscous}} \ . \tag{2.4}$$

The friction force is independent of $\varrho$ and linear in $v$. On the other hand, for large Reynolds numbers, the flow is turbulent and the inertia force gets dominant, while the viscous force is negligible. Thus a constant function $f(R) = C_2$ gives a friction force

$$F = C_2 \varrho v^2 r^2 \equiv F_{\text{inertia}} \ ,$$

which is independent of $\eta$ and depends on the square of the velocity. For the derivation of hydrodynamic friction usually the Navier-Stokes equation is considered [2]. It allows to calculate the value for the constant $C_1$, giving $C_1 = 6\pi$. Using this value for $C_1$ in Eq. (2.4) the well known Stokes friction force is achieved [26].
A linear velocity dependence of the friction force can also be derived if a body sliding on a lubricated surface is considered. A sketch of this is shown on the left side in Fig. 2.8. On the right hand side the relation between friction force and sliding velocity is shown. The two regimes *hydrodynamic lubrication* and *boundary lubrication* are explained by considering the viscosity and velocity. Pushing two solid surfaces, which are separated by a fluid, together will

squeeze the fluid out of the contact area. This process can take a long time, if the viscosity is high. Is there a fast enough relative lateral motion of the two solid surfaces, the time to squeeze out the fluid completely will be insufficient. The separating fluid film remains relatively thick, which is the case of hydrodynamic lubrication with relatively low friction. The friction force is proportional to the velocity. For small relative velocity, the fluid film can be squeezed out till direct contact between the two solid surfaces occurs. This is the region of boundary lubrication where the friction is much higher (typically by a factor of 100 [1]) and velocity independent. While the hydrodynamic lubrication is quite well understood, boundary lubrication is not so well understood. Experiments show, that in boundary lubrication at most a few monolayers of lubrication molecules are present between the sliding surfaces and participate at the sliding process. The viscosity, which is the most important parameter for hydrodynamic lubrication, is irrelevant for boundary lubrication, where direct interactions between the solid interfaces and the molecules of the lubricant are important.

# Chapter 3

# Coupling of dynamic friction force and torque

## 3.1 Introduction

The coupling of friction force and torque constitutes an interesting phenomenon. Consider two identical disks which slide on a table with velocity $v$. Both are launched with the same initial velocity, but one of them is also spinning with angular velocity $\omega$. Will there be a difference in the distance travelled by the two disks? Yes, the spinning disk slides farther, because the spinning motion reduces the sliding friction (the sliding motion reduces the friction torque as well). An analytic proof will be given in this study.

Another interesting effect which can be observed, is that spinning and sliding motion stop at the same time, independent of the initial sliding and spinning velocity. For an ordinary table and disk one can assume that Coulomb friction applies and that the observed effects can be ascribed to the coupling of sliding and spinning motion via the friction force and torque. Voyenli and Eriksen discussed in Ref. [27] the coupled friction force and torque, but did not provide analytic closed expressions for the net friction force and torque. They defined the velocity ratio $\omega/v$ and showed on the basis of its time evolution, that it approaches unity for $v, \omega \to 0$ in case of a homogenous circular ring. For a homogenous disk they derived numerically that this ratio takes the value of approximately 1.53 just before the motion stops. Comparing the stopping times for both the ring and disk, they found that the stopping time of a purely rotating or purely translating ring or disk is smaller than for a

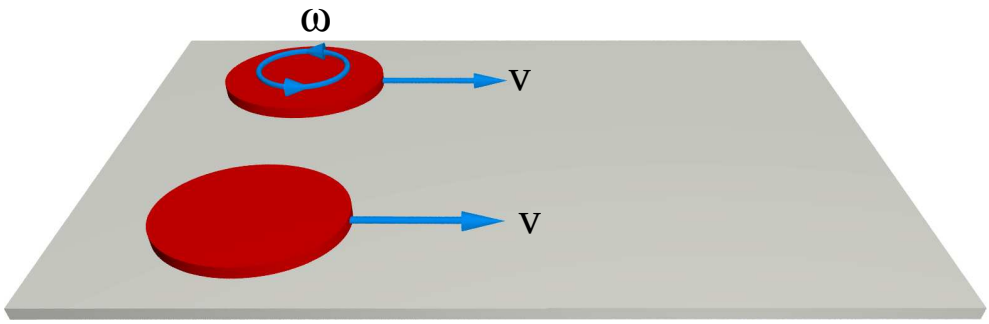


Figure 3.1: Two identical disks on a flat surface slide with the same initial velocity. One of the disks is spinning additionally. Do both disks travel the same distance or does one of the two disks travel farther?

sliding and spinning ring or disk. Therefore, the sliding *and* spinning ring or disk travels farther. Further, they showed that the translation of a sliding and spinning ring or disk is rectilinear and stated that this holds for all mass distributions which are rotationally symmetric.

Goyal and Ruina [28] used a geometric method based on the limit surface description of friction to describe the planar sliding and rotation of an object with dry friction [29]. The object can have arbitrary shape and thus is not restricted to circular geometry. Ref. [29] also discussed the final motion mode and for axisymmetric sliders found it to depend on the relation between its radius of pressure distribution and radius of gyration. Goyal and Ruina gave an example object where the radius of gyration can be easily changed while the pressure distribution radius is kept constant: a massless board mounted on top of a ring. On this board the mass (rotationally symmetrically) can be distributed at an arbitrary radius. The ratio between the radius of the ring (pressure distribution radius) and the radius of the distributed mass determines the final motion mode this object has. The three final motion modes are separated by certain values of that ratio. Goyal and Ruina derived the corresponding values for the examples of a ring and a disk as supporting object of the board [29]. In general, the final motion mode depends on the friction law used, the contact pressure distribution and the mass distribution of the object.

The final motion mode of an object is interesting for the so called *inverse sliding problem*. There, one wants to know how to push an object, so that it comes to rest in a certain desired way. A practical application of this problem is found in the research of robotics [30, 31].

Furthermore the static coupling of dynamic friction force and torque is of interest and is currently studied for dry friction. It was possible to show by experiments with discs and with an analytic model, that the static friction force is reduced if an external torque is also applied [32]. The analytic model, where a collective breaking of microbonds between slider and surface is assumed, fits the experimental data very well, while another model, where the sliding starts after the breaking of the weakest contact, fails to fit. The coupling between static friction force and torque is nontrivial and is not determined by the Coulomb friction law alone, but depends on the microscopic details of friction. Further, it seems that the macroscopic experiment reveals details about the microscopic processes lying behind friction [32]. The obtained results for the disc geometry are not restricted to such a geometry, as a tripod was investigated as well [33]. The microscopic processes relevant for the onset of sliding, i.e. the transition from static friction to dynamic friction, is currently under research, see e.g. Rubinstein et al. [34]. The coupling of static friction force and torque will not be considered in this study.

### Motivation

All the works mentioned above consider dry friction, i.e. they are based on the velocity independent Coulomb friction law.

In this chapter the coupling between friction force and friction torque is extended to a more general friction law, where the velocity depends on a power-law with power $\alpha \geq 0$. It is a purely phenomenological model neglecting the microscopic structure of the contact area and the origin of this velocity dependence. For deriving the net friction force and torque the following system is considered: a sliding and spinning disk on an (isotropic) plane surface, which provides a circular contact area. The pressure distribution is assumed to be uniform.

Dry Coulomb friction is included with $\alpha = 0$ and analytic closed expressions for the friction force and torque will be presented, which show the dynamical reduction of the friction force and torque. That section is based on the publication by Farkas et al. [12].

The net friction force and torque for $\alpha = 1$ (linear) and $\alpha = 3$ (cubic) are calculated and discussed explicitly. For general $\alpha > 0$ the net friction force and torque are calculated in the limit of fast sliding/slow spinning and fast spinning/slow sliding. With an autonomous differential equation for the velocity ratio $\varepsilon$, the final motion modes and the influence of mass distribution

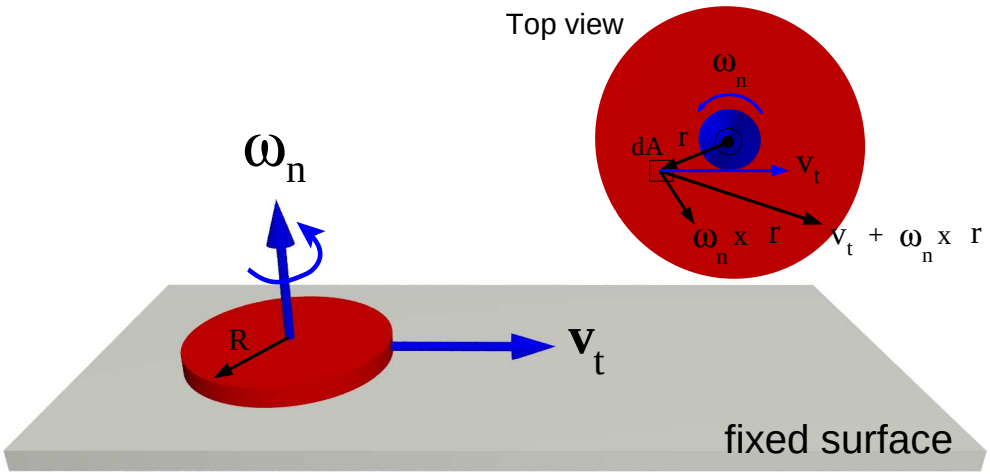


Figure 3.2: Schematic view of the disk system with relevant variables: a disk slides with velocity $\mathbf{v}_\mathrm{t}$ and angular velocity $\boldsymbol{\omega}_n$ on a plane. The top view of the contact area shows an example of the vectorial superposition of both velocities.

are discussed. This is first done explicitley for $\alpha = 0, 1, 3$ as introduction and after that for general $\alpha$. Finally a scheme is presented showing the stable and unstable (finite) fixed points for given mass distribution, moment of inertia and exponent $\alpha$.

Finally, the consequence of a nonuniform pressure distribution for the coupling is discussed by the example of a sliding and spinning cylinder, which shows a curved path in contrast to the disk with uniform pressure distribution. In this context, the motion of a curling rock on ice is interesting as it shows the opposite deviation from the sliding path as the cylinder. A summary of recently published experimental results and theoretical models to explain this phenomenon is given.

## 3.2 Sliding and spinning disk

The concept of coupling between friction force and friction torque is introduced by considering a simple model system: a rigid disk with radius $R$ slides on its flat side with velocity $\mathbf{v}_\mathrm{t}$ and rotates with angular velocity $\boldsymbol{\omega}_n$ on a plane. A sketch of this model system is shown in FIG. 3.2. The vector $\mathbf{n}$ is the normal of the contact area plane, while the tangential vector $\mathbf{t}$ is coplanar with that plane and its direction defined by the sliding velocity $\mathbf{v}_\mathrm{t}$. The macroscopic friction properties of Amontons' and da Vinci's friction

laws are considered here: the friction is independent of the contact area size and proportional to the load. Here the load is (only) the weight of the disk $Mg$, where $M$ is the mass of the disk and $g$ is the acceleration due to gravity, which direction shall be parallel to the normal vector $\mathbf{n}$. From here on the load is denoted as normal force value $F_\mathrm{n}$. With $F_\mathrm{n}$ and the contact area a pressure distribution can be defined:

$$P(F_\mathrm{n}, R_\mathrm{c}) = \frac{F_\mathrm{n}}{\pi R_\mathrm{c}^2} \ , \tag{3.1}$$

which is uniform. The effect of nonuniform pressure distributions will be discussed later in Sec. 3.5. The newly introduced contact area radius $R_\mathrm{c}$ is, for the case of the disk, equal to the disk radius $R$.
The relative velocity of each surface element $dA$ within the contact area $A$ is determined by the superposition of $\mathbf{v}$ and $\boldsymbol{\omega}_n$:

$$\mathbf{v} = \mathbf{v}_\mathrm{t} + \boldsymbol{\omega}_n \times \mathbf{r} \ , \tag{3.2}$$

where $\mathbf{r}$ is the vector pointing from the center to the surface element $dA$. For the calculation of the friction force and torque a coordinate system in the center of the contact area is defined. The sliding velocity $\mathbf{v}_\mathrm{t}$ is used to define the unit vector $\mathbf{e}_v$ and the angular velocity $\boldsymbol{\omega}_n$ for defining the unit vector $\mathbf{e}_\omega$, which is orthogonal to $\mathbf{e}_v$. With the vector product $\mathbf{e}_\omega \times \mathbf{e}_v = \mathbf{e}_\perp$ the third unit vector is given, which is coplanar with $\mathbf{e}_v$ in the contact area plane. Its index $\perp$ is chosen to indicate that it is orthogonal to both $\mathbf{e}_\omega$ and $\mathbf{e}_v$.
These three unit vectors give an orthonormal system and read:

$$\mathbf{v}_\mathrm{t} = v_t \mathbf{e}_v, \qquad \boldsymbol{\omega}_n = \omega_\mathrm{n} \mathbf{e}_\omega \tag{3.3}$$

Due to the circular geometry of the contact area it is favorable to use polar coordinates which gives two additional unit vectors:

$$\begin{aligned} \mathbf{e}_\varphi &= -\sin\varphi\ \mathbf{e}_v + \cos\varphi\ \mathbf{e}_\perp + 0\ \mathbf{e}_\omega = \begin{pmatrix} -\sin\varphi \\ \cos\varphi \\ 0 \end{pmatrix} \\ \mathbf{e}_r &= \cos\varphi\ \mathbf{e}_v + \sin\varphi\ \mathbf{e}_\perp + 0\ \mathbf{e}_\omega = \begin{pmatrix} \cos\varphi \\ \sin\varphi \\ 0 \end{pmatrix} \end{aligned} \tag{3.4}$$

Where $r = |\mathbf{r}|$ the distance from the center.
The overall velocity $\mathbf{v}$ can be written in the following form:

$$\begin{aligned} \mathbf{v} &= v_t \mathbf{e}_v + \omega_\mathrm{n} \mathbf{e}_\omega \times r \mathbf{e}_r \\ \Longrightarrow \mathbf{v} &= v_t \mathbf{e}_v + \omega_\mathrm{n} r \mathbf{e}_\varphi \end{aligned} \tag{3.5}$$

This form of $\mathbf{v}$ will be used for the formulation of the local friction force.

### 3.2.1 Local friction force

A more general approach for the velocity dependence of the friction force and torque is chosen. The magnitude of relative velocity of each surface element $\mathbf{v}$ now has an exponent $\alpha > 0$. The friction force for every surface element $dA$ is:

$$\begin{aligned} d\mathbf{f}_\alpha &= -\gamma^\alpha P(F_\mathrm{n}, R_\mathrm{c}) \, |\mathbf{v}|^\alpha \frac{\mathbf{v}}{|\mathbf{v}|} \, dA \\ &= -\gamma^\alpha P(F_\mathrm{n}, R_\mathrm{c}) \, |\mathbf{v}_\mathrm{t} + \boldsymbol{\omega}_n \times \mathbf{r}|^{\alpha-1} (\mathbf{v}_\mathrm{t} + \boldsymbol{\omega}_n \times \mathbf{r}) \, dA \end{aligned} \tag{3.6}$$

The dimension of the coefficient $\gamma^\alpha$ is $[\gamma^\alpha] = \mathsf{T}^\alpha \mathsf{L}^{-\alpha}$, where $\mathsf{T}$ has the dimension of time and $\mathsf{L}$ has the dimension of length. Thus, the dimensions on both sides of Eq. (3.7) are equal. For $\alpha = 0$ only the direction of velocity remains and its magnitude is not involved. This is the velocity independent dry Coulomb friction law. With $\alpha = 1$ a linear dependence on $\mathbf{v}$ is given.

With the introduction of a dimensionless velocity ratio $\varepsilon$ and dimensionless position vector $\tilde{\mathbf{r}}$:

$$\varepsilon = \frac{v_t}{\omega_\mathrm{n} R_\mathrm{c}} \geq 0, \qquad \tilde{\mathbf{r}} = \frac{\mathbf{r}}{R_\mathrm{c}} \, . \tag{3.7}$$

one can write $\mathbf{v}$ (Eq. (3.5)) as:

$$\mathbf{v} = \omega_\mathrm{n} R_\mathrm{c} \left( \varepsilon \mathbf{e}_v + \tilde{r} \mathbf{e}_\varphi \right) \, .$$

Together with the uniform pressure distribution Eq. (3.1) and the property $dA = d^2 r = R_\mathrm{c}^2 d^2 \tilde{r} = R_\mathrm{c}^2 \tilde{r} d\tilde{r} d\varphi$, one finally gets for the friction force on each surface element $d\mathbf{f}_\alpha$:

$$d\mathbf{f}_\alpha = -\gamma^\alpha \frac{F_\mathrm{n}}{\pi} (\omega_\mathrm{n} R_\mathrm{c})^\alpha |\varepsilon \mathbf{e}_v + \tilde{r} \mathbf{e}_\varphi|^{\alpha-1} (\varepsilon \mathbf{e}_v + \tilde{r} \mathbf{e}_\varphi) \, \tilde{r} d\tilde{r} d\varphi. \tag{3.8}$$

The net friction force and friction torque are the integrals over $d\mathbf{f}_\alpha$:

$$\mathbf{F}_\alpha = \int_0^1 \int_0^{2\pi} d\mathbf{f}_\alpha \tag{3.9}$$

$$\mathbf{T}_\alpha = R_\mathrm{c} \int_0^1 \int_0^{2\pi} \tilde{\mathbf{r}} \times d\mathbf{f}_\alpha. \tag{3.10}$$

The integration can be done with a dimensionless integrand by putting all constant factors in front of the integral signs.

Similar to the Coulomb graph (FIG. 2.5) one can illustrate the dependence of $d\mathbf{f}_\alpha$ on $|\mathbf{v}|$. In FIG. 3.3 this is shown for the values $\alpha = 0, 0.1, 0.5, 1, 2, 3$, with taking the sign of $\mathbf{v}$ for the friction forces into account (the friction force has the opposite sign of the velocity). This figure gives an impression of how the velocity dependence changes with the exponent. For $\alpha = 0$ the friction force is a step function of the velocity and indetermined for $|\mathbf{v}| = 0$. This is not a problem, as only kinetic friction forces are considered here, i.e. forces for $\mathbf{v} \neq 0$.

The following section concerning the frictional coupling for dry friction is based on the publication by Farkas et al. [12].

### 3.2.2 Coulomb friction: $\alpha = 0$

Now $\alpha = 0$ is inserted into the ansatz of $d\mathbf{f}_\alpha$ (EQ. (3.8)) and one gets:

$$\begin{aligned} d\mathbf{f}_0 &= -\gamma_0 \frac{F_\mathrm{n}}{\pi} (\omega_\mathrm{n} R_\mathrm{c})^0 |\varepsilon \mathbf{e}_v + \tilde{r}\mathbf{e}_\varphi|^{-1} (\varepsilon \mathbf{e}_v + \tilde{r}\mathbf{e}_\varphi) \tilde{r} d\tilde{r} d\varphi \\ &= -\gamma_0 \frac{F_\mathrm{n}}{\pi} \frac{\varepsilon \mathbf{e}_v + \tilde{r}\mathbf{e}_\varphi}{|\varepsilon \mathbf{e}_v + \tilde{r}\mathbf{e}_\varphi|} \tilde{r} d\tilde{r} d\varphi = -\gamma_0 \frac{F_\mathrm{n}}{\pi} \frac{\varepsilon \mathbf{e}_v + \tilde{r}\mathbf{e}_\varphi}{\sqrt{\varepsilon^2 + \tilde{r}^2 - 2\varepsilon\tilde{r}\sin\varphi}} \tilde{r} d\tilde{r} d\varphi \end{aligned}$$

This friction force fulfills the requirements of the dry friction law: proportionality to the load and independence of the relative velocity, i.e. Coulomb's dry friction law. The minus sign takes into account the opposite direction of friction to the relative velocity. The coefficient $\gamma_0$ is dimensionless and in this case it is the dynamic friction coefficient $\mu_d$ of dry friction (which was introduced in the historical review (SEC. 2.1)). Thus, the notation $\mu_d$ for $\gamma_0$

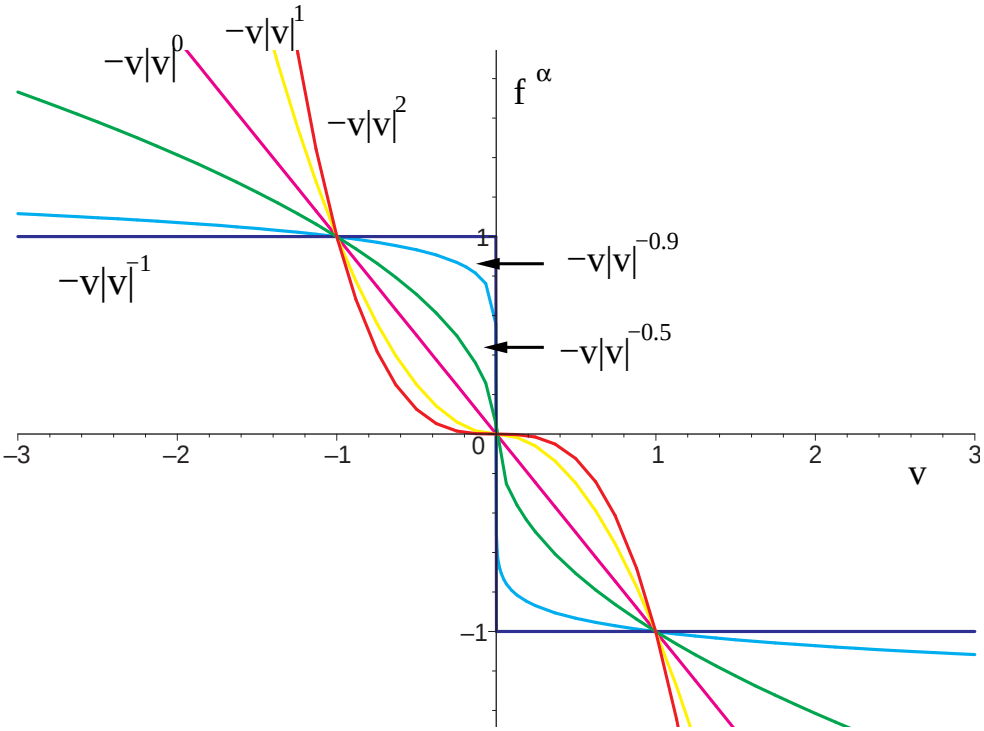


Figure 3.3: In this figure four different powers of $|\mathbf{v}|$ are plotted taking the sign for the friction forces into account. The largest qualitative change in the graphs occurs from $-\mathbf{v}|\mathbf{v}|^{-1}$ to $-\mathbf{v}|\mathbf{v}|^{2}$ .

will be used from here on.

The net sliding friction force $\mathbf{F}_0$ is:

$$\mathbf{F}_0 = -\mu_d \frac{F_\mathrm{n}}{\pi} \int_0^1 \int_0^{2\pi} \frac{\varepsilon \mathbf{e}_v + \tilde{r}\mathbf{e}_\varphi}{\sqrt{\varepsilon^2 + \tilde{r}^2 - 2\varepsilon\tilde{r}\sin\varphi}} \tilde{r} d\tilde{r} d\varphi$$

The integral is of elliptic type and can be evaluated to the form:

$$\mathbf{F}_0 \cdot \mathbf{e}_v = -\mu_d F_\mathrm{n} \cdot \mathcal{F}_{\mathrm{v},0}(\varepsilon), \text{ with} \tag{3.11}$$

$$\mathcal{F}_{\mathrm{v},0}(\varepsilon) = \begin{cases} \frac{4}{3}\frac{(\varepsilon^2+1)E(\varepsilon) + (\varepsilon^2-1)K(\varepsilon)}{\varepsilon\pi}, & \varepsilon \leq 1 \\ \frac{4}{3}\frac{(\varepsilon^2+1)E(\frac{1}{\varepsilon}) - (\varepsilon^2-1)K(\frac{1}{\varepsilon})}{\pi}, & \varepsilon \geq 1. \end{cases}$$

The $\mathbf{e}_\perp$ component of $\mathbf{F}_0$ vanishes, so the friction force has no transverse component. $K(\varepsilon)$ and $E(\varepsilon)$ are the complete elliptic integral functions of the first and the second kind, respectively [35]. One can show, that the two parts of $\mathcal{F}_{\mathrm{v},0}(\varepsilon)$ are continuously and even smoothly connected at $\varepsilon = 1$:

$$\lim_{\varepsilon\to 1}\mathcal{F}_{\mathrm{v},0}(\varepsilon) = \frac{8}{3\pi}\ , \quad \lim_{\varepsilon\to 1}\frac{d}{d\varepsilon}\mathcal{F}_{\mathrm{v},0}(\varepsilon) = \frac{4}{3\pi}. \tag{3.12}$$

One obtains the same values by taking the limit from both the left and the right side. For vanishing $\varepsilon$, and for infinite $\varepsilon$ one gets the following values:

$$\mathcal{F}^0_{t,min}(0) = 0 \quad , \ \lim_{\varepsilon\to\infty}\mathcal{F}^0_{t,max}(\varepsilon) = 1$$

The sliding friction force is zero for $\varepsilon = 0$, while it has an upper bound of 1 for infinite $\varepsilon$.

For the friction torque $\mathbf{T}_0$ the integral is:

$$\mathbf{T}_0 = -\mu_d\frac{F_\mathrm{n}R_\mathrm{c}}{\pi}\int_0^1\int_0^{2\pi}\tilde{\mathbf{r}}\times\frac{\varepsilon\mathbf{e}_v + \tilde{r}\mathbf{e}_\varphi}{\sqrt{\varepsilon^2+\tilde{r}^2-2\varepsilon\tilde{r}\sin\varphi}}\tilde{r}d\tilde{r}d\varphi\ .$$

It is evaluated to [1]:

$$\mathbf{T}_0\cdot\mathbf{e}_\omega \ = \ -\mu_d F_\mathrm{n}R_\mathrm{c}\mathcal{T}_{\mathrm{n},0}(\varepsilon),\ \text{where} \tag{3.13}$$

$$\mathcal{T}_{\mathrm{n},0}(\varepsilon) \ = \ \begin{cases} \dfrac{4}{9}\dfrac{(4-2\varepsilon^2)E(\varepsilon)+(\varepsilon^2-1)K(\varepsilon)}{\pi}, & \varepsilon\le 1 \\ \dfrac{4\varepsilon}{9}\dfrac{(4-2\varepsilon^2)E(\frac{1}{\varepsilon})+(2\varepsilon^2-5+\frac{3}{\varepsilon^2})K(\frac{1}{\varepsilon})}{\pi}, & \varepsilon\ge 1. \end{cases}$$

As for $\mathcal{F}_{\mathrm{v},0}(\varepsilon)$ the two parts of $\mathcal{T}_{\mathrm{n},0}(\varepsilon)$ are also continuously and smoothly connected:

$$\lim_{\varepsilon\to 1}\mathcal{T}_{\mathrm{n},0}(\varepsilon) = \frac{8}{9\pi}, \quad \lim_{\varepsilon\to 1}\frac{d}{d\varepsilon}\mathcal{T}_{\mathrm{n},0}(\varepsilon) = \frac{-4}{3\pi} \tag{3.14}$$

For vanishing angular velocity $\omega_\mathrm{n}$, i.e. $\varepsilon\to\infty$, the function $\mathcal{T}_{\mathrm{n},0}(\varepsilon)$ becomes

$$\lim_{\varepsilon\to\infty}\mathcal{T}^0_{n,min}(\varepsilon) = 0, \tag{3.15}$$

[1] In REF. [12] a typing error occurred in $\mathcal{T}_{\mathrm{n},0}(\varepsilon)$ for $\varepsilon \ge 1$, where $\varepsilon$ appeared in the denominator and not in the enumerator.

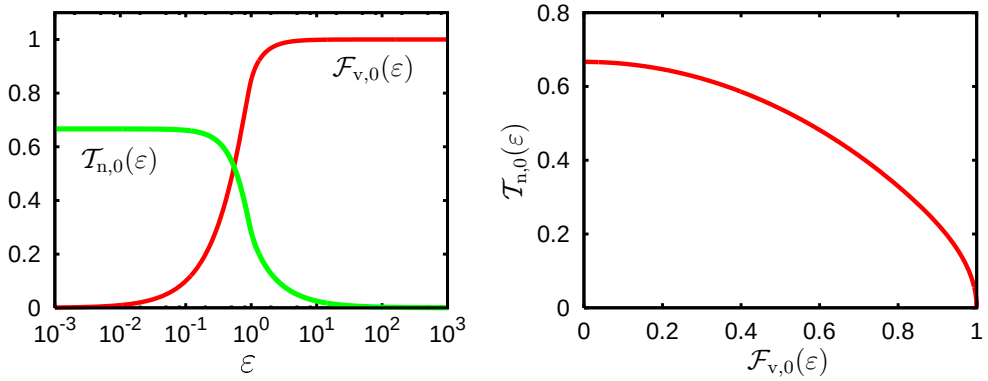


Figure 3.4: The left graph shows the dimensionless friction force $\mathcal{F}_{\mathrm{v},0}(\varepsilon)$ and torque $\mathcal{T}_{\mathrm{n},0}(\varepsilon)$ as functions of the dimensionless velocity parameter $\varepsilon$. The right graph shows the possible $(\mathcal{F}_{\mathrm{v},0}(\varepsilon), \mathcal{T}_{\mathrm{n},0}(\varepsilon))$ pairs. As $\mathcal{F}_{\mathrm{v},0}(\varepsilon)$ and $\mathcal{T}_{\mathrm{n},0}(\varepsilon)$ are strictly monotonous functions, $\mathcal{F}_{\mathrm{v},0}(\varepsilon)$ can be considered as a function of $\mathcal{T}_{\mathrm{n},0}(\varepsilon)$ and vice versa.

while for $\omega_{\mathrm{n}}$ going to infinity, i.e. $\varepsilon \to 0$, the limiting value is

$$\mathcal{T}^{0}_{n,max}(0) = \frac{2}{3} \,. \tag{3.16}$$

The velocity dependence of friction force $\mathbf{F}_0$ and friction torque $\mathbf{T}_0$ is completely covered by the dimensionless velocity ratio $\varepsilon$. This is not the case for $\alpha > 0$, as will be shown.

Alternatively, $\mathcal{F}_{\mathrm{v},0}(\varepsilon)$ and $\mathcal{T}_{\mathrm{n},0}(\varepsilon)$ can be expressed without the distinction of cases at $\varepsilon = 1$ [32, 36]:

$$\mathcal{F}_{\mathrm{v},0}(\varepsilon) = \frac{2(1+\varepsilon)}{3\pi\varepsilon}\left[(1+\varepsilon^2)E\left(\frac{2\sqrt{\varepsilon}}{1+\varepsilon}\right) - (1-\varepsilon)^2 K\left(\frac{2\sqrt{\varepsilon}}{1+\varepsilon}\right)\right] \tag{3.17}$$

$$\mathcal{T}_{\mathrm{n},0}(\varepsilon) = \frac{4(1+\varepsilon)}{9\pi}\left[(2-\varepsilon^2)E\left(\frac{2\sqrt{\varepsilon}}{1+\varepsilon}\right) + (1-\varepsilon)^2 K\left(\frac{2\sqrt{\varepsilon}}{1+\varepsilon}\right)\right] \tag{3.18}$$

One should note that $\mathcal{F}_{\mathrm{v},0}(\varepsilon)$ and $\mathcal{T}_{\mathrm{n},0}(\varepsilon)$ are undefined for $\varepsilon = 1$ as the complete elliptic integral of the first kind $K(1)$ is infinite. But it can be shown, that both functions are smoothly connected there, and with exactly the same limits as given in Eq. (3.12) and Eq. (3.14).

The dimensionless friction force, $\mathcal{F}_{\mathrm{v},0}(\varepsilon)$, and torque, $\mathcal{T}_{\mathrm{n},0}(\varepsilon)$, as function of $\varepsilon$ and also the function $\mathcal{T}_{\mathrm{n},0}(\mathcal{F}_{\mathrm{v},0})$ are displayed in Fig. 3.4. The latter function is invertable, as both, $\mathcal{F}_{\mathrm{v},0}(\varepsilon)$ and $\mathcal{T}_{\mathrm{n},0}(\varepsilon)$ are strictly monotonous

functions. For large values of $\varepsilon$, where the angular velocity is small compared with the sliding velocity, the dimensionless friction torque vanishes, while the dimensionless friction force approaches its maximum value of 1. Inversely, for small $\varepsilon$, where the sliding velocity is very small compared with the angular velocity, the friction force vanishes, while the friction torque approaches the value 2/3. The friction force and torque dynamically reduce each other in a range of roughly $10^{-2}$ to $10^{2}$ for $\varepsilon$. This is an important feature of the frictional coupling in this case, since it works as a negative feedback system which effectively equilibrates the sliding and spinning motion. This will be discussed in more detail in Sec. 3.4, where it is shown that the velocity ratio $\varepsilon$ equilibrates to a certain value independent of the initial conditions.

To disregard the frictional coupling means to use the maximum values of friction force and torque and thus neglecting their $\varepsilon$ dependence. For the friction torque this means using $\mathcal{T}_{\mathrm{n},0}(\varepsilon) = 2/3$ and for the friction force $\mathcal{F}_{\mathrm{v},0}(\varepsilon) = 1$. The previously discussed dynamical reduction and the vanishing of the friction force and torque for the limit cases $\varepsilon = 0$ and $\varepsilon = \infty$, respectively, would not be considered. As a consequence, the dissipation of a system is *overestimated*. That means, if coupling is neglected the dissipation in a system can only be considered as an upper bound.

**Experimental validation**

The analytic solutions for the coupled friction force and torque have been experimentally validated by Zénó Farkas. He performed experiments with a plastic disc having a radius of 8 cm and 2 cm width. It was manually set into sliding and spinning motion on a plastic polyamid fabric surface and video recorded during its decelerating motion. The movie was decomposed to single digital images. The image sequences have been analyzed and values for the friction force and torque were obtained. These results are shown as squares for the friction force and triangles for the friction torque in Fig. 3.5. The solid and dashed curve represent the analytic solutions given by the equations Eq. (3.11) and Eq. (3.13) and are shown for comparison reasons. For further details on the experimental data analysis see reference [12]. Finally, the theoretically obtained nontrivial equations for friction force and torque are validated by the experimental results very well.

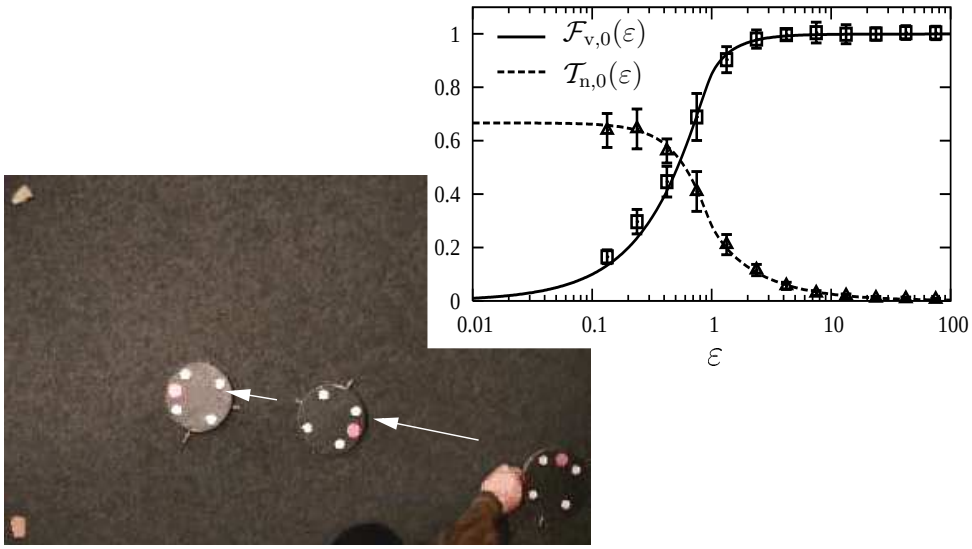


Figure 3.5: The left image shows a sequence of three snapshots (connected by the white arrows) from the experiments performed by Zénó Farkas. A disk was labeled with markers and set into sliding and spinning motion by hand. The motion was recorded with a digital video camera. The graph on the right shows the experimental results together with the curves from the analytic solution for the friction force (solid line) and torque (dashed line). The squares represent data for the friction force and the triangles for the friction torque, while the solid and dashed line represents the theoretical curves for friction force and torque, respectively.

### 3.2.3 Odd exponents $\alpha$

If one assumes integer $\alpha$, one can distinguish between the two cases of odd and even $\alpha$. With the property of the Euclidean vector norm for even exponents $\alpha > 0$,

$$|\mathbf{v}|^{\alpha} = \mathbf{v}^{\alpha}$$

one can distinguish two cases for the friction force of each surface element:

$$\begin{aligned} d\mathbf{f}_{\alpha} &= -\gamma^{\alpha} P(F_{\mathrm{n}}, R_{\mathrm{c}})\ |\mathbf{v}|^{\alpha-1}\mathbf{v}\ dA \\ &= -P(F_{\mathrm{n}}, R_{\mathrm{c}})\ dA \begin{cases} \gamma_{\alpha}\dfrac{\mathbf{v}^{\alpha+1}}{|\mathbf{v}|}, & \alpha \geq 0,\ \text{even} \\ \gamma_{\alpha}\mathbf{v}^{\alpha}, & \alpha > 0,\ \text{odd} \end{cases} \end{aligned} \tag{3.19}$$

The vector norm $|\mathbf{v}|$ remains in the expression (in the denominator) for even $\alpha$, while for odd $\alpha$ the vector norm is not involved. This makes the integration of $d\mathbf{f}_\alpha$ simpler. The explicit derivation of friction force and torque for odd $\alpha$ is presented in App. A. Here only the friction force and torque for the special cases with $\alpha = 1$ and $\alpha = 3$ are calculated, as they are used for further discussion and provide interesting properties.

### 3.2.4 Friction linear in v: $\alpha = 1$

For $\alpha = 1$ one has:

$$d\mathbf{f}_1 \;=\; -\gamma_1 \frac{F_\mathrm{n}}{\pi}(\omega_\mathrm{n} R_\mathrm{c})(\varepsilon \mathbf{e}_v + \tilde{r}\mathbf{e}_\varphi)\; \tilde{r} d\tilde{r} d\varphi \;.$$

The net (sliding) friction force $\mathbf{F}_1$ is then given as:

$$\mathbf{F}_1 = -\gamma_1 \frac{F_\mathrm{n}}{\pi}(\omega_\mathrm{n} R_\mathrm{c}) \int_0^1 \int_0^{2\pi} (\varepsilon \mathbf{e}_v + \tilde{r}\mathbf{e}_\varphi) \tilde{r} d\tilde{r} d\varphi \;.$$

Expanding the sum and using $\mathbf{e}_\varphi = (-\sin\varphi \mathbf{e}_v + \cos\varphi \mathbf{e}_\perp)$ leads to the two integrals:

$$\begin{aligned} \mathbf{F}_1 \;=\; & -\gamma_1 \frac{F_\mathrm{n}}{\pi}(\omega_\mathrm{n} R_\mathrm{c}) \int_0^1 \int_0^{2\pi} \varepsilon \mathbf{e}_v \tilde{r} d\tilde{r} d\varphi \\ & -\gamma_1 \frac{F_\mathrm{n}}{\pi}(\omega_\mathrm{n} R_\mathrm{c}) \int_0^1 \int_0^{2\pi} \tilde{r}(-\sin\varphi \mathbf{e}_v + \cos\varphi \mathbf{e}_\perp) \tilde{r} d\tilde{r} d\varphi \;. \end{aligned}$$

After integration over $d\varphi$ only the first term remains which only has a component in direction of $\mathbf{e}_v$. Doing the last integration gives:

$$\mathbf{F}_1 \cdot \mathbf{e}_v \;=\; -2\gamma_1 F_\mathrm{n}(\omega_\mathrm{n} R_\mathrm{c})\varepsilon \int_0^1 \tilde{r} d\tilde{r} \;= -\gamma_1 F_\mathrm{n}(\omega_\mathrm{n} R_\mathrm{c})\varepsilon \;.$$

The dimensionless friction force is given as $\mathcal{F}_{\mathrm{v},1}(\varepsilon) = \varepsilon$.
Using $\varepsilon = v_t/\omega_\mathrm{n} R_\mathrm{c}$ gives for the net friction force:

$$\mathbf{F}_1 \cdot \mathbf{e}_v \;=\; -\gamma_1 F_\mathrm{n} v_t \;.$$

The sliding friction force $\mathbf{F}_1$ has no component in $\mathbf{e}_\perp$ direction and does *not* depend on the angular velocity $\omega_\mathrm{n}$, thus is *decoupled*.

The net friction torque $\mathbf{T}_1$ for $\alpha = 1$ is given as:

$$\begin{aligned}\mathbf{T}_1 &= R_\mathrm{c} \int_0^1 \int_0^{2\pi} \tilde{\mathbf{r}} \times d\mathbf{f}_1 \\ &= -\gamma_1 \frac{F_\mathrm{n} R_\mathrm{c}}{\pi} (\omega_\mathrm{n} R_\mathrm{c}) \int_0^1 \int_0^{2\pi} \tilde{r}\mathbf{e}_r \times (\varepsilon \mathbf{e}_v + \tilde{r}\mathbf{e}_\varphi) \tilde{r} d\tilde{r} d\varphi \ .\end{aligned}$$

The expansion of the integrand gives two cross products of unit vectors:

$$\begin{aligned}\mathbf{e}_r \times \mathbf{e}_v &= (-\sin\varphi)\mathbf{e}_\omega \ , \\ \mathbf{e}_r \times \mathbf{e}_\varphi &= \mathbf{e}_\omega \ .\end{aligned}$$

This shows, that the net friction torque will only have a component in direction of $\mathbf{e}_\omega$ and results in:

$$\begin{aligned}\mathbf{T}_1 \cdot \mathbf{e}_\omega &= -\gamma_1 \frac{F_\mathrm{n} R_\mathrm{c}}{\pi} (\omega_\mathrm{n} R_\mathrm{c}) \int_0^1 \int_0^{2\pi} \tilde{r}\varepsilon(-\sin\varphi) \tilde{r} d\tilde{r} d\varphi \\ &\quad -\gamma_1 \frac{F_\mathrm{n} R_\mathrm{c}}{\pi} (\omega_\mathrm{n} R_\mathrm{c}) \int_0^1 \int_0^{2\pi} \tilde{r}^2 \tilde{r} d\tilde{r} d\varphi\end{aligned}$$

The first integral vanishes after integration of $d\varphi$, while the second integral gives:

$$\mathbf{T}_1 \cdot \mathbf{e}_\omega = -2\gamma_1 F_\mathrm{n} R_\mathrm{c} (\omega_\mathrm{n} R_\mathrm{c}) \int_0^1 \tilde{r}^3 d\tilde{r} \ = -\gamma_1 \frac{F_\mathrm{n} R_\mathrm{c}}{2} (\omega_\mathrm{n} R_\mathrm{c})$$

The dimensionless friction torque, $\mathcal{T}_{\mathrm{n},1}(\varepsilon) = 1/2$, is just a constant value for $\alpha = 1$. The friction torque has only a component in direction of $\mathbf{e}_\omega$ and does *not* depend on the sliding velocity $v_t$. Thus, the friction torque is *decoupled* as well.

The friction force and torque for $\alpha = 1$ are in summary:

$$\mathbf{F}_1 \cdot \mathbf{e}_v = -\gamma_1 F_\mathrm{n} v_t, \qquad \mathbf{T}_1 \cdot \mathbf{e}_\omega = -\gamma_1 \frac{F_\mathrm{n} R_\mathrm{c}}{2} (\omega_\mathrm{n} R_\mathrm{c})$$

The local coupling of the velocities in $d\mathbf{f}_1$ has vanished in the net friction force and torque. The sliding friction force has no component in $\mathbf{e}_\perp$ direction, thus the initial sliding direction is not changed.

### 3.2.5 Friction cubic in v: $\alpha = 3$

The friction force and torque for $\alpha = 3$ is derived now, with $d\mathbf{f}_3$ as follows:

$$\begin{aligned} d\mathbf{f}_3 &= -\gamma_3 \frac{F_\mathrm{n}}{\pi}(\omega_\mathrm{n} R_\mathrm{c})^3 |\varepsilon \mathbf{e}_v + \tilde{r}\mathbf{e}_\varphi|^2 (\varepsilon \mathbf{e}_v + \tilde{r}\mathbf{e}_\varphi)\ \tilde{r} d\tilde{r} d\varphi. \\ &= -\gamma_3 \frac{F_\mathrm{n}}{\pi}(\omega_\mathrm{n} R_\mathrm{c})^3 \underbrace{(\varepsilon \mathbf{e}_v + \tilde{r}\mathbf{e}_\varphi)^3}_{\tilde{\mathbf{v}}^3 = \tilde{\mathbf{v}}^2 \cdot \tilde{\mathbf{v}}} \tilde{r} d\tilde{r} d\varphi \end{aligned}$$

Again the property of the Euclidean vector norm, $|\mathbf{v}|^2 = \mathbf{v}^2$, has been used and a cubic dimensionless velocity was defined as $\tilde{\mathbf{v}}^3 = \tilde{\mathbf{v}}^2 \cdot \tilde{\mathbf{v}}$. The scalar product $\tilde{\mathbf{v}}^2$ gives:

$$\begin{aligned} \tilde{\mathbf{v}}^2 &= (\varepsilon \mathbf{e}_v + \tilde{r}\mathbf{e}_\varphi)^2 \\ &= \varepsilon^2 \mathbf{e}_v \cdot \mathbf{e}_v + 2\varepsilon\tilde{r}\mathbf{e}_v \cdot \mathbf{e}_\varphi + \tilde{r}^2 \mathbf{e}_\varphi \cdot \mathbf{e}_\varphi \\ &= \varepsilon^2 + \tilde{r}^2 - 2\varepsilon\tilde{r}\sin\varphi\ . \end{aligned} \tag{3.20}$$

This gives then for $\tilde{\mathbf{v}}^3$ explicitely:

$$\tilde{\mathbf{v}}^3 = \tilde{\mathbf{v}}^2(\varepsilon \mathbf{e}_v + \tilde{r}\mathbf{e}_\varphi) = (\varepsilon^2 + \tilde{r}^2 - 2\varepsilon\tilde{r}\sin\varphi) \cdot \begin{pmatrix} \varepsilon - \tilde{r}\sin\varphi \\ \tilde{r}\cos\varphi \\ 0 \end{pmatrix}$$

The net friction force $\mathbf{F}_3$ is then:

$$\begin{aligned} \mathbf{F}_3 &= -\gamma_3 \frac{F_\mathrm{n}}{\pi}(\omega_\mathrm{n} R_\mathrm{c})^3 \int_0^1 \int_0^{2\pi} \tilde{\mathbf{v}}^3 \tilde{r} d\tilde{r} d\varphi \\ &= -\gamma_3 \frac{F_\mathrm{n}}{\pi}(\omega_\mathrm{n} R_\mathrm{c})^3 \\ &\quad \int_0^1 \int_0^{2\pi} \begin{pmatrix} \varepsilon^3 - 3\varepsilon^2\tilde{r}\sin\varphi + 2\varepsilon\tilde{r}^2\sin^2\varphi - \tilde{r}^3\sin\varphi + \varepsilon\tilde{r}^2 \\ \varepsilon^2\tilde{r}\cos\varphi + \tilde{r}^3\cos\varphi - 2\varepsilon\tilde{r}^2\sin\varphi\cos\varphi \\ 0 \end{pmatrix} \tilde{r} d\tilde{r} d\varphi \end{aligned}$$

The second component of the vector in the integrand vanishes completely after integration of $d\varphi$ for the given limits. Only the first component of the vector remains and its integration gives:

$$\begin{aligned} \mathbf{F}_3 \cdot \mathbf{e}_v &= -\gamma_3 \frac{F_\mathrm{n}}{\pi}(\omega_\mathrm{n} R_\mathrm{c})^3 \int_0^1 (2\pi\varepsilon^3\tilde{r} + 2\pi\varepsilon\tilde{r}^3 + 2\pi\varepsilon\tilde{r}^3) d\tilde{r} \\ &= -\gamma_3 F_\mathrm{n}(\omega_\mathrm{n} R_\mathrm{c})^3 \underbrace{(\varepsilon^3 + \varepsilon)}_{\mathcal{F}_{\mathrm{v},3}(\varepsilon)} \end{aligned} \tag{3.21}$$

Inserting in the above defined dimensionless friction force $\mathcal{F}_{\mathrm{v},3}(\varepsilon)$ the ratio $v_t/\omega_\mathrm{n}R_\mathrm{c}$ for $\varepsilon$ does not cancel the dependence on $\omega_\mathrm{n}$ completely, as it was the case for $\alpha = 1$. Further, the velocity dependence of the net friction force $\mathbf{F}_3$ can not be expressed as a function of $\varepsilon$ alone, which was possible for $\mathbf{F}_0$. That means, that for the same value of $\varepsilon$ different friction force values are possible. In fact, this is true as soon as $\alpha > 0$.

The net friction torque $\mathbf{T}_3$ reads:

$$\mathbf{T}_3 = -\gamma_3 \frac{F_\mathrm{n} R_\mathrm{c}}{\pi} (\omega_\mathrm{n} R_\mathrm{c})^3 \int_0^1 \int_0^{2\pi} \tilde{\mathbf{r}} \times \tilde{\mathbf{v}}^3 \tilde{r} d\tilde{r} d\varphi \ .$$

The definitions of $\tilde{\mathbf{v}}^3$ and $\tilde{\mathbf{r}}$ show, that they are coplanar with the contact area, thus a vector product of both results is a vector having a component in $\mathbf{e}_\omega$ direction only, giving:

$$\begin{aligned}
\mathbf{T}_3 \cdot \mathbf{e}_\omega &= -\gamma_3 \frac{F_\mathrm{n} R_\mathrm{c}}{\pi} (\omega_\mathrm{n} R_\mathrm{c})^3 \int_0^1 \int_0^{2\pi} \left( \tilde{r} \cos\varphi (\tilde{\mathbf{v}}^3)_{\mathbf{e}_\perp} - \tilde{r} \sin\varphi (\tilde{\mathbf{v}}^3)_{\mathbf{e}_v} \right) \tilde{r} d\tilde{r} d\varphi \\
&= -\gamma_3 \frac{F_\mathrm{n} R_\mathrm{c}}{\pi} (\omega_\mathrm{n} R_\mathrm{c})^3 \int_0^1 \int_0^{2\pi} \big( \varepsilon^2 \tilde{r}^2 \cos^2\varphi + \tilde{r} - 2\varepsilon \tilde{r}^3 \sin\varphi \cos^2\varphi \\
&\quad -\varepsilon^3 \tilde{r} \sin\varphi + 3\varepsilon^2 \tilde{r}^2 \sin^2\varphi - 2\varepsilon \tilde{r}^3 \sin^3\varphi - \varepsilon \tilde{r}^3 \sin\varphi \big) \tilde{r} d\tilde{r} d\varphi \ .
\end{aligned}$$

Four of the seven terms of the integrand vanish after integrating over $d\varphi$. Doing as last step the integration over $d\tilde{r}$ gives:

$$\begin{aligned}
\mathbf{T}_3 \cdot \mathbf{e}_\omega &= -\gamma_3 \frac{F_\mathrm{n} R_\mathrm{c}}{\pi} (\omega_\mathrm{n} R_\mathrm{c})^3 \int_0^1 \left( 2\pi \tilde{r}^5 + 4\pi \varepsilon^2 \tilde{r}^3 \right) d\tilde{r} \qquad (3.22) \\
&= -\gamma_3 F_\mathrm{n} R_\mathrm{c} (\omega_\mathrm{n} R_\mathrm{c})^3 \underbrace{\left( \varepsilon^2 + \frac{1}{3} \right)}_{\mathcal{T}_{\mathrm{n},1}(\varepsilon)}
\end{aligned}$$

For the friction torque the velocity dependence is the same as for the friction force: it can not be expressed with the parameter $\varepsilon$ solely. If one compares the dimensionless friction force and torque, one finds, that the parameter $\varepsilon$ appears with odd powers in the friction force, while it has even powers in the friction torque. This is also the case if one compares the dimensionless friction force and torque for odd $\alpha > 3$, which can be obtained from the analytic solutions derived in App. A.

In summary, the friction force and torque for $\alpha = 1, 3$ are listed with their explicit dependence on $v_t$ and $\omega_\mathrm{n}$:

$$\begin{aligned} \mathbf{F}_1 &= -\gamma_1 F_\mathrm{n} v_t \mathbf{e}_v & \mathbf{T}_1 &= -\frac{\gamma_1}{2} F_n \omega_\mathrm{n} R_\mathrm{c}^2 \mathbf{e}_\omega \\ \mathbf{F}_3 &= -\gamma_3 F_\mathrm{n} (v_t^3 + v_t \omega_\mathrm{n}^2 R_\mathrm{c}^2) \mathbf{e}_v & \mathbf{T}_3 &= -\gamma_3 F_\mathrm{n} R_\mathrm{c} \left( \frac{1}{3} \omega_\mathrm{n}^3 R_\mathrm{c}^3 + \omega_\mathrm{n} R_\mathrm{c} v_t^2 \right) \mathbf{e}_\omega \end{aligned}$$

For the dry friction with $\alpha = 0$ it was found that the friction force and torque dynamically reduce each other and that a neglection of the coupling would lead to an overestimation of friction. A look at the expressions of friction force and torque with $\alpha = 3$ shows that a neglection of coupling would mean to leave out all terms containing the product of $v_t$ and $\omega_\mathrm{n} R_\mathrm{c}$. But these terms contribute in an amplifying way to the magnitude of friction force and torque, respectively. Disregarding the coupling leads, in this case, to an *underestimation* of friction. The same result can be obtained for general odd $\alpha \geq 3$ analysing the expressions in App. A and it can be expected that the neglection of coupling results in an underestimation of friction for all $\alpha > 1$. In context with the final motion modes the over- and underestimation of friction will be picked up again.

## 3.3 Friction force and torque for small and large $\varepsilon$

In this section the cases are considered, where either translation or rotation dominates the motion. If translation is dominating the motion, then the sliding velocity $v_t$ is much larger than $\omega_\mathrm{n} R_\mathrm{c}$, hence $\varepsilon \gg 1$. And if rotation is dominant, then $\omega_\mathrm{n} R_\mathrm{c}$ is much larger than $v_t$ and $\varepsilon \ll 1$. In both cases the friction force and torque can be approximated to simpler expressions. For illustration the friction force and torque for $\alpha = 3$ are taken as example. After that the approximations of friction force and torque will be derived for general $\alpha$.

The friction force and torque for $\alpha = 3$ are:

$$\begin{aligned} \mathbf{F}_3 \cdot \mathbf{e}_v &= -\gamma_3 F_\mathrm{n} (\omega_\mathrm{n} R_\mathrm{c})^3 (\varepsilon^3 + \varepsilon) \\ \mathbf{T}_3 \cdot \mathbf{e}_\omega &= -\gamma_3 F_\mathrm{n} R_\mathrm{c} (\omega_\mathrm{n} R_\mathrm{c})^3 (\varepsilon^2 + \frac{1}{3}) \end{aligned}$$

For $\varepsilon \ll 1$ one can neglect all terms of order $\mathcal{O}(\varepsilon^2)$ and higher, which gives then:

$$\begin{aligned}\mathbf{F}_3 \cdot \mathbf{e}_v &\approx -\gamma_3 F_\mathrm{n} (\omega_\mathrm{n} R_\mathrm{c})^3 (\varepsilon) = -\gamma_3 F_\mathrm{n} (\omega_\mathrm{n} R_\mathrm{c})^2 v_t \\ \mathbf{T}_3 \cdot \mathbf{e}_\omega &\approx -\gamma_3 F_\mathrm{n} R_\mathrm{c} (\omega_\mathrm{n} R_\mathrm{c})^3 \frac{1}{3} = -\gamma_3 \frac{F_\mathrm{n} R_\mathrm{c}}{3} (\omega_\mathrm{n} R_\mathrm{c})^3\end{aligned}$$

The sliding friction force depends linearly on $v_t$, while the angular velocity enters quadratically into that force. The friction torque is cubic in $\omega_\mathrm{n} R_\mathrm{c}$ and is decoupled from the sliding velocity.

For $\varepsilon \gg 1$ one can keep only the term with the highest order of $\varepsilon$. Keeping only the leading order in $\varepsilon$ one obtains:

$$\begin{aligned}\mathbf{F}_3 \cdot \mathbf{e}_v &\approx -\gamma_3 F_\mathrm{n} (\omega_\mathrm{n} R_\mathrm{c})^3 (\varepsilon^3) = -\gamma_3 F_\mathrm{n} v_t^3 \\ \mathbf{T}_3 \cdot \mathbf{e}_\omega &\approx -\gamma_3 F_\mathrm{n} R_\mathrm{c} (\omega_\mathrm{n} R_\mathrm{c})^3 \varepsilon^2 = -\gamma_3 \frac{F_\mathrm{n} R_\mathrm{c}}{3} (\omega_\mathrm{n} R_\mathrm{c}) v_t^2\end{aligned}$$

While the sliding friction force depends cubically on $v_t$, it enters the friction torque with one order less: $v_t^2$. In this case the slower angular velocity $\omega_\mathrm{n}$ appears linearly and only in the friction torque. In case of $\varepsilon \gg 1$ the friction force is decoupled from the spinning motion.

These approximations for the special case of $\alpha = 3$ will now be extended to the case of general $\alpha \geq 0$.

### 3.3.1 Fast spinning, slow sliding: $\varepsilon \ll 1$

The friction force $d\mathbf{f}_\alpha$ in Eq. (3.8) was:

$$d\mathbf{f}_\alpha = -\gamma^\alpha \frac{F_\mathrm{n}}{\pi} (\omega_\mathrm{n} R_\mathrm{c})^\alpha |\varepsilon \mathbf{e}_v + \tilde{r} \mathbf{e}_\varphi|^{\alpha-1} (\varepsilon \mathbf{e}_v + \tilde{r} \mathbf{e}_\varphi) \, \tilde{r} d\tilde{r} d\varphi \qquad (3.23)$$

The Euclidean vector norm with power $(\alpha - 1)$ is now approximated for small $\varepsilon$ by a Taylor expansion [37]:

$$\begin{aligned}|\varepsilon \mathbf{e}_v + \tilde{r} \mathbf{e}_\varphi|^{\alpha-1} &= (\varepsilon^2 + \tilde{r}^2 - 2\varepsilon \tilde{r} \sin\varphi)^{\frac{\alpha-1}{2}} \\ &\approx \tilde{r}^{(\alpha-1)} - (\alpha - 1) \tilde{r}^{(\alpha-2)} \sin\varphi \varepsilon + \mathcal{O}(\varepsilon^2)\end{aligned}$$

This approximation is substituted in Eq. (3.23). The net sliding friction force is obtained after integration over the contact area and neglection of terms of order $\mathcal{O}(\varepsilon^2)$ and higher:

$$\mathbf{F}_\alpha \cdot \mathbf{e}_v \approx -\gamma^\alpha \frac{F_\mathrm{n}}{\pi} (\omega_\mathrm{n} R_\mathrm{c})^\alpha \pi \varepsilon = -\gamma^\alpha F_\mathrm{n} (\omega_\mathrm{n} R_\mathrm{c})^{\alpha-1} v_t$$

Again, the sliding friction force has only a component in direction of $\mathbf{e}_v$.

The friction torque $\mathbf{T}_\alpha$ is for $\varepsilon \ll 1$:

$$\mathbf{T}_\alpha \cdot \mathbf{e}_\omega \approx -\gamma^\alpha \frac{F_\mathrm{n} R_\mathrm{c}}{\pi} (\omega_\mathrm{n} R_\mathrm{c})^\alpha \frac{2\pi}{\alpha+3} = -\gamma^\alpha F_\mathrm{n} R_\mathrm{c} \frac{2}{\alpha+3} (\omega_\mathrm{n} R_\mathrm{c})^\alpha$$

In the limit of $\varepsilon \ll 1$ the sliding friction force depends linearly on the sliding velocity $v_t$ and the friction torque depends *only* on the angular velocity, thus is decoupled from $v_t$.

### 3.3.2 Fast sliding, slow spinning: $\varepsilon \gg 1$

For very large values of $\varepsilon$ the vector norm is rearranged to the following form:

$$\begin{aligned} |\varepsilon \mathbf{e}_v + \tilde{r}\mathbf{e}_\varphi|^{\alpha-1} &= \left(\varepsilon^2 + \tilde{r}^2 - 2\varepsilon\tilde{r}\sin\varphi\right)^{\frac{\alpha-1}{2}} \\ &= \varepsilon^{\alpha-1}\left(1 + \frac{\tilde{r}^2}{\varepsilon^2} - 2\frac{\tilde{r}}{\varepsilon}\sin\varphi\right)^{\frac{\alpha-1}{2}} \end{aligned}$$

Now the term in paranthesis can be approximated by a Taylor expansion for small $\tilde{r}/\varepsilon$ as $\varepsilon \gg 1$ and $0 \le \tilde{r} \le 1$ :

$$\varepsilon^{\alpha-1}\left(1 + \frac{\tilde{r}^2}{\varepsilon^2} - 2\frac{\tilde{r}}{\varepsilon}\sin\varphi\right)^{\frac{\alpha-1}{2}} \approx \varepsilon^{\alpha-1}\left(1 - (\alpha-1)\sin\varphi\frac{\tilde{r}}{\varepsilon} + \mathcal{O}\left(\frac{\tilde{r}^2}{\varepsilon^2}\right)\right) \tag{3.24}$$

This approximation is multiplied with the first component of the sliding friction,

$$(\varepsilon - \tilde{r}\sin\varphi) = \varepsilon\left(1 - \frac{\tilde{r}}{\varepsilon}\sin\varphi\right) ,$$

which results, after omitting terms of order $\mathcal{O}\left(\frac{\tilde{r}^2}{\varepsilon^2}\right)$ and higher, in:

$$\begin{aligned} \mathbf{F}_\alpha \cdot \mathbf{e}_v &\approx -\gamma^\alpha \frac{F_\mathrm{n}}{\pi} (\omega_\mathrm{n} R_\mathrm{c})^\alpha \int_0^1 \int_0^{2\pi} \varepsilon^\alpha \left(1 - \sin\varphi\frac{\tilde{r}}{\varepsilon} - (\alpha-1)\sin\varphi\frac{\tilde{r}}{\varepsilon}\right) \tilde{r}\, d\tilde{r}\, d\varphi \\ &= -\gamma^\alpha F_\mathrm{n} (\omega_\mathrm{n} R_\mathrm{c})^\alpha \varepsilon^\alpha \\ &= -\gamma^\alpha F_\mathrm{n} v_t^\alpha \end{aligned}$$

The friction force $\mathbf{F}_\alpha \cdot \mathbf{e}_\perp$ would vanish by integration again and is therefore not shown here.

The friction torque component $\mathbf{T}_\alpha \cdot \mathbf{e}_\omega$ is rearranged as well:

$$(\tilde{r}^2 - \varepsilon\tilde{r}\sin\varphi) = \varepsilon^2\left(\frac{\tilde{r}^2}{\varepsilon^2} - \frac{\tilde{r}}{\varepsilon}\sin\varphi\right) .$$

After multiplying this with the approximation in Eq. (3.24) and omitting the terms of order $\mathcal{O}\left(\frac{\tilde{r}^3}{\varepsilon^3}\right)$ and higher one gets:

$$\begin{aligned}
\mathbf{T}_\alpha \cdot \mathbf{e}_\omega &\approx -\gamma^\alpha \frac{F_\mathrm{n} R_\mathrm{c}}{\pi}(\omega_\mathrm{n} R_\mathrm{c})^\alpha \cdot \\
&\quad \int_0^1 \int_0^{2\pi} \varepsilon^{\alpha+1}\left(-\sin\varphi\frac{\tilde{r}}{\varepsilon} + \frac{\tilde{r}^2}{\varepsilon^2} + (\alpha-1)\sin^2\varphi\frac{\tilde{r}^2}{\varepsilon^2}\right)\tilde{r}d\tilde{r}d\varphi \\
&= -\gamma^\alpha F_\mathrm{n} R_\mathrm{c}\frac{1+\alpha}{4}(\omega_\mathrm{n} R_\mathrm{c})^\alpha \varepsilon^{\alpha-1} \\
&= -\gamma^\alpha F_\mathrm{n} R_\mathrm{c}\frac{(1+\alpha)}{4}(\omega_\mathrm{n} R_\mathrm{c}) v_t^{\alpha-1}
\end{aligned}$$

Now, in the limit of $\varepsilon \gg 1$ the spinning is relatively slow and the sliding friction force depends only on the sliding velocity, i.e. is decoupled from $\omega_\mathrm{n}$. The friction torque depends linearly on $\omega_\mathrm{n}$.

The derived approximations are summarized in the table below.

| | $\mathbf{F}_\alpha \cdot \mathbf{e}_v$ | $\mathbf{T}_\alpha \cdot \mathbf{e}_\omega$ |
|---|---|---|
| $\varepsilon \ll 1$ | $-\gamma^\alpha F_\mathrm{n}(\omega_\mathrm{n} R_\mathrm{c})^{\alpha-1} v_t$ | $-\gamma^\alpha F_\mathrm{n} R_\mathrm{c}\frac{2}{\alpha+3}(\omega_\mathrm{n} R_\mathrm{c})^\alpha$ |
| $\varepsilon \gg 1$ | $-\gamma^\alpha F_\mathrm{n} v_t^\alpha$ | $-\gamma^\alpha F_\mathrm{n} R_\mathrm{c}\frac{(1+\alpha)}{4}(\omega_\mathrm{n} R_\mathrm{c}) v_t^{\alpha-1}$ |

Table 3.1: The friction force and torque in the limit of $\varepsilon \ll 1$ and $\varepsilon \gg 1$.

The next section shall clarify how the coupling of the friction force and torque affects the dynamics of the disk.

## 3.4 Final motion modes

A disk on a plane surface, which was set into sliding and spinning motion will be slowed down due to the friction force and torque. Wether one of the motions stops before the other, or both motions stop together, that is the central question of this section. To answer this, the time evolution of the velocity ratio $\varepsilon$ is considered. With the initial sliding and spinning velocity an initial velocity ratio $\varepsilon_i = \varepsilon(t = 0)$ is defined, for a given constant $R_\mathrm{c}$. If $\varepsilon$ decreases towards zero, then the sliding motion is more decelerated than the spinning motion and vice versa if $\varepsilon$ evolves towards larger values or even infinity.

An autonomous differential equation for $\varepsilon$ provides the informations about its tendencies, i.e. increasing or decreasing $\varepsilon$, during its time evolution. From this the final motion mode can be derived, as will be shown. For the autonomous differential equation the time evolution of $v_t$ and $\omega_\mathrm{n}$ is needed.

### 3.4.1 Dynamic equations

The dynamic equations of motion for the sliding and spinning disk of mass $M$, are as follows:

$$\begin{aligned} M\frac{dv_t}{dt} &= \mathbf{F}_\alpha \cdot \mathbf{e}_v &&= -\gamma^\alpha M g (\omega_\mathrm{n} R_\mathrm{c})^\alpha \mathcal{F}_{\mathrm{v},\alpha}(\varepsilon) \\ I\frac{d\omega_\mathrm{n}}{dt} &= \mathbf{T}_\alpha \cdot \mathbf{e}_\omega &&= -\gamma^\alpha M g R_\mathrm{c} (\omega_\mathrm{n} R_\mathrm{c})^\alpha \mathcal{T}_{\mathrm{n},\alpha}(\varepsilon). \end{aligned} \tag{3.25}$$

$I$ is the moment of inertia related to the spinning axis of $\omega$, and it is assumed that only gravity acts as external force on the disk.
By introducing dimensionless velocities and time,

$$v_t^* = \frac{v_t}{\sqrt{R_\mathrm{c}\, g}}\,, \quad \omega_\mathrm{n}^* = \omega_\mathrm{n}\sqrt{\frac{R_\mathrm{c}}{g}}\,, \quad t^* = t\sqrt{\frac{g}{R_\mathrm{c}}}$$

one can write dimensionless dynamic equations:

$$\begin{aligned} \frac{dv_t^*}{dt^*} &= -\gamma^\alpha (\omega_\mathrm{n} R_\mathrm{c})^\alpha \mathcal{F}_{\mathrm{v},\alpha}(\varepsilon) \\ \frac{d\omega_\mathrm{n}^*}{dt^*} &= -\gamma^\alpha (\omega_\mathrm{n} R_\mathrm{c})^\alpha \frac{M R_\mathrm{c}^2}{I} \mathcal{T}_{\mathrm{n},\alpha}(\varepsilon) \end{aligned} \tag{3.26}$$

The coefficient at $\mathcal{T}_{\mathrm{n},\alpha}(\varepsilon)$ describes the ratio between the moment of inertia $I$ and the "moment of inertia" $MR_{\mathrm{c}}^2$, which is achieved if the complete mass would be distributed circularly at the outer edge of the disk with a distance $R_{\mathrm{c}}$ from the center. This is similar to the moment of inertia of a thin ring with mass $M$ and radius $R_{\mathrm{c}}$ [38].

### 3.4.2 Autonomous differential equation for $\varepsilon$

An autonomous differential equation for $\varepsilon$ can be derived using the variable transformation $x = -\ln \omega_{\mathrm{n}}^*$ and $\varepsilon = v_t^*/\omega_{\mathrm{n}}^*$:

$$\begin{aligned}
\frac{d\varepsilon}{dx} &= \frac{d\left(\frac{v_t^*}{\omega_{\mathrm{n}}^*}\right)}{d(-\ln \omega_{\mathrm{n}}^*)} = -\frac{dv_t^*}{d\omega_{\mathrm{n}}^*} + \frac{v_t^*}{\omega_{\mathrm{n}}^*} = -\frac{dv_t^*/dt^*}{d\omega_{\mathrm{n}}^*/dt^*} + \varepsilon \\
&= \varepsilon - \frac{\mathcal{F}_{\mathrm{v},\alpha}(\varepsilon)}{\frac{MR_{\mathrm{c}}^2}{I}\mathcal{T}_{\mathrm{n},\alpha}(\varepsilon)} \\
&= \varepsilon - \frac{I}{MR_{\mathrm{c}}^2}\frac{\mathcal{F}_{\mathrm{v},\alpha}(\varepsilon)}{\mathcal{T}_{\mathrm{n},\alpha}(\varepsilon)} \equiv g_\alpha(\varepsilon)
\end{aligned} \tag{3.27}$$

The right hand side of the equation above is a function of $\varepsilon$ only, so that one has an autonomous differential equation [39]. This autonomous differential equation provides information about the dynamical evolution of $\varepsilon$ into so called fixed points. This is now illustrated with the plots of $g_\alpha(\varepsilon)$ for the three values $\alpha = 0, 1, 3$. With the moment of inertia for the disk, $I = 1/2MR_{\mathrm{c}}^2$, the coefficient at $\mathcal{F}_{\mathrm{v},\alpha}(\varepsilon)/\mathcal{T}_{\mathrm{n},\alpha}(\varepsilon)$ becomes simply $1/2$.

The function $g_\alpha(\varepsilon)$ written for each of $\alpha = 0, 1$ and 3 is:

$$g_0(\varepsilon) = \varepsilon - \frac{3}{4\varepsilon}\frac{(1+\varepsilon^2)E\left(\frac{2\sqrt{\varepsilon}}{1+\varepsilon}\right) - (1-\varepsilon)^2 K\left(\frac{2\sqrt{\varepsilon}}{1+\varepsilon}\right)}{(2-\varepsilon^2)E\left(\frac{2\sqrt{\varepsilon}}{1+\varepsilon}\right) + (1-\varepsilon)^2 K\left(\frac{2\sqrt{\varepsilon}}{1+\varepsilon}\right)}\ , \tag{3.28}$$

$$g_1(\varepsilon) = \varepsilon - \frac{1}{2}\frac{\varepsilon}{\frac{1}{2}} = 0\ , \tag{3.29}$$

$$g_3(\varepsilon) = \varepsilon - \frac{(\varepsilon^3+\varepsilon)}{2(\frac{1}{3}+\varepsilon^2)}\ , \tag{3.30}$$

where the corresponding dimensionless friction force $\mathcal{F}_{\mathrm{v},\alpha}(\varepsilon)$ and torque $\mathcal{T}_{\mathrm{n},\alpha}(\varepsilon)$ were inserted. The curves for each of these three functions are shown in FIG. 3.6. If for a given $\varepsilon$, say $\varepsilon = \varepsilon_i$, the function $g_\alpha(\varepsilon)$ returns a positive

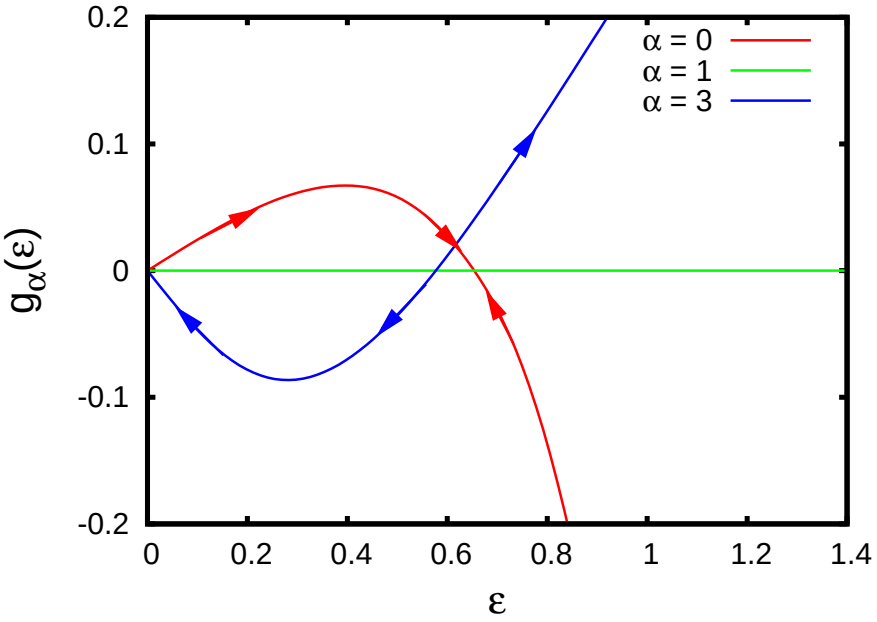


Figure 3.6: The function $g_\alpha(\varepsilon)$ for $\alpha = 0, 1, 3$ is displayed. The common fixed point at $\varepsilon = 0$ is an unstable one for $g_0(\varepsilon)$, while it is semistable for $g_1(\varepsilon)$ and stable for $g_3(\varepsilon)$. For $g_3(\varepsilon)$ an unstable point exists at $\varepsilon = \sqrt{3}/3$, while for $g_0(\varepsilon)$ a stable point at $\varepsilon \approx 0.653$ exists. The black arrows indicate the direction in which $\varepsilon$ evolves if $g_\alpha(\varepsilon)$ is positive or negative.

value, then the velocity ratio $\varepsilon$ is increased for increasing $x$ and if the function returns a negative value then $\varepsilon$ is decreased. In terms of time evolution, one can say, that for $g_\alpha(\varepsilon) > 0$ the velocity ratio $\varepsilon$ evolves towards larger values, while for $g_\alpha(\varepsilon) < 0$ it evolves towards lower values. This behaviour is indicated by the arrows in the figure. The zeros of $g_\alpha(\varepsilon)$ play an important role, as they determine the fixed points of the time evolution of $\varepsilon$. The simplest zero of all $g_\alpha(\varepsilon)$ is $\varepsilon = 0$, which corresponds to the motion of pure spinning, as $v_t = 0$. Another fixed point which is common to $g_\alpha(\varepsilon)$ for all $\alpha$, is $\varepsilon = \infty$ and corresponds to a zero angular velocity, i.e. the motion of the disk is pure sliding. These fixed points will be referred to as "trivial" fixed points, while other fixed points will be called "finite fixed points" and denoted by $\varepsilon_0$. The value of $\varepsilon_0$ is different for every $\alpha$.

Fixed points can be classified as *stable*, *semistable* or *unstable* with the slope of $g_\alpha(\varepsilon)$ in $\varepsilon_0$:

$$\begin{aligned}
\left.\frac{\partial g_\alpha(\varepsilon)}{\partial \varepsilon}\right|_{\varepsilon_0} &> 0, \text{ unstable} \\
\left.\frac{\partial g_\alpha(\varepsilon)}{\partial \varepsilon}\right|_{\varepsilon_0} &= 0, \text{ semistable} \\
\left.\frac{\partial g_\alpha(\varepsilon)}{\partial \varepsilon}\right|_{\varepsilon_0} &< 0, \text{ stable}
\end{aligned}$$

This classification is also possible for the trivial fixed points of $\varepsilon = 0$ and $\varepsilon = \infty$. In the graph of FIG. 3.6 the curve of $g_3(\varepsilon)$ has an unstable fixed point at $\varepsilon_0 = \sqrt{3}/3$ and stable trivial fixed points at $\varepsilon = 0$ and $\varepsilon \to \infty$. That means, that the final motion mode depends on the initial $\varepsilon_i$. If $\varepsilon_i < \varepsilon_0$, then $\varepsilon = 0$ is the attractive fixed point. The sliding velocity is more strongly decelerated than the angular velocity and spinning is becoming the dominant motion mode. On the other hand, if $\varepsilon_i > \varepsilon_0$ then $\varepsilon \to \infty$ is the attractive fixed point, thus the angular velocity is decelerated stronger and sliding is becoming the dominant motion mode. If $\varepsilon_i = \varepsilon_0$ this value of the velocity ratio is kept till the complete motion stops. But this fixed point is unstable and any small perturbation resulting in $\varepsilon_i \neq \varepsilon_0$ leads to an evolution of $\varepsilon$ away from that $\varepsilon_0$. It will depend on the "direction" of the perturbation if $\varepsilon$ evolves either towards zero or infinity.

The situation is different for $g_1(\varepsilon)$, which is zero for every $\varepsilon$ and thus has infinitely many semistable points. That means, that the disk started with the ratio value $\varepsilon_i$ keeps this ratio until it comes to rest, presuming that no perturbation occurs. The effect of a perturbation would be that $\varepsilon$ changes from one semistable fixed point to another, which will be retained. The curve of $g_0(\varepsilon)$ has a *stable* finite fixed point $\varepsilon_0$ at $\varepsilon \approx 0.653$. For any $\varepsilon_i \neq \varepsilon_0$, except for $\varepsilon_i = 0$ or $\varepsilon_i = \infty$, the $\varepsilon$ evolves to that attractive stable fixed point. This means, in case of dry Coulomb friction the sliding and spinning motion will stop at the same time, independent of the initial velocities, i.e. $\varepsilon_i$.

The exponents $\alpha = 0, 1$ and 3 are just examples and have been chosen because their analytic solutions were at hand. The functions of $g_\alpha(\varepsilon)$ for $\alpha > 1$ are similar to $g_3(\varepsilon)$ in the sense that all have single *unstable* finite fixed point, where the final motion mode depends on the initial $\varepsilon$, i.e. if $\varepsilon_i > \varepsilon_0$ or $\varepsilon_i < \varepsilon_0$. Thus the dynamical behaviour of the disk is then similar for all $\alpha > 1$.

In the following paragraph it is shown, that for any $\alpha < 1$ the function $g_\alpha(\varepsilon)$ has *stable finite* fixed points.

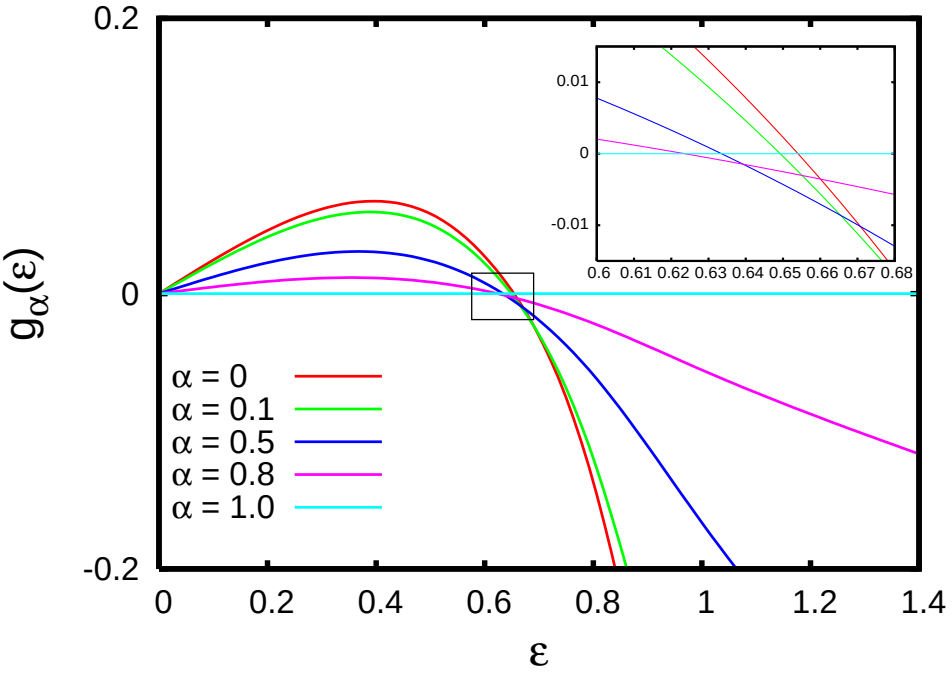


Figure 3.7: The transition from Coulomb friction to linear friction for some selected values $\alpha \in [0, 1]$. For all curves a stable finite fixed point exists.

### 3.4.3 Final motion modes for $\alpha < 1$

In FIG. 3.7 the function $g_\alpha(\varepsilon)$ is shown for some selected values of $\alpha$ from the interval $[0, 1]$. The data for these curves were obtained by numerical integration of EQ. (3.9) and EQ. (3.10) with the corresponding $\alpha$. The numerical integration was done with a small program written in C which uses the trapezoid rule [40]. For $\alpha = 0$ the numerical integration was done for validation reasons: the results obtained from the numerical integration have been compared with values from the analytic equations for EQ. (3.11) and EQ. (3.13) without noticing significant deviations.
It can be seen from FIG. 3.7, that every curve possesses a *stable* finite fixed point. Further, with increasing $\alpha$ the curves approach the horizontal $\varepsilon-$axis, but the negative slope in the finite fixed point at $\varepsilon_0$ is retained.The inset zooms closer to the range of the finite fixed points and shows that they are all distinct, lying in a small range $[0.62, 0.64]$.

As will be shown below, for every $0 \leq \alpha < 1$ a *finite stable* fixed point exists. This property changes when $\alpha \geq 1$. The conclusion is, that for coupled

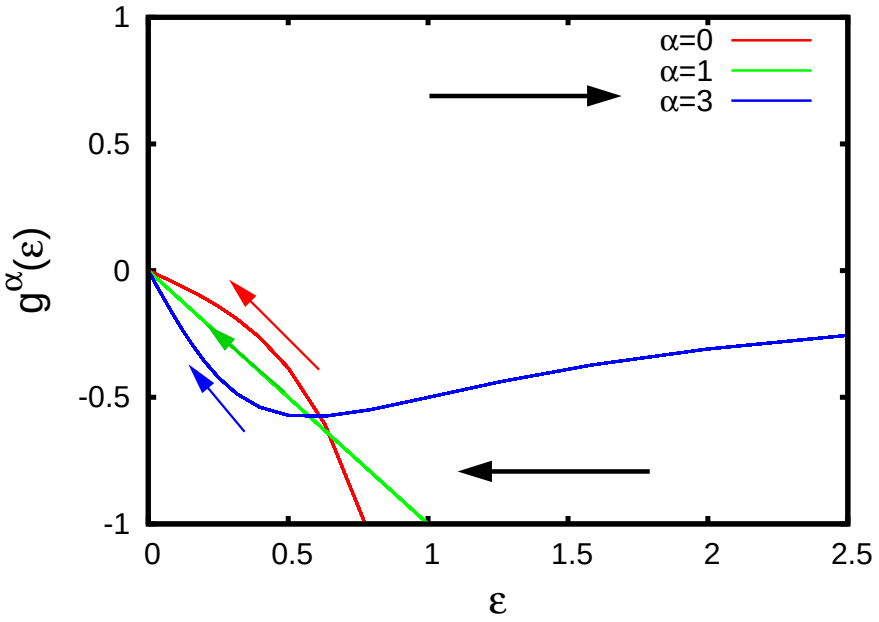


Figure 3.8: The function $g_\alpha(\varepsilon)$ is shown with $C = 1$. In contrast to the case of the disk (see FIG. 3.6), now all curves have the trivial fixed point in $\varepsilon = 0$ as a stable one. The final motion is then dominated by the spinning motion.

friction force and torque with $0 \leq \alpha < 1$ a stable finite fixed point exists and that sliding and spinning always stop together.

In function $g_\alpha(\varepsilon)$ the value of $I/MR_c^2$ is a fixed value depending on the geometry and mass distribution of the object. In the following section it is shown how a change of this parameter influences the finite fixed points and thus the final motion mode.

### 3.4.4 Existence of finite fixed points, "Phase diagram"

The dimensionless ratio $I/MR_c^2$ in the function $g_\alpha(\varepsilon)$,

$$g_\alpha(\varepsilon) = \varepsilon - \frac{I}{MR_c^2}\frac{\mathcal{F}_{v,\alpha}(\varepsilon)}{\mathcal{T}_{n,\alpha}(\varepsilon)} \,, \tag{3.31}$$

will be denoted as $C$ from here on. $C$ is determined by the geometry and mass distribution of the considered object. Therefore, for a different object than the disk the value of $C$ is usually different as well. For example, the

moment of inertia for a thin ring with mass $M$ and radius $R$ is $I = MR^2$ which would give $C = 1$.

The curves of $g_\alpha(\varepsilon)$ with $C = 1$ and $\alpha = 0, 1, 3$ are shown in FIG. 3.8. Now, *all* curves have the trivial fixed point $\varepsilon = 0$ as stable and only fixed point. This is a significant change , as for $\alpha = 0$ a finite stable fixed point existed and for $\alpha = 3$ the unstable fixed point $\varepsilon_0$ partitioned the region for $\varepsilon$, for which either $\varepsilon = 0$ or $\varepsilon \to \infty$ is the attractive fixed point. This example illustrates how the value $C$ changes the function $g_\alpha(\varepsilon)$ and with that the final motion modes of the considered object. For a certain value of $C$ the functions $g_\alpha(\varepsilon)$ will only have positive values and therefore $\varepsilon \to \infty$ is the attractive trivial fixed point, except the motion starts with pure spinning $\varepsilon = 0$, i.e. without sliding. The values $C$ for which the function $g_\alpha(\varepsilon)$ has a finite fixed point are different for every $\alpha$ and are contained in a range with upper and lower bounds. This range, for which the function $g_\alpha(\varepsilon)$ has a finite fixed point $\varepsilon_0$ shall be determined now, by calculating the zeros of $g_\alpha(\varepsilon)$:

$$g_\alpha(\varepsilon) = \varepsilon - C\frac{\mathcal{F}_{\mathrm{v},\alpha}(\varepsilon)}{\mathcal{T}_{\mathrm{n},\alpha}(\varepsilon)} \stackrel{!}{=} 0 \ . \tag{3.32}$$

But this only gives the finite fixed point, if it exists, for a given value $C$.

Thus, the question is asked in an other way:

*What value must $C$ assume, so that a finite fixed point at $\varepsilon_0$ exists?*

This can be answered by solving EQ. (3.32) for $C$:

$$C = \varepsilon_0\frac{\mathcal{T}_{\mathrm{n},\alpha}(\varepsilon_0)}{\mathcal{F}_{\mathrm{v},\alpha}(\varepsilon_0)} \equiv C_\alpha(\varepsilon_0)$$

The function $C_\alpha(\varepsilon_0)$ can be interpreted as follows: if an object has a moment of inertia $I = C_\alpha(\varepsilon_0)MR_c^2$, then its function $g_\alpha(\varepsilon)$ has a finite fixed point at $\varepsilon_0$. $C_\alpha(\varepsilon_0)$ is shown as function of $\varepsilon_0$ for $\alpha = 0, 1$ and 3 in FIG. 3.9. For all shown values $\alpha$ each function $C_\alpha(\varepsilon_0)$ has a lower and an upper limit. These upper and lower limits are summarized in TAB. 3.2. Assuming that $C_\alpha(\varepsilon)$

| | $C_0(\varepsilon_0)$ | $C_1(\varepsilon_0)$ | $C_3(\varepsilon_0)$ |
|---|---|---|---|
| $\lim_{\varepsilon_0\to 0}$ | 2/3 | 1/2 | 1/3 |
| $\lim_{\varepsilon_0\to\infty}$ | 1/4 | 1/2 | 1 |

Table 3.2: Upper and lower limits of $C_\alpha(\varepsilon_0)$ for $\alpha = 0, 1, 3$

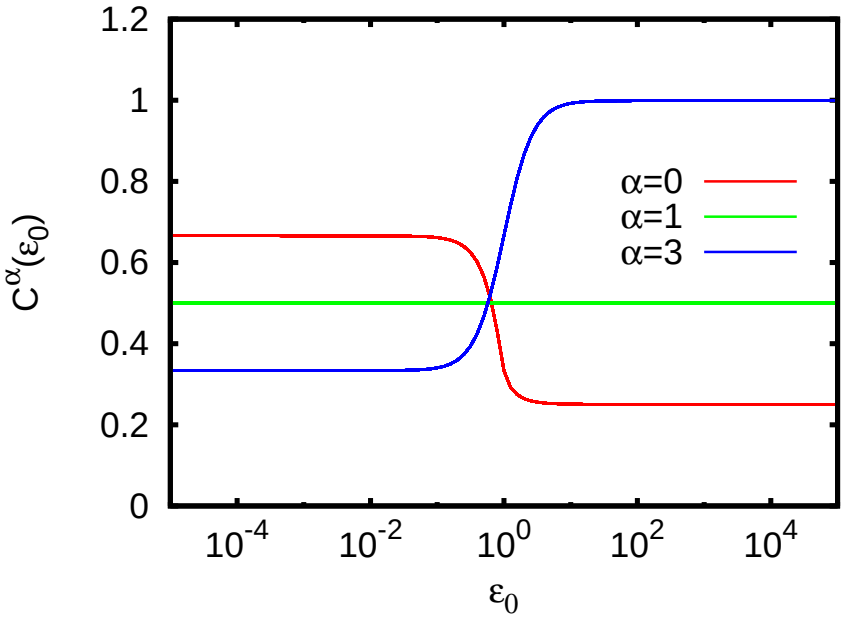


Figure 3.9: The range of the function $C_\alpha(\varepsilon)$ for three different values of $\alpha$. There are upper and lower limits for each function, which are reached at $\varepsilon_0 = 0$ and $\varepsilon_0 \to \infty$. That means, that for $C_\alpha(\varepsilon_0)$ below or beyond these limits no finite fixed point $\varepsilon_0$ exists. The mapping of $C_\alpha(\varepsilon_0)$ is bijective for $\alpha \neq 1$.

is a monotonous function of $\varepsilon_0$, which is determined by the monotony of the friction force and torque, an interval $\mathcal{I}_\alpha = (c_{\alpha,\min}, c_{\alpha,\max})$ is defined, with

$$\begin{aligned} c_{\alpha,\min} &= \min\left\{\lim_{\varepsilon_0\to 0} C^\alpha(\varepsilon_0), \lim_{\varepsilon_0\to\infty} C^\alpha(\varepsilon_0)\right\} \\ c_{\alpha,\max} &= \max\left\{\lim_{\varepsilon_0\to 0} C^\alpha(\varepsilon_0), \lim_{\varepsilon_0\to\infty} C^\alpha(\varepsilon_0)\right\} . \end{aligned}$$

That the interval limits are defined by the limits $\varepsilon_0 \to 0$ and $\varepsilon_0 \to \infty$ makes it possible to use the approximations for friction force and torque of Sec. 3.3. With that, the interval $\mathcal{I}_\alpha$ can be determined for arbitrary $\alpha > 0$. Substituting the corresponding approximated dimensionless friction force and torque listed in Tab. 3.1 into the function $C_\alpha(\varepsilon_0)$ gives:

$$\begin{aligned} \lim_{\varepsilon_0\to 0} C_\alpha(\varepsilon_0) &= \varepsilon_0 \frac{2/(\alpha+3)}{\varepsilon_0} &&= \frac{2}{3+\alpha} , \\ \lim_{\varepsilon_0\to\infty} C_\alpha(\varepsilon_0) &= \varepsilon_0 \frac{\varepsilon_0^{(\alpha-1)}(1+\alpha)/4}{\varepsilon_0^\alpha} &&= \frac{1+\alpha}{4} . \end{aligned}$$

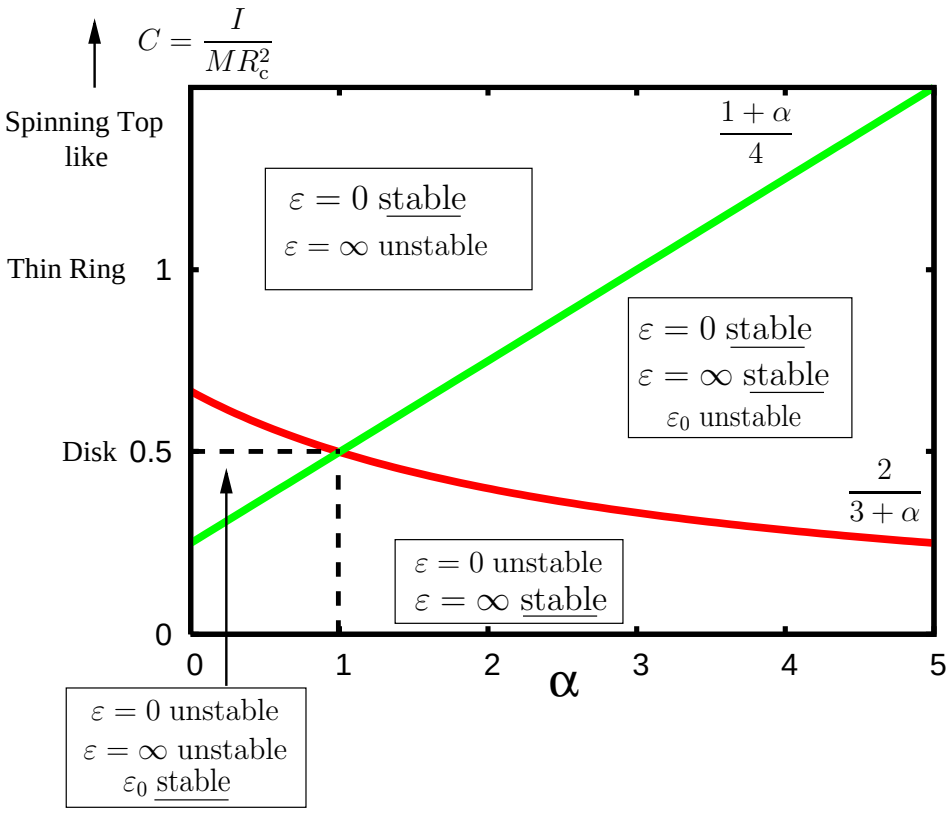


Figure 3.10: The "phase diagram" for the pair $(C, \alpha)$ shows the regions of stable, unstable and finite fixed points.

Afterwards it becomes clear why the interval boundaries $c_{\alpha,\min}$ and $c_{\alpha,\max}$ were defined with the minimum and maximum function, respectively. As long as $\alpha < 1$, the upper limit of $\mathcal{I}_\alpha$ is located at $\varepsilon_0 = 0$, while it changes to $\varepsilon_0 \to \infty$ for $\alpha > 1$. It can be shown that for $\alpha = 0, 1, 3$ the same interval limits are obtained from equations (3.33) as already derived and listed in TAB. 3.2.

Finally, one can now determine for every $\alpha$ the interval $\mathcal{I}_\alpha$ of C-values for which a finite fixed point $\varepsilon_0$ exists. If for a given $\alpha$ and moment of inertia $I$ the value $C = I/MR_c^2$ is an element of the corresponding interval $\mathcal{I}_\alpha$, then the function $g_\alpha(\varepsilon)$ has a finite fixed point. If $C < c_{\alpha,\min}$ then $g_\alpha(\varepsilon)$ is positive for all $\varepsilon$ and the fixed point $\varepsilon = \infty$ is stable, while for $C > c_{\alpha,\max}$ all values $g_\alpha(\varepsilon)$ are negative and the trivial fixed point $\varepsilon = 0$ is stable. The function $C_1(\varepsilon_0)$ is special, because it does not provide a range of possible values for $C$, but only the single value $1/2$, which when put into $g_1(\varepsilon)$ gives a continuum of semistable points.

It is now assumed that the dimensionless friction force $\mathcal{F}_{\mathrm{v},\alpha}(\varepsilon)$ and torque $\mathcal{T}_{\mathrm{n},\alpha}(\varepsilon)$ are strictly monotonous functions for all $\alpha \neq 1$, which is it at least true for the explicitly calculated values $\alpha = 0, 1, 3$ and can be deduced for all odd $\alpha$ from the analytic expressions.(see APP.A). Then the value $C_\alpha(\varepsilon_0)$ is different for different $\varepsilon_0$ and the mapping

$$C_\alpha(\varepsilon) : [0, \infty] \to [c_{\alpha,\min}, c_{\alpha,\max}]$$

is *bijective* and for every $C \in [c_{\alpha,\min}, c_{\alpha,\max}]$ the function $g_\alpha(\varepsilon)$ can have *only one* finite fixed point.

The "phase diagram" in FIG. 3.10 shows where in addition to $\varepsilon = 0$ and $\varepsilon \to \infty$ a third fixed point $0 < \varepsilon_0 < \infty$ exists and which of them is stable for a given pair $(C, \alpha)$. Thus, one can for any $\alpha$ and $C = I/MR_\mathrm{c}^2$ read off, what will be the final motion mode and wether it depends on the initial $\varepsilon_i$. The region of stable $\varepsilon = 0$ and $\varepsilon = \infty$ gets larger with increasing $\alpha$. As can be read off EQ. (3.33) the upper limit increases linearly with $\alpha$, while the lower limit approaches zero asymptotically. For increasing $\alpha$ the region with the unstable finite fixed point $\varepsilon_0$ and stable $\varepsilon = 0$ and $\varepsilon \to \infty$ broadens and becomes the dominant region for large enough $\alpha$

### 3.4.5 Numerical examples

In this section it is shown with numerical simulations, that for a given $\alpha$ and $C$ the corresponding stable fixed point is approached. An object, constructed from two disks, is considered for which the value $C$ can be changed to an arbitrary value. The dynamic equations of this object are then integrated numerically. The dynamics for two different exponents of the friction force and torque were compared. They are $\alpha = 0$ and $\alpha = 3$, as the analytic solutions in these cases were at hand. The friction with $\alpha = 1$ is left out, as it does not provide stable or unstable finite fixed points.
Before doing this, a look is taken at the stopping time for the different values of $\alpha$.

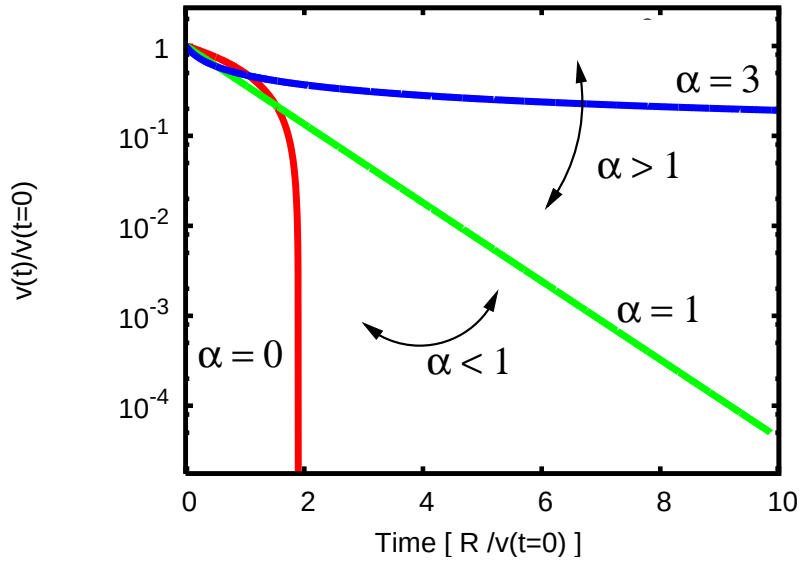


Figure 3.11: The graph shows the time evolution of the velocity for three different $\alpha = 0, 1$ and 3. From Eq. (3.34) it follows that for $\alpha < 1$ the velocity vanishes in finite time, which is confirmed by the curve for $\alpha = 0$. The exponential time dependence of the velocity for $\alpha = 1$ is validated as well and also the asymptotical approach to zero of the sliding velocity for $\alpha > 1$ by the curve for $\alpha = 3$.

### Stopping times

It is interesting whether the time the moving object needs to come to rest completely is finite or infinite. Thinking of Coulomb friction, $\alpha = 0$, it has been shown theoretically, that the existence of the finite stable fixed point leads to a stop of spinning and sliding motion at the same time. That this takes finite time was observed in experiments with the disk (see Sec. 3.2.2). Can this be shown analytically too? To answer this question, it is sufficient to consider an equation of motion of an object on which only a sliding friction force depending on $[v(t)]^\alpha$ acts:

$$\frac{dv(t)}{dt} = -\frac{\gamma^\alpha F_\mathrm{n}}{M}[v(t)]^\alpha \tag{3.33}$$

Formal integration leads to:

$$v(t) = [C_2 - (1-\alpha)Kt]^{\frac{1}{1-\alpha}} , \tag{3.34}$$

where

$$K = \frac{\gamma^\alpha F_\mathrm{n}}{M}$$

and with the initial velocity $v(t=0)$ the integration constant is

$$C_2 = [v(t=0)]^{(1-\alpha)} \ .$$

For $\alpha < 1$, the exponent in Eq. (3.34) is positive and larger than one. The velocity vanishes in finite time. If $\alpha > 1$, the exponent is negative and smaller than one. In this case the sliding velocity vanishes only asymptotically, i.e. in infinite time. A formal integration of Eq. (3.33) with $\alpha = 1$ shows, that the velocity vanishes exponentially in time. Thus the sliding velocity decreases faster than for $\alpha > 1$.

Now the coupled friction force and torque is considered again. The equations of motion for a sliding and spinning disk of radius $R$ have been simulated for the friction force and torque with $\alpha = 0, 1$ and 3. The time integration of the equations of motion (3.25) was done with the Verlet-method [40] and for the calculation of the coupled friction force and torque the corresponding analytic solutions were used.

The absolute value of the total velocity $v(t)$ of the disk is shown as function of time in Fig. 3.11. The predictions derived from Eq. (3.34) are confirmed: for $\alpha < 1$ the velocity vanishes in finite time, which is demonstrated by the curve for $\alpha = 0$. Also the exponential time dependence for $\alpha = 1$ and the asymptotical approach to zero for $\alpha > 1$, shown by the curve for $\alpha = 3$, are confirmed.

For friction force and torque with $\alpha < 1$ the motion of the disk will stop completely in finite time, while for $\alpha \geq 1$ this will take infinite time.

### Final motion modes for a double disk

The disk and the thin ring were two examples for objects, which gave the values $C = 1/2$ and $C = 1$, respectively. While $C = 1/2$ is element of the interval $\mathcal{I}_\alpha$ for $\alpha = 0, 3$, the value $C = 1$ served as example for a case where $C > c_{0,\max}$ and $C > c_{3,\max}$. A very simple object is now considered, which provides arbitrary values for $C$ and is called "double disk". This double disk is just the fusion of two discs. One of the disks has radius a $R_\mathrm{c}$, is considered massless and provides contact with the support. The second disk with radius $R$ and mass $M$ is mounted atop the other. Consequently, the mass the and moment of inertia of this construct are determined by the upper disk and the value for $C$ then only depends on the ratio $R^2/(2R_\mathrm{c}^2)$. In principle, it

should be possible to construct a double disk with the desired $C$ by choosing an appropriate ratio of the radii.

The numerical simulations were done for dry friction, $\alpha = 0$, and friction depending on the cubic velocity, $\alpha = 3$. The reason, is that these examples illustrate quantitatively all interesting cases of finite fixed points and their analytic solutions were at hand. For other $\alpha$ no significant different behaviour is expected. The dynamics with friction linear in $\mathbf{v}$ is not considered here because it is trivial.

With $c_{\alpha,\min}$ and $c_{\alpha,\max}$ one can find the limits for the ratio of radii, for which a finite fixed point exists:

$$c_{\alpha,\min} < \frac{R^2}{2R_\mathrm{c}^2} < c_{\alpha,\max} \;\Rightarrow \sqrt{2c_{\alpha,\min}} < \frac{R}{R_\mathrm{c}} < \sqrt{2c_{\alpha,\max}}$$

This gives for $\alpha = 0$

$$\frac{1}{\sqrt{2}} < \frac{R}{R_\mathrm{c}} < \frac{2}{\sqrt{3}} \tag{3.35}$$

which is in agreement with [29]. For $\alpha = 3$ it is

$$\sqrt{\frac{2}{3}} < \frac{R}{R_\mathrm{c}} < \sqrt{2}\,. \tag{3.36}$$

The simulations were done for three different values of $R/R_\mathrm{c}$, which are chosen within the range, $R/R_\mathrm{c} = 1$, and close to the corresponding limit values given in Eq. (3.35) and Eq. (3.36), but not equal. For each ratio of radii seven different initial velocity ratios $\varepsilon_i$ were chosen, while six of them were the same for both friction types and the seventh was chosen equal to the value of the finite fixed point $\varepsilon_0$, which would be present if the ratio of radii is within the given range. For the numerical integration again the Verlet-Method [40] was used.

The results are shown in Fig. 3.13. The velocity ratio $\varepsilon$ is plotted as a function of the dimensionless angular velocity $\omega_\mathrm{n}^*$, which was measured in units of initial angular velocity. The simulations were stopped after both of the velocities got smaller than $10^{-4}$ in units of their initial velocity. In the graphs the time evolves from the right to the left. The red curve shows the time evolution of the seventh initial condition for $\alpha = 0$ with $\varepsilon_i \approx 0.653$ and the green curve indicates this initial condition for $\alpha = 3$ with $\varepsilon_i \approx 0.577$.

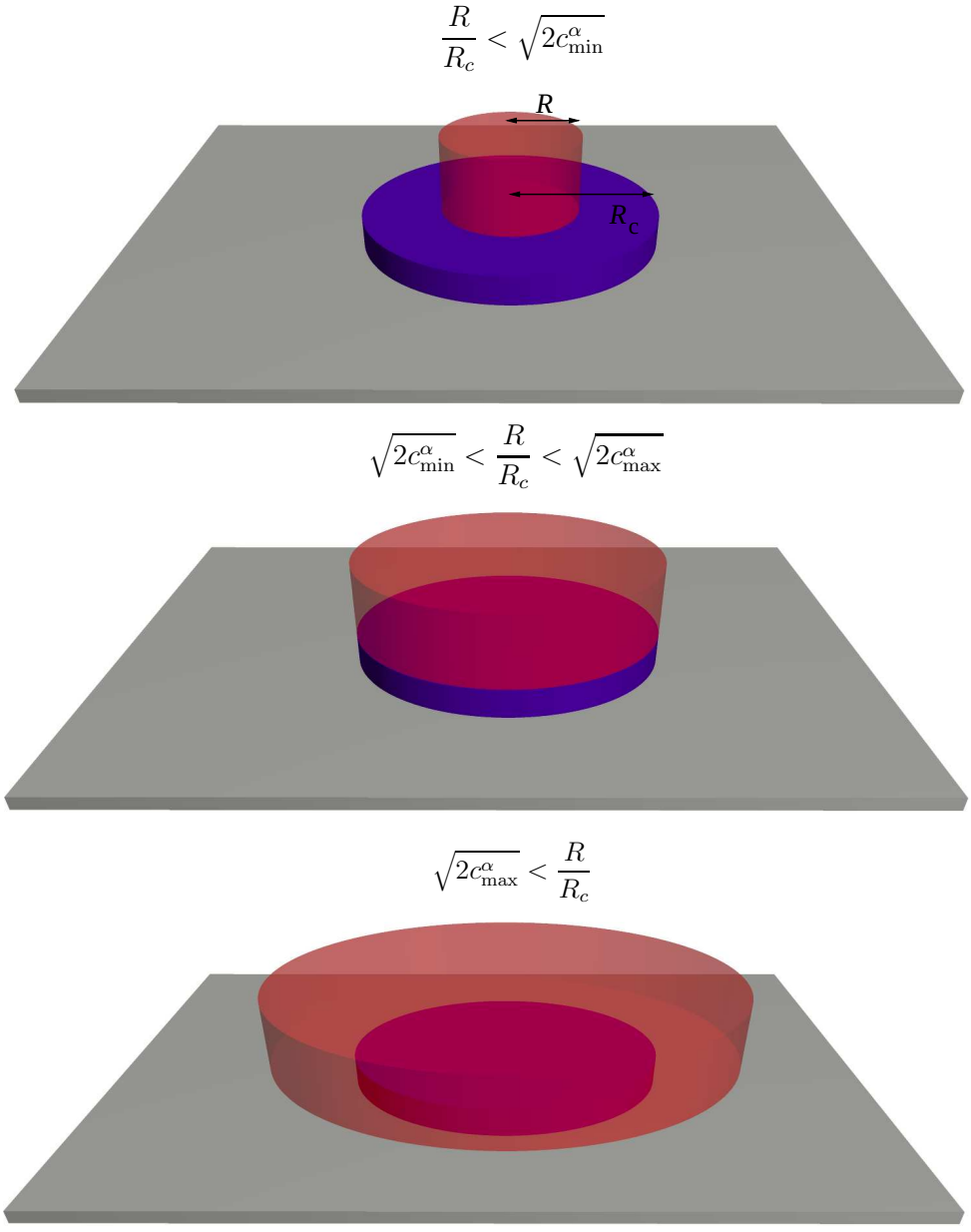


Figure 3.12: The model of the double disk. The upper disk carries a mass $M$ and has a radius $R$, while the massless disk of radius $R_c$ beneath makes contact with the support. Shown are three different cases of radii ratio $R/R_c$.

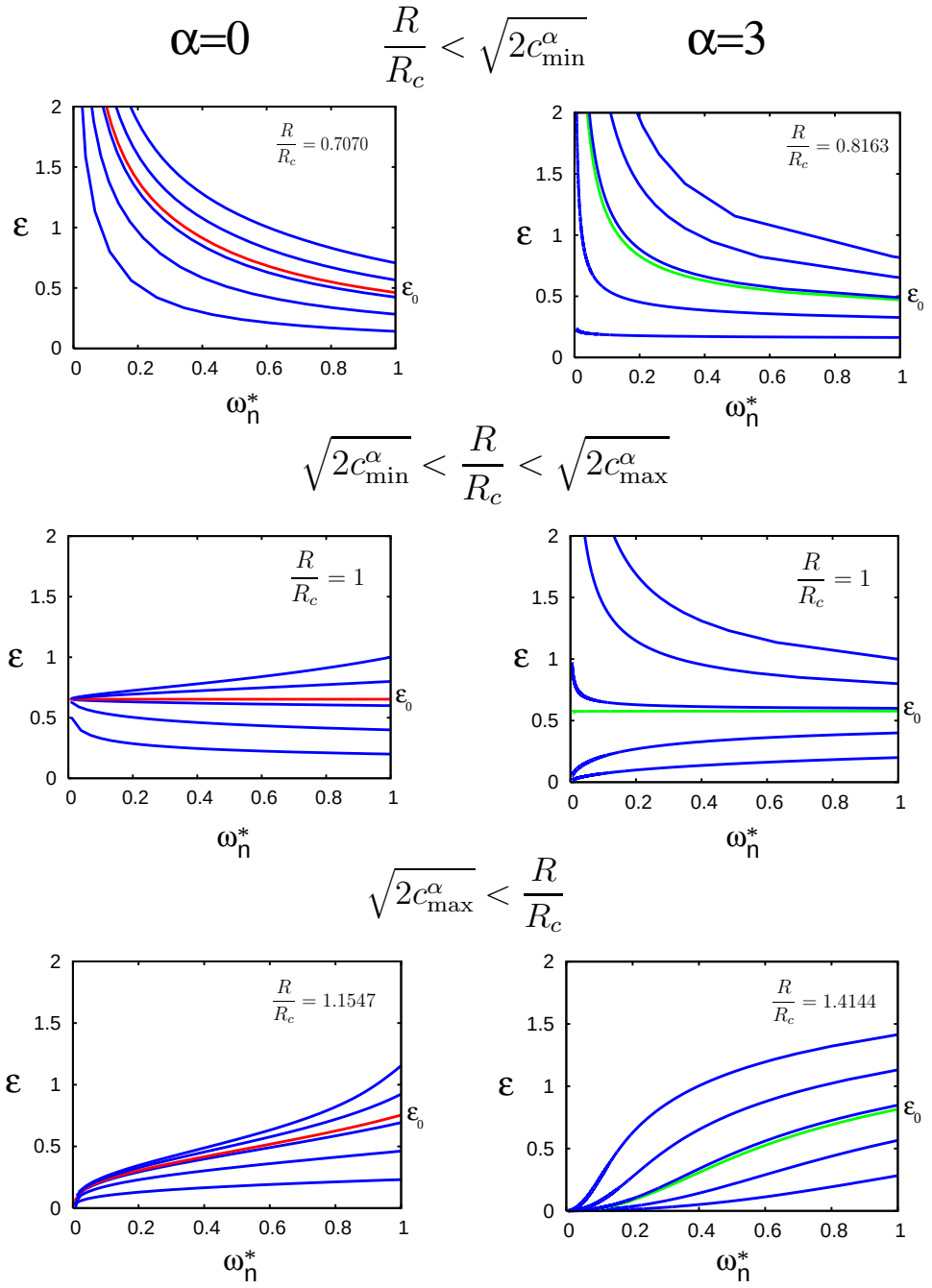


Figure 3.13: The dynamical equations EQ. (3.25) were integrated numerically for the two friction types Coulomb friction ($\alpha = 0$) and cubic friction ($\alpha = 3$) with six different initial conditions and three different radii ratios. Shown is the velocity ratio $\varepsilon$ as a function of the angular velocity $\omega^*_{\mathrm{n}}$ which is normalized to the initial velocity.

As expected, the curves for the case $R/R_c < \sqrt{2c_{\alpha,\min}}$ show that the final motion mode is independent of the initial velocities for both values of $\alpha$. All curves show that $\varepsilon \to \infty$ and the final motion mode is dominated by sliding. If the ratio is larger than $\sqrt{2c_{\alpha,\max}}$, then the final motion mode is spinning, as $\varepsilon = 0$ is the stable fixed point. More interesting is the case of $R/R_c = 1$, where all blue curves for $\alpha = 0$ converge to the fixed point $\varepsilon_0$ no matter what the initial velocity is. The final motion mode is stopping of spinning and sliding at the same time. For $\alpha = 3$ it is recognized that with $\varepsilon_0$ the set of initial $\varepsilon$ is divided into two parts. For $\varepsilon_i > \varepsilon_0$ the fixed point is $\varepsilon = \infty$ corresponding to a final motion mode of sliding. The curves with $\varepsilon_i < \varepsilon_0$ have $\varepsilon = 0$ as fixed point and spinning is the final mode. For $\varepsilon_i = \varepsilon_0$ (green curve) the ratio is not changed during the time evolution. For $\alpha = 0$ this is not surprising as it is the value of the stable attractive fixed point, but for $\alpha = 3$ it is an unstable fixed point.
These numerical experiments show the expected dynamical behaviour of the velocities concluded from the autonomous differential equation Eq. (3.27).

It is worth noting that the final motion modes for an object are of practical interest in the research of robotics, for example in the so-called *inverse sliding problem* [30,31]. Up to now a uniform pressure distribution was assumed. In the following section the effect of a nonuniform pressure distribution on the coupled friction force and torque is discussed.

## 3.5 Nonuniform pressure distribution

The sliding and spinning disk was used as a simple and illustrative example, for which the local pressure is the same (uniform) everywhere. However, in general the pressure distribution over the contact area will be nonuniform. For every rotationally symmetric and radially dependent pressure distributions, like the famous Hertz pressure [22, 41], the friction force component $F_{\perp,0}$ will be zero [27], and this also holds for every value of $\alpha$ of the coupled friction force and torque. Only a rotationally asymmetric pressure distribution gives a nonzero friction force component $F_{\perp,0}$ and the sliding and spinning object shows a curved sliding path.

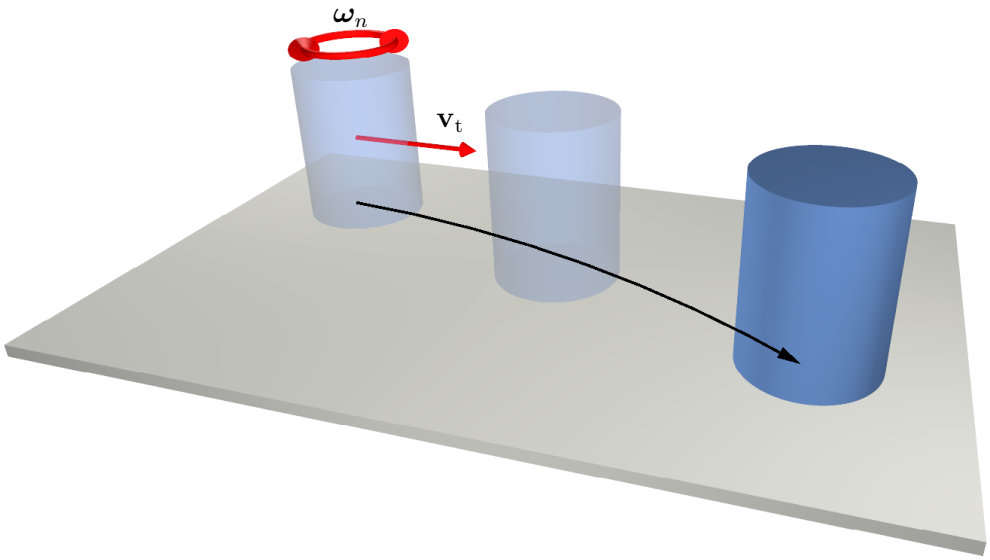


Figure 3.14: A sliding and spinning cylinder will have a curved path due to friction at its bottom. The friction causes a torque with respect to the center of mass and thus leads to a pressure increase in the contact area in front of the sliding direction. The coupling of the friction on the velocities now gives a friction force component perpendicular to the sliding direction and spinning axis. The effect is visible in a curved sliding path.

### 3.5.1 Sliding and spinning cylinder

Consider a cylinder of height $H$ and radius $R$ sliding on its flat side with velocity $\mathbf{v}_\mathrm{t}$ and spinning with angular velocity $\boldsymbol{\omega}_n$, like sketched in FIG. 3.14. The sliding friction force $\mathbf{F}_\alpha$ at the bottom causes a torque at the center of mass (COM), that wants the cylinder to tip over in sliding direction. Assuming that the cylinder does not topple, i.e. does not lift up at any point of the contact area, the torque is compensated by a pressure increase at the leading edge (front) of the cylinder and consequently a pressure decrease at the trailing edge (back). In terms of polar coordinates, the pressure changes with both distance $r$ from the center and angle $\varphi$. Since the real pressure distribution can be rather complex, for simplicity a linear pressure correction is assumed. It is a correction to the uniform pressure distribution, which decreases the pressure from the front of the contact area to the back linearly. The forces and pressure distribution for the sliding and spinning cylinder in this situation is illustrated in FIG. 3.15. The center of mass (COM) is at the height $H/2$ and the torque which is to be compensated is $F_\alpha H/2$, where

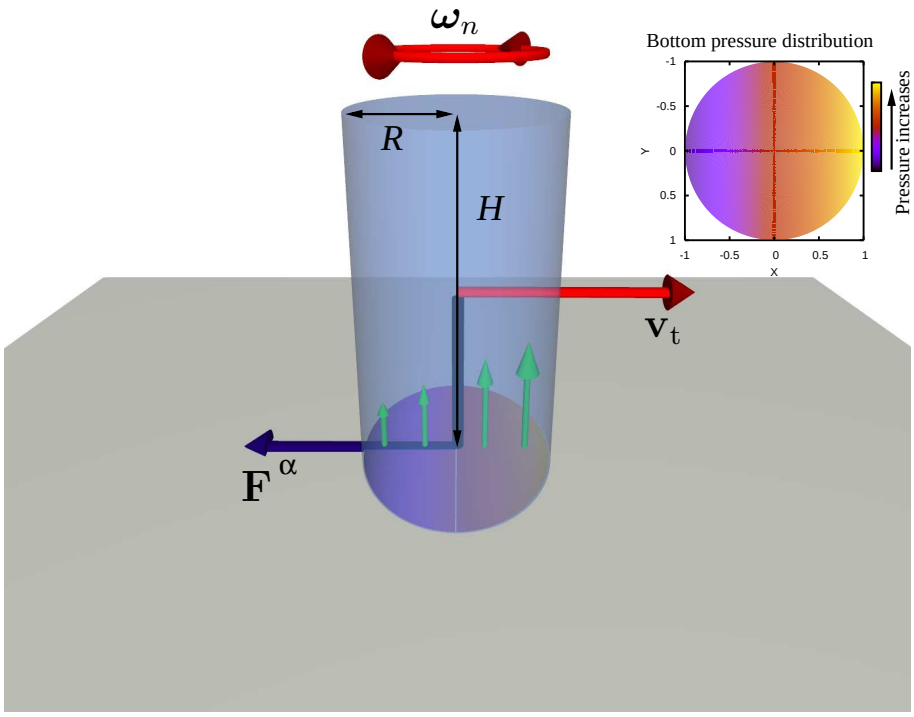


Figure 3.15: Sketch of a cylinder of height $H$ and radius $R$, which slides with the velocity $\mathbf{v}_\mathrm{t}$ and spins with the angular velocity $\omega_\mathrm{n}$. The friction force $\mathbf{F}_\alpha$ and the pressure distribution $P(r, \alpha)$ once at the bottom of the cylinder (green arrows) and as (qualitative) gradient plot in the upper right corner are shown as well.

$|\mathbf{F}_\alpha| = F_\alpha$. The pressure distribution $P(r, \varphi)$ then is:

$$P(r, \varphi) = \frac{F_\mathrm{n}}{\pi R^2} + \frac{2F_\alpha H}{\pi R^4} r \cos\varphi \tag{3.37}$$

For this pressure distribution the friction force and torque for Coulomb friction, $\alpha = 0$, were calculated numerically with the trapezoid rule [40]. The resulting dimensionless friction force and torque are shown in FIG. 3.16. The difference between the friction force for the uniform pressure distribution (FIG. 3.4) and this nonuniform pressure distribution is, that now its component $\mathbf{e}_\perp$ is nonzero, i.e. the (dimensionless) friction force $\mathcal{F}_{\perp,0}(\varepsilon)$ (black line FIG. 3.16). The graph of $\mathcal{F}_{\perp,0}$ looks similar to that of the friction torque $\mathcal{T}_{\mathrm{n},0}(\varepsilon)$, having the same limits at $\varepsilon = 0$ and $\varepsilon \to \infty$. The friction torque $\mathcal{T}_{\mathrm{n},0}(\varepsilon)$ and sliding friction $\mathcal{F}_{\mathrm{v},0}(\varepsilon)$ are not changed by this pressure distribution and thus are the same as for the uniform pressure distribution. $F_\alpha$ is the sliding friction force component $\mathbf{F}_0 \cdot \mathbf{e}_v = -\mu_d F_\mathrm{n} \mathcal{F}_{\mathrm{v},0}(\varepsilon)$ and is included

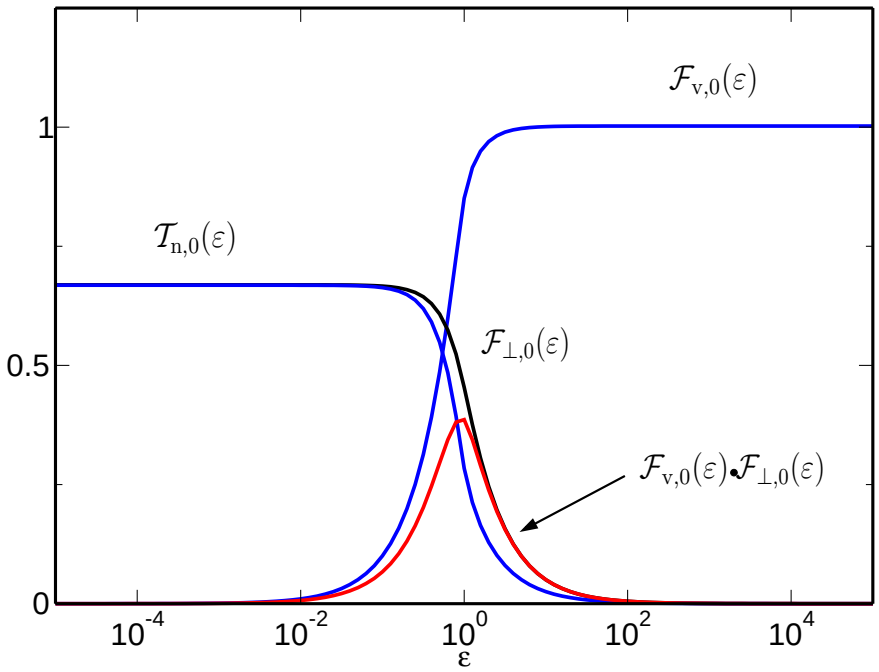


Figure 3.16: The dimensionless Coulomb friction force and torque for the distribution $P(r,\varphi)$ from Eq. (3.37). The friction force $\mathcal{F}_{\perp,0}(\varepsilon)$ is not zero, as it was for the uniform pressure distribution.

in the net friction force $F_{\perp,0}(\varepsilon)$ giving:

$$F_{\perp,0}(\varepsilon) = \mu_d^2 F_{\mathrm{n}} \frac{H}{R} \mathcal{F}_{\mathrm{v},0}(\varepsilon)\mathcal{F}_{\perp,0}(\varepsilon) \tag{3.38}$$

The product $\mathcal{F}_{\mathrm{v},0}(\varepsilon)\mathcal{F}_{\perp,0}(\varepsilon)$ is represented by the red curve in Fig. 3.16 and shows the $\varepsilon$ dependence of $F_{\perp,0}$. As $F_{\perp,0}$ is induced by the spinning motion, it is clear that $\mathcal{F}_{\perp,0}(\varepsilon)$ vanishes for decreasing angular velocity, i.e. for $\omega_{\mathrm{n}} \to 0$ or $\varepsilon \to \infty$ as can be seen in Fig. 3.16. It also vanishes for decreasing sliding velocities, i.e. for $\varepsilon \to 0$, as a purely rotating cylinder should not be translated in any direction. Further, without sliding there is no sliding friction causing a torque on the COM and in turn there is no asymmetry in the pressure distribution. Thus, the friction force $F_{\perp,0}$ also vanishes for $\varepsilon \to 0$. The lateral friction force $F_{\perp,0}(\varepsilon)$ is in opposite direction to $\mathbf{e}_\perp$, thus the lateral deviation of the cylinder from its (initial) sliding direction is in direction of $-\mathbf{e}_\perp = \mathbf{e}_v \times \mathbf{e}_\omega$. A sliding cylinder, which is spinning counterclockwise, will move to the right viewed in sliding direction. For clockwise spinning, the lateral motion would be to the left. Phenomenologically, lateral deviations from the translation direction induced by rotation are also known for objects

in a fluid or gas, which is attributed to the Magnus effect [42]. But one has to note, that the underlying physical phenomena are different.
The aspect ratio of the cylinder $H/R$ influences the magnitude of $F_{\perp,0}(\varepsilon)$. For the disk used in the experiments (Sec. 3.2.2) the aspect ratio was 1/4, which is relatively small and explains why only very small deviations from the sliding path were observed [12].
For other friction than $\alpha = 0$ the net friction force component $F_{\perp,\alpha}$ is nonzero as well and its dimensionless friction force is similar to the dimensionless friction torque.

Penner [43] investigated theoretically and experimentally the sliding and spinning motion of a cylindrical shell or hollow cylinder standing on its end. He formulated the equations of motion and a pressure distribution with a larger pressure in front and smaller in the back, similar to the one used here (Eq. (3.37)). Analytic expressions for the friction force and torque were not given in [43]. The dynamical equations were integrated numerically and the obtained results were compared to experimental results. The theoretical paths, obtained from the numerical integration, are very well in line with the experimental results, where the lateral deflection increases with the initial angular velocity and the height of the cylinder. The direction of deflection observed in the experiments is the same as mentioned here. In Fig. 3.17 the theoretical and experimental results for the hollow cylinder are shown. Shegelski et al. showed in [44], that the net lateral deflection of a rapidly rotating cylinder, where $\omega_\mathrm{n} R_\mathrm{c} \gg v_t$ ($\varepsilon \ll 1$), can be as large as the net displacement in the initial direction of motion. For large enough initial angular speed, the trajectory of the cylinder can have the form of a spiral with a large number of loops. Such large-curl trajectories can be observed experimentally with a curling rock on a smooth, flat sheet of ice, but handedness of the spiral is different.

Several aspects of the motion of a curling rock on ice are of great physical interest. One of these is that its motion differs from that of a cylinder on a dry surface and thus can not be simply explained in these terms. A more detailed examination of the ice surface, the curling rock and its observed different motions is needed. This is the topic of the next section. It is worth noting that up to now no complete theoretical explanation and theory for the motion of the curling rock exists. That emphasizes, that this is a more complex problem than the sliding cylinder with dry friction.

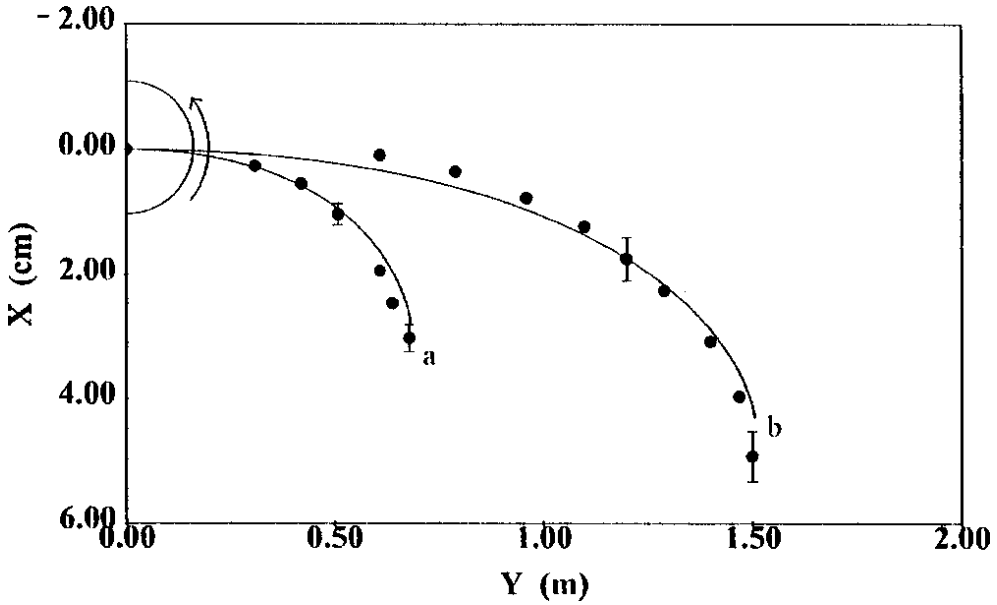


Figure 3.17: Shown are the experimental positions (black dots) of two sliding pipe sections (hollow cylinders) as compared with the corresponding theoretical paths (solid lines). The two pipe sections started in $Y$ direction with initial sliding velocity $v_{y0} = 1.74$ m/s and $\omega_0 = 10.2$ rad/s for (a) and with $v_{y0} = 2.61$ m/s and $\omega_0 = 10.6$ rad/s for (b). (Graphic taken from [43].)

### 3.5.2 Curling rock on ice vs. cylinder on a dry surface

Curling is a sport, where cylindrically symmetrical granite rocks, called curling rocks slide and rotate over a sheet of ice. It is generally believed, that the game has been invented in Scotland in the 16th century and was very popular at that time, provided that in winter the climate was cold enough to ensure good ice conditions [45].

A standard curling rock is a disk-shaped object and has a mass of 20 kg, a height of 11.4 cm and is 29 cm in diameter. The bottom surface of the curling rock is not flat, but concave and the rock moves on the ice on a narrow running band, which has a diameter of approximately 12.5 cm and width of $4 - 5$ mm [46]. This running band is prepared by abrasion so as to increase friction between the granite and the ice. The profile of a curling rock is shown in FIG. 3.18. Further details about the playing field, which is called rink, and basic rules of the game can be found for example in reference [45, 48]. It may be surprising, that despite the long history of curling, only recently

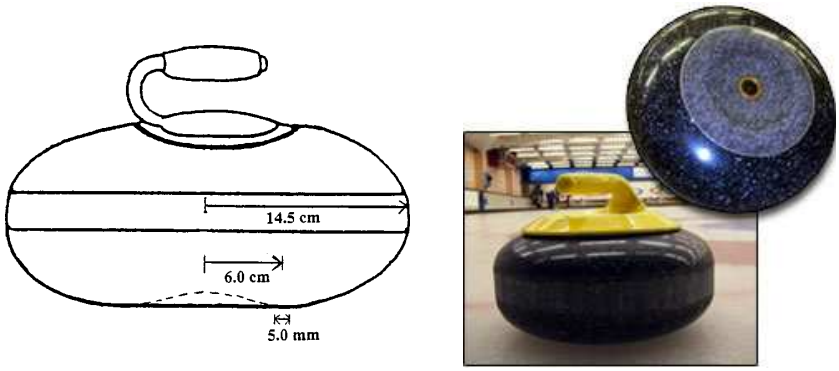


Figure 3.18: On the left the profile of a curling rock is shown. The running band at the bottom surface with a radius of $6.0$ cm and $5.0$ mm width is indicated [43]. On the right an image of the curling rock and its bottom is shown [47]

the question for the underlying physical reasons for the observed motion of curling rocks has been addressed in a physically reasonable approach.

For curling a nominally flat ice surface at a temperature of $-5°$C is *pebbled* by spraying droplets of water over it. The droplets freeze immediately and form a surface containing a vast number of millimeter-sized bumps, also called pebbles. The preparation of the surface is a key part for the game and there is a considerable art in preparing a good curling surface [46]. The condition of the ice surface is very important for the curling rock motion, therefore Shegelski et al. investigated the curling rock motion on *flooded ice* as well. This was prepared, by flooding the surface with water and let it freeze. The obtained ice surface is quite flat, but not perfectly smooth.

### Observations

Some examples of observations are listed below, which are of physical interest:

- As already mentioned, the trajectory of a curling rock is not straight, but *curved* instead.Therefore the sport is called "curling".
- The lateral motion, the "curl", on ice is in *opposite* direction to that of a geometrically similar cylinder sliding over a smooth dry surface.
- The net lateral displacement can be so *large* that it is not easily understood, which also holds for its *weak* dependence on the initial angular velocity.

The first and second point can be observed at a curling shot called draw shot, where the translation dominates the motion and rotation is low. The curling rock has a relatively large initial sliding velocity traveling 28 m in approximately 20 s, i.e. $v_t \sim 1.4$ m/s, while the curling rock has a low number of rotations, approximately one to four full rotations, which corresponds to an initial angular velocity ranging from 0.3 to 1.4 rad/s [43]. It is also reported, that a rock with a too large angular velocity, a so called spinner, will travel farther and show a trajectory with less curl [48]. This is attributed to the effect of dynamical reduction of friction force and torque similar to that known for dry friction, shown in Sec. 3.2.2, with $\alpha = 0$. Remember, that the existence of the stable finite fixed point for $\alpha < 1$, also implies the dynamical reduction of friction force and torque. Shegelski et al. found, that for a draw shot on pebbled ice the sliding and rotational motion typically stop a the same time, within the resolution of their experiments. From this and the initial values for sliding and angular velocity, one gets $\varepsilon \gg 1$ and can conclude, that a finite fixed point exists for a draw shot. The opposite (extreme) motion to the draw shot is the case of a rapidly rotating, slowly sliding (RRSS) curling rock. In this case, the curling rock shows a lateral motion as well, but here the lateral displacement, approx. $0.5 - 1.2$ m, is of the same order as the displacement in initial direction, approximately $3 - 4$ m [46]. The lateral displacement is larger on flooded ice than on pebbled ice. Shegelski et al. observed, that the translational motion stops prior to the rotational motion, which they explain with the variations in ice pebble heights. A slow translating curling rock can become trapped in a "well", while its rotational motion continues. For an RRSS shot the initial velocity ratio is $\varepsilon \ll 1$. For both shots, draw shot and RRSS, Shegelski et al. also derived approximate expressions for coupled friction force and torque as introduced here for $\varepsilon \ll 1$ and $\varepsilon \gg 1$ in Sec. 3.3, differing only by a factor of order unity [46]. With these approximations the exponent $\alpha$ could be evaluated from experimental data.

It is worth to take a look at the interface between the running band of the curling rock and the ice, as it plays a crucial role in the observed lateral motion. A.R. Penner argued, that the slightly roughened surface of the running band is responsible for the curl and therefore stated: the rougher the surface, the more the rock curls [43]. Shegelski et al. observed that this is not necessarily true: they compared the curl of curling rocks on ice, one having a polished *granite* running band and one having a polished *stainless steel* running band. One can observe, that both running bands have a smooth surface. The result was, that the granite running band exhibited little or no curl, while the stainless steel running band exhibited an even *larger* curl, than

a regular curling rock. Shegelski et al. concluded from that observation that the interface characteristic is crucial for determining the motion of the curling rock and that a large curl distance does not require a roughened running band. Further it supports their assumption, that the curl is attributed to a thin liquid film between the curling rock and ice.

Not only the opposite curling direction, but also the magnitude of the lateral displacement and the weak dependence of the lateral displacement on the initial angular velocity, require a different explanation than the one given for the sliding and spinning cylinder.

### Models

One can expect that the friction force should be responsible for the curl of a curling rock, as it is the only force acting on the curling rock which has components in the plane of the path. Before considering the various models explaining the curl, it is discussed what kind of friction between the curling rock and ice is acting, as this is controversially discussed in literature as well.

From the friction point of view ice is interesting, because its dynamic friction can be an order of magnitude lower than that of most other crystal systems [2]. This low dynamic friction is normally attributed to a thin water film, acting as lubricant. It was long believed, that this thin water film has its origin in pressure melting, which was proposed by Reynolds. But Bowden has shown that this explanation is not correct as the pressure must be much larger, than the one given usually by the weight and contact area of the objects [6]. Rather, that thin water film is induced by *frictional heating* and thus depends on the sliding velocity [6]. That the frictional heating induces a thin liquid layer is also taken by Penner [43] and (critically reviewed) by Shegelski et al. [46]. For an aluminum block on ice at $-10°\mathrm{C}$ Bowden found the static friction coefficient to be $\mu_s = 0.38$. For the block sliding on ice the dynamic friction coefficient is $\mu_d = 0.34$ at $v_t = 0.03$ m/s and $\mu_d = 0.04$ at $v_t = 5$ m/s. This emphasizes, that pressure melting can not be the origin for the thin water layer in this case, since then the static friction would be much smaller and $\mu_d$ would not be velocity dependent. Besides, experiments show, that during sliding on ice and snow the friction force is proportional to the load [6], indicating that the real area of contact is proportional to the load.

The decrease of the dynamic friction coefficient $\mu_d$ with increasing velocity, at least for the velocities given as example above, inspired researchers to model a velocity dependent dynamic friction coefficient:

$$\mu_d = \gamma v^{\alpha}, \tag{3.39}$$

Penner derived values for $\gamma$ and $\alpha$ by considering the energy produced at each contact point of the running band by the frictional force and assuming that the bulk of the heat is conducted into the ice [2]. The coefficient $\gamma$ contains material parameters and interface properties. With the dimensions and material parameter values for a curling rock Penner gave for $\gamma$ the value 0.0080 and $\alpha = -1/2$, while $v$ is expressed in m/s. The $v^{-1/2}$ dependence is experimentally verified for various sliders on ice [43]. Shegelski et al. derived $\alpha = -1/2$ as well, by combining the equation of heat from the curling rock into the ice with the equation for the amount of energy transferred. But from their experiments with the curling rock they found different values for $\gamma$ and $\alpha$, depending on the type of curling motion. In case of a purely rotating curling rock it is $\gamma_{\text{rot}} = 0.0094\ (\text{m/s})^{\alpha_{\text{rot}}}$ where $-0.82 \leq \alpha_{\text{rot}} \leq -0.52$. For the RRSS shots they found $\gamma_\theta = 0.0103\ (\text{m/s})^{\alpha_\theta}$ with $\alpha_\theta = -0.75$ and for a draw shot it is $\gamma_y = 0.0076\ (\text{m/s})^{\alpha_y}$ with $\alpha_y = -0.19$. These experimental results led Shegelski et al. to the conclusion that one or more assumptions in the theoretical derivation are incorrect. Further, these results are evidence for wet friction and not for dry friction, which would require $\alpha = 0$. Based on this, Shegelski et al. rule out the dry friction model as proposed by Denney [46]. This is further supported by their observation, that the lateral displacement does depend only very weakly on the initial angular velocity. For a dry friction model a linear relation would be expected, like it was shown for the cylindrical shell [43]. Shegelski et al. propose, that the thin liquid film acquires a nonzero velocity due to the adhesion between the granite and water. As it is the thin film providing the force on the rock, the relevant relative velocity is that between rock and liquid and not between rock and the ice surface. Further, the direction of the relative velocity between the thin liquid film and curling rock need not be in the same direction as for the relative velocity between curling rock and ice surface. With this concept, the observed phenomena should be explainend. But the direction of the curl could not be explained within these terms. One approach to explain this, was done with a so called *front-back* asymmetry model. It proposes, that a difference in friction between the leading and trailing halves of the running band shall be responsible for the curl, similar to the situation of the cylinder

[2] For sliding objects with similar thermal properties to that of a curling rock it was found that the bulk of the heat is transferred into the ice [43].

with dry friction. But now the friction at the back half must be larger than at the front half to get the correct curling direction. Penner showed that the friction force at the back must be $10 - 100$ times greater than the friction force of the front half and the initial angular velocity must be larger than found in the game to get a curl distance of 1 m [43]. Further, he showed by an experiment with a full and half curling rock model, that such large difference can not be observed. The front-back model also has problems to explain the weak dependence of the curl on the angular velocity, as it would predict a linear relation. Another model is based on a *left-right* asymmetry in the friction force, where the left and right half of the running band are related to the sliding direction. The rotation causes a different magnitude of the relative velocity at different positions around the running band. This will in turn give a varying friction force around the running band, as long as friction is velocity dependent ($\alpha \neq 0$). But as already known from the explicit calculations of the friction force and torque for $\alpha = 1$, $\alpha = 3$ and in general for odd $\alpha > 0$, there is no net lateral friction force, i.e. $F_{\perp,0}^{(\alpha)} = 0$. One can show that this is true for positive as well as negative $\alpha$, and therefore also for $\alpha = -1/2$, the value derived theoretically for the curling rock sliding on ice. Penner suggested, that the friction force between ice and curling rock is partly adhesive in nature. This adhesive nature is expected to result in a pivoting-like action about contact points on the slower side of running band. For $\mu_d \propto v^{-1/2}$ this would be the left side for a counterclockwise spinning curling rock. Penner suggested further, that this would lead to an increase in the curl with the angular velocity, which is in disagreement with the experimental results [43]. Thus deeper understanding of the adhesive nature of the frictional force is needed according to Penner.

Finally one can conclude, that the motion of a curling rock is a nontrivial problem, which can not be "easily" described in terms of a sliding and spinning cylinder with dry friction. A theoretical model is lacking and the different approaches fail in comparison with experimental results. It seems that Shegelski et al. have a promising approach taking the thin water layer and its relative motion into account, even if, up to now, it is not clear how this explains the direction of the curl.

Negative values for the exponent $\alpha$ give a diverging friction force for vanishing velocities. This is unphysical, if one does not consider a transition to a non-diverging friction force, e.g. positive $\alpha$, for small velocities. From experiments one knows that for smaller velocities as of order $10^{-4}$ m/s the friction force is constant for approximately two orders of magnitude, down to $10^{-6}$ m/s, and decreases for vanishing velocities to a finite value (see FIG. 3.19).

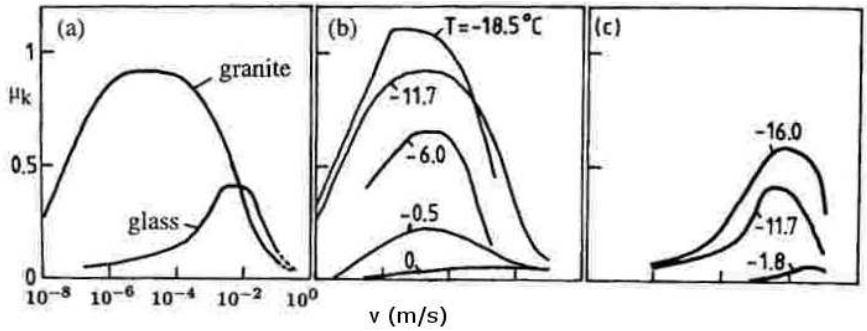


Figure 3.19: The friction coefficient of polycrystalline ice sliding on granite and glass at $-11.7$°C is shown in the left image. The center and right image show the coefficient friction for several different temperatures for granite and glass, respectively [2].

As most of the curl distance of a draw shot is achieved while the curling rock has a sliding velocity of order 1 m/s, the assumption of a velocity dependence like $v^{-1/2}$ seems reasonable for this velocity range. But a theoretical model for the motion of a curling rock on ice should describe the complete velocity range. For an RRSS shot one should take into account that the curling rock travels slowly and the running band rotates on a small area of ice. Therefore the running band passes the same area of ice more often as for a draw shot and the situation at the interface can differ widely, for example concering the thin liquid film. The motion of a curling rock on ice provides a complexity which is intensively investigated and can not be explained in simple terms.

## 3.6 Summary

In this chapter the coupling of dynamic sliding friction force and (normal) friction torque on the basis of a disk was investigated, where the local friction force was assumed to depend on an arbitrary power $\alpha \geq 0$ of the local velocity. A uniform pressure distribution was assumed.

The case of $\alpha = 0$ is the velocity independent Coulomb friction, where the local friction force depends only on the direction of $\mathbf{v}$. The analytic expressions of net friction force and torque were found and their velocity dependence is covered completely by the dimensionless friction force $\mathcal{F}_{\mathrm{v},0}(\varepsilon)$ and friction torque $\mathcal{T}_{\mathrm{n},0}(\varepsilon)$, which are functions of the velocity ratio $\varepsilon = v_t/\omega_{\mathrm{n}}R_{\mathrm{c}}$ only. With $\mathcal{F}_{\mathrm{v},0}(\varepsilon)$ and $\mathcal{T}_{\mathrm{n},0}(\varepsilon)$ it could be shown, that they dynamically reduce

each other. This affects the dynamics of a sliding and spinning disk in a way that it travels farther compared to a purely sliding disk. As another consequence, the reduction leads to a negative feedback mechanism, such that the ratio of sliding and spinning velocities is equilibrated to the universal value of $\varepsilon_0 \approx 0.653$ for the disk. Both motions stop at the same time. The analytic solutions for $\mathbf{F}_0$ and $\mathbf{T}_0$, respectively, and the analytically calculated universal ratio are an extension to the work of Voyenli and Eriksen [27], as they gave a numerical approximation of $\varepsilon_0$.

For $\alpha = 1$ the friction force and torque are decoupled and depend linearly on the sliding and spinning velocity, respectively. For $\alpha = 3$ the coupling is present again as an explicit calculation of friction force and torque showed. In fact, $\alpha = 1$ is the only case where net friction force and torque are decoupled. General analytic expressions for friction force and torque with positive odd $\alpha$ could be derived (App. A).

In the limits of fast spinning with slow sliding, $\varepsilon \ll 1$, and fast sliding with slow spinning, $\varepsilon \gg 1$, approximate expressions for friction force and torque could be derived. For $\varepsilon \ll 1$ the friction torque is decoupled from the (slower) sliding velocity, while for $\varepsilon \gg 1$ the friction force is decoupled from the (slower) angular velocity. For the uniform pressure distribution, the net friction force has only a component parallel to the sliding velocity.

The effect of frictional coupling on the final motion mode of a sliding and spinning disk was then investigated, i.e. if both motions stop together or if one stops earlier than the other. This can be derived from the time evolution of the velocity ratio $\varepsilon$. The zeros of an autonomous differential equation for $\varepsilon$ provide fixed points which can be stable, semi-stable or unstable. A distinction was made between trivial fixed points and finite fixed points. The trivial fixed points were $\varepsilon = 0$, corresponding to a spinning disk, and $\varepsilon = \infty$ which corresponds to a sliding disk. All other possible values were finite fixed points and denoted with $\varepsilon_0$. Stable fixed points $\varepsilon_0$ are attractive and $\varepsilon$ evolves towards such fixed points. For the disk and $\alpha = 0$ it was shown, that $\varepsilon_0 \approx 0.653$ is a stable finite fixed point. Therefore, independent of the initial velocity ratio $\varepsilon_i$ the time evolution leads $\varepsilon$ towards this $\varepsilon_0$. For $\alpha = 1$ only semi-stable fixed points exist, which mean that the initial $\varepsilon_i$ is not changed till the motion vanishes. For $\alpha = 3$ a finite fixed point exists, but this is an unstable fixed point and either $\varepsilon = 0$ or $\varepsilon = \infty$ are stable, depending on $\varepsilon_i$. For $\varepsilon_i < \varepsilon_0$ the attractive fixed point is $\varepsilon = 0$, while for $\varepsilon_i > \varepsilon_0$ it is $\varepsilon = \infty$. Only for $\varepsilon_i = \varepsilon_0$ this ratio is retained till the motion vanishes. Furthermore, it could be deduced from examples that for $\alpha < 1$ the finite fixed points are *stable*, while for $\alpha > 1$ the finite fixed points are

*unstable*. The autonomous differential equation contains a moment of inertia ratio $C = I/MR_c^2$. The value of this ratio influences the values of the finite fixed points and their existence. For certain values $C$ no finite fixed points exist and only either $\varepsilon = 0$ or $\varepsilon = \infty$ are stable fixed points. These values are different for every $\alpha$. Thus it could be shown that an interval $\mathcal{I}_\alpha$ with finite fixed points exists and that the interval limits are determined by the friction force and torque at $\varepsilon \ll 1$ and $\varepsilon \gg 1$. With the expressions for the approximated friction force and torque the limits of the interval for $\mathcal{I}_\alpha$ could be derived. The scheme, given in FIG. 3.10, shows for all possible pairs $(C, \alpha > 0)$ the stable and unstable fixed points. This scheme shows also that if a finite fixed point exists it is a *stable* one for $\alpha < 1$ and an *unstable* one for $\alpha > 1$. Thus, for $\alpha < 1$ both motions stop at the same time. This can be attributed to a negative feedback mechanism as already mentioned for $\alpha = 0$. One can now conclude, that for every $\alpha < 1$ the friction force and torque dynamically reduce each other and that a neglection of coupling would lead to an *overestimation* of friction. For $\alpha > 1$ there exist always unstable finite fixed points and no negative feedback mechanism is active. Rather, the final motion mode depends on $\varepsilon_i$ for the same reasons as already discussed for $\alpha = 3$. Disregarding the coupling means in this case an *underestimation* of friction.

For the uniform and rotationally symmetric pressure distributions the friction force component lateral to the sliding direction is nonzero for all $\alpha$ for reasons of symmetry. However, a sliding and spinning cylinder standing on one of its flat sides, provides a rotationally asymmetric pressure distribution. Due to the friction at its bottom a torque is exerted on its center of mass. Assuming that the cylinder does not topple, the torque is compensated by a pressure increase in the leading part of the contact area and a pressure decrease in the trailing part. This in turn increases the friction force in front and decreases it at the back, what results a nonzero net lateral friction force $F_\perp$. Hence, the sliding path of the cylinder is curved. For simplicity a linear pressure correction was assumed and the lateral friction force for dry Coulomb friction ($\alpha = 0$) was discussed.
The frictional induced lateral deflection of the cylinder is to the right (with respect to the sliding direction) for counterclockwise rotation and to the left for clockwise rotation of the cylinder. A theoretical and experimental investigation was made by Penner, the results of which were briefly reviewed.

The lateral deflection for a curling rock on ice is opposite to that of the cylinder. This phenomenon was taken as motivation for a closer look on the physics of curling. That friction decreases with increasing sliding velocity

is observed in experiments. Penner proposed on theoretical basis that the friction is proportional to $v_t^{-1/2}$, by considering the energy produced by the friction force and the heat conduction equation. Shegelski and Penner agree that dry friction is not the kind of friction acting between curling rock and ice. This is ruled out by the experimental observations of Shegelski et al., which underline that wet friction with a negative exponent $\alpha$ of the velocity is present. The exponent $\alpha$ takes different values depending on the type of motion of the curling rock, but lies roughly in the negative range from $-0.19$ to $-0.82$. However, the velocity dependence with negative exponent can be used only for a certain velocity range as for vanishing velocity the friction force does not diverge. Experimental data have been presented, showing the range with decreasing friction at increasing velocity.
Why the lateral deflection is in opposite direction to the cylinder with dry friction is not understood up to now. The front-back model tries to explain the correct lateral deflection direction with a larger friction force at the back of the curling rock than in front. But the origin of this asymmetry is not given. In conclusion, the curl of the curling rock stays an interesting area of research.

Shegelski et al. observed in their experiments that the curling rock shows stopping of both motions at the same time for a draw shot, while a slowly sliding and rapidly rotating curling rock shows a stopping of sliding motion before rotation stops. In the discussion of final motion modes only positive $\alpha$ were considered. Further, in case of a nonzero net lateral friction force this has to be considered in the dynamic equations of motion and thus in the autonomous differential equation for $\varepsilon$. Thus predictions of the final motion mode for the curling rock cannot be made on the basis of the investigation done here.

# Chapter 4

# The effect of contact torques on porosity of nano-powders

In the last chapter the dynamic coupling between sliding and torsion friction for a single moving object with one contact was subject of investigation. In this chapter the compaction of cohesive nano-powders is considered, which represents a system consisting of many objects (nano-particles) and possibly multiple contacts per object. The relative rotational motion between two contacting nano-particles has three degrees of freedom: two degrees of rolling, i.e. rotation about an axis parallel to the contact area plane, and one degree of rotation about the normal of the contact area plane, which will be termed torsion from here on. Hence, a friction torque can now be related to rolling and torsion as well. To distinguish the friction for the corresponding rotational degree of freedom, the friction torque for rolling is called rolling friction and for torsion it is called torsion friction. Next, a brief introduction to cohesive granular media and nano-powders is given.

## 4.1 Cohesive granular media and nano-powders

Granular media seem to be ubiquitous: large rocks, gravel, sand, powders, coffee (both as bean or milled to powder) or sugar and flour are just a few examples. A huge amount of granular media is processed yearly in industrial applications, thus it is important for industry to understand the behavior of granular systems. The field of granular media is extensively researched,

thus many articles and books exist about its application and physics. The following references give a good introduction and overview about this area [49–57].

The elements of granular systems are single particles (grains) with many internal degrees of freedom and relatively large mass. The relevant energies in granular media are much larger than thermal energies. Consider for example a particle of sand with a diameter of $100\mu$m: The kinetic energy for a typical velocity of 1 cm/s and the potential energy difference that is needed to raise it atop another particle are 9 orders of magnitude larger than the thermal energy $k_bT$ at room temperature [58]. Thus, thermal agitation can be neglected. The internal degrees of freedom tend to absorb the kinetic energy of the particles. This dissipation of kinetic energy in a granular system occurs in inelastic collisions and friction between the particles. Typical particle diameters range from several meters to some micrometers and therefore the length scale covers several orders of magnitude.

Usually the interactions between the particles in granular media can be described by compressive contact forces. For another class of granular media also tensile (cohesive) forces are present. For example in wet sand [59, 60]: the surface tension of water exerts some resistance against the separation of particles (sand grains). These interparticle capillary forces can exceed the force scale given by the particle weight by two orders of magnitude. The consequence is a significant change in the mechanical properties that makes it possible to build stable objects with wet sand, like sand castles or sand sculptures.

A similar effect can be found in fine dry powders with particle diameter less than $10\mu$m. At this length scale van der Waals forces, which are caused by dipole-dipole fluctuations [61], become dominant between adjacent particles. Such powders are referred to as cohesive powders and show different properties in comparison to regular granular media. For example, under gravity such cohesive powders do not collapse into a dense packing, but form a stable porous aggregate.

For nano-particles, where particle sizes smaller than 100nm are typical, the pore stabilization effect is enhanced. If one keeps the total mass constant and reduces the particle size, it is possible to reach porosities over 90% in a filling as can be seen in Fig. 4.1. The nano-particles take only 10% of the total volume. This effect has important consequences in nanotechnology [15, 62]. In the production of nanoceramics [63] the consolidation of nano-powders (sintering) is an important process. The so called sinter-forging technique consolidates nano-powders at low temperatures to avoid the undesired growth

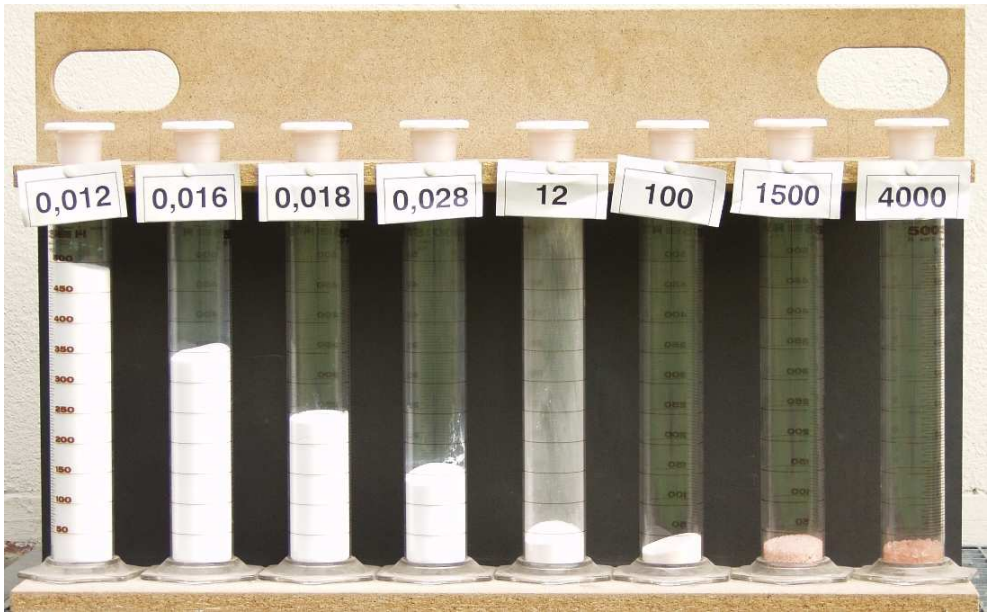


Figure 4.1: Fillings of different fine powders of the same material and with the same total mass. The labels at the cylinders show the average particle size in micrometer. The filling height corresponds to the porosity in the aggregate. The larger the filling height the larger the porosity. The porosity increases with decreasing particle size (cylinders from right to left) [15].

of particle size. In this process a highly porous nano-powder is uniaxially compacted under large pressure without constraints in lateral direction.
In contrast to nanoceramics, a highly porous aggregate is desired for gas sensors, where the high porosity provides large relative surface, which is important for a high sensitivity [64]. The dependency of this sensitivity on the particle size has been proven experimentally for $SnO_2$ [65]. The nano-particles were obtained out of the gas phase, providing a monodisperse particle size distribution [66].

Theses examples show, that nano-particles and nano-powders receive considerable attention in research and industry. About contact laws and microscopic processes, which must differ in various aspects from those of larger particles, not much is known up to now. In addition to the cohesive forces, the sinter-neck formation [62, 67] between contacting nano-particles is an important aspect, which also allows a significant mechanical torque transmission at the contact.

## 4.2 Uniaxial compaction

Under external load the behavior of granular packings is governed by particle properties (e.g. roughness, elasticity, cohesion) and also the geometrical structure of the packing plays a role (e.g. connectivity, orientations of contacts). When compacting loose granular material, density and connectivity increase until a static state is reached, where the material withstands the external pressure. Such jammed states, are currently widely studied [68–70]. For noncohesive materials the porosity in such a jammed state depends essentially on the deformability of the grains under the fixed external load. For rigid particles, the porosity could not be reduced by upscaling the external load (including gravity), but by shaking [71, 72].

For cohesive powders, static states with much higher porosity are possible. They are due to stabilization mechanisms, which involve the cohesion force as an intrinsic force scale. Therefore, these states are *not* stable for arbitrary upscaling of the external load, but only up to a threshold depending on the porosity. Exceeding this threshold leads to further compaction of the powder. In this chapter the stabilization mechanisms in nano-powders consisting of rigid nano-particles are considered in three dimensions. The previous work in two dimensions [14] is extended by introducing torsion friction in addition to rolling friction and cohesion into contact dynamics simulations (CD) of a uniaxial compression process.

The nano-particles are modeled as (perfectly) rigid spheres of identical size. Of course, two perfectly rigid spheres, if they existed, would only have a contact *point*, which could neither exert a rolling nor a torsion torque on the particles in contact. Even the (daVinci-Amontons-)Coulomb friction law (Sec. 2.1) would not be justified for such an idealized point contact. By contrast; here the rigid spheres are only considered as a geometrical idealization of real particles, and their contact areas are not taken into account explicitly: Implicitly, however, the finite size of the contacts is responsible for the various kinds of friction which are considered here in the following.

It is believed that torsion and rolling resistance are of little importance in noncohesive granular assemblies of spheres, where indeed in statics the contact-torques vanish [10] or are very weak [12], but this work was motivated rather by nano-powders. Many concepts developed for regular granular media can be applied also to nano-powders, but additional aspects have to be taken into account as well, such as strong cohesion (due to van der Waals forces) and sinter-neck formation between the particles which make the question of

blocking torsion and rolling modes relevant. Little is known so far about the way in which a sinter-neck resists rolling or torsion. It is plausible, however, that on a sufficiently short time scale (where creep can be neglected) torque thresholds have to be exceeded to break a sinter-neck and induce relative motion between the particles. Therefore, lacking well proved contact laws on the nano-scale, the simplest kind of threshold dynamics for sliding, rolling and torsion friction will be assumed here.

## 4.3 Simple contact laws for nano-particles

The relative motion of two contacting solid spheres has six degrees of freedom: Three translational degrees of freedom characterized by a velocity vector $\mathbf{v}$ with one normal component and two tangential components (sliding modes), and three rotational degrees of freedom characterized by an angular velocity vector $\mathbf{\Omega}$, again with one normal component (torsion mode) and two tangential components (rolling modes). If any of these modes are damped or blocked they represent specific dissipation or stabilization mechanisms, respectively. For instance in case of static friction a contact is stabilized against small tangential forces (blocking), while in case of sliding friction kinetic energy is dissipated (damping).

In the following section simple contact laws for the normal force, sliding, rolling and torsion friction will be described. Except of that for torsion friction, the contact laws presented here for nano-particles are the three dimensional version of the contact laws used in Ref. [15] for two dimensions. The extension with torsion friction leads then to a blocking or damping of *all* possible relative motions in three dimensions.

### 4.3.1 Cohesion and sliding friction model

Rigid spherical particles of identical sizes are considered here. But, as already mentioned above, *force* and also *torque* transmission is allowed at contacts. For cohesive powders the contact force between two particles can be repulsive, then the normal component is positive ($F_\mathrm{n} > 0$), and also attractive ($F_\mathrm{n} < 0$), depending on the other forces acting on the particles. In case of repulsion $F_\mathrm{n}$ can be arbitrarily strong if needed to ensure volume exclusion (Signorinis condition [73]). In case of attraction, however, the normal force is limited by the cohesion strength $0 > F_\mathrm{n} > -F_\mathrm{coh}$. This means that a pulling force on the

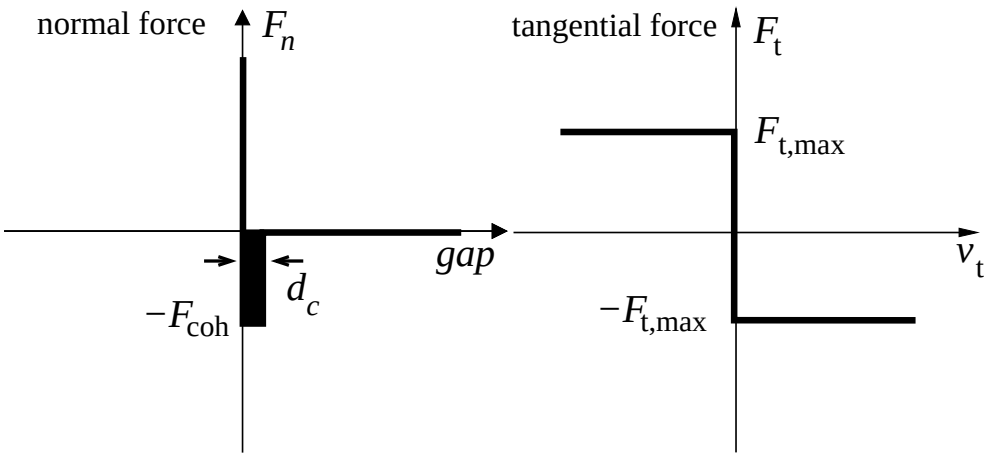


Figure 4.2: The left graph shows the model for the normal force for a cohesive contact. For a gap between two particles larger than $d_c$ the normal force is zero. At zero gap, i.e. at direct contact, the normal force $F_n$ can take any value to avoid overlapping (negative gap). If $0 \leq$ gap $\leq d_c$ then a negative (attractive) normal force $F_n$ up to the cohesion strength $F_{coh}$ is possible. The right graph represents Coulomb's law of friction: A sticking contact (with relative tangential velocity $v_t = 0$) can bear any tangential force with absolute value up to $F_{t,max}$. If sliding occurs ($v_t \neq 0$) the magnitude of the tangential force is $F_{t,max}$ while its direction is opposite to the sliding velocity. The static friction coefficient is equal to the dynamic friction coefficient, i.e $\mu_s = \mu_d$.

particles that is stronger than $F_{coh}$ can not be compensated by the contact force: the particles start moving apart, but the contact breaks only when the work done by the pulling force exceeds the cohesion energy $E_c = F_{coh} d_c$, where $d_c$ is a parameter giving the effective range of cohesion.

The cohesion force $F_{coh}$ is the same for all contacts, no matter how long they have existed. The dependence of the normal contact force $F_n$ on the distance between the particles (gap) shows the left graph in FIG. 4.2. For a gap between two particles larger than the cohesion range $d_c$ the normal force is zero. At direct contact, i.e. zero gap, $F_n$ can take any value to avoid overlapping (negative gap). The actual value of $F_n$ is determined by the external load on this contact and by the constraint condition that during the dynamics the gap remains zero. If $0 \leq$ gap $\leq d_c$ then a negative (attractive) normal force $F_n$ up to the cohesion strength $F_{coh}$ is possible, avoiding that the particles move apart. For further details about this model and other cohesion models see REF. [15].

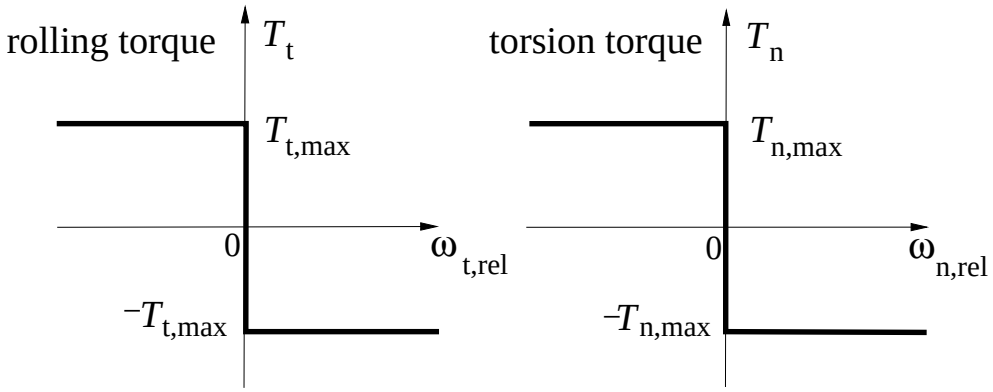


Figure 4.3: Contact torques applied to suppress rolling and torsion. The rules are similar to those of the tangential force. The rolling torque is coupled to the tangential relative angular velocity $\omega_t$ (left graph) and the torsion torque is coupled to the normal relative angular velocity $\omega_n$ (right graph).

For the tangential contact force the Coulomb friction law has been modified to include the influence of cohesion: if the relative velocity of the two particle surfaces is zero (sticking contact) the magnitude of the friction force ($F_t = |\mathbf{F}_t|$) can be any value up to the threshold $F_{t,max}$, while in the case of sliding $F_t = F_{t,max}$, and its direction is opposite to the relative velocity. The maximal friction force is proportional to the normal force including $F_{coh}$:

$$F_{t,max} = \mu(F_n + F_{coh}) \ , \tag{4.1}$$

thus the threshold value vanishes when the contact opens ($F_n = -F_{coh}$). In contrast to the original Coulomb friction law ($F_{coh} = 0$) and its illustration in the Coulomb graph in FIG. 2.5, here the maximal static friction force is identical with the dynamic friction force, or in terms of the friction coefficients it is $\mu_s = \mu_d$. The relation between relative sliding velocity and tangential friction force $F_t$ shows the right graph in FIG. 4.2.

### 4.3.2 Rolling and torsion friction model

The contact laws for the normal (torsion friction) and tangential torques (rolling friction) are chosen in analogy to the modified Coulomb friction law. Their corresponding graphs are shown in FIG. 4.3. The threshold values for the torques $T_{n,max}$ and $T_{t,max}$ are defined as force times length, where the force-scale is again given by $(F_n + F_{coh})$ and the radius of the sinter-neck $R_c$ determines the relevant length-scale (see FIG. 4.4).

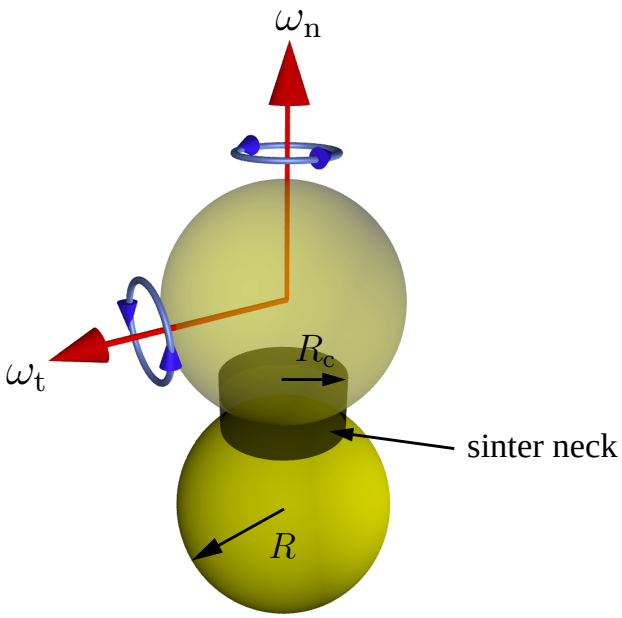


Figure 4.4: Schematic view of a sinter-neck between two nano-particles. The tangential and normal components of the relative angular velocity are displayed for rolling and torsion friction, respectively. $R$ and $R_c$ indicate the particle and sinter-neck radii $R_c$.

This length makes sense only if it is below the particle size, and in this work it is chosen within the range between zero and the effective radius at the contact: $r_{\text{eff}} = (1/R_1 + 1/R_2)^{-1}$. For two identical spheres this value is one-half of particle radius. The maximal normal and tangential torques in the model are given by:

$$T_{\text{n,max}} = \mu_{\text{n}}(F_{\text{n}} + F_{\text{coh}})r_{\text{eff}} \tag{4.2}$$
$$T_{\text{t,max}} = \mu_{\text{t}}(F_{\text{n}} + F_{\text{coh}})r_{\text{eff}} \ , \tag{4.3}$$

where the dimensionless parameters $\mu_{\text{n}}$ and $\mu_{\text{t}}$ make it possible to control the strength of blocking, similar to the friction coefficient $\mu$ in Eq. (4.1). This model is certainly oversimplified, and the physics of nano-particles might be better described by more sophisticated, yet unknown microscopically founded models. Nevertheless, with some caution one can use this simplified model to analyse the effects of rolling and torsion friction in granular media or nano-powders, respectively.

# 4.4 Computer Simulations

## 4.4.1 Introduction

Nowadays numerical simulations have become an important research tool. They are used in great variety, e.g. for testing models, measuring parameters which may be difficult to obtain by experiments or even inaccessible for them. In simulations it is easy to adjust input parameters independently. Another purpose can be to separate relevant and irrelevant properties. This makes it possible to "simplify" complex systems for a better understanding.

For granular media different simulation techniques with different range of applicability have been developed [74]. An important class of techniques are the so-called *discrete element methods* (DEM), where the trajectory of each particle is simulated. The trajectory is calculated from the interaction with other particles and the environment. Characteristic differences in the simulation methods are mainly due to different modeling of particle interactions. Prominent examples for DEM are the *event driven* (ED) method [49, 75], the *soft particle molecular dynamics* (MD) [49,76] and the *contact dynamics* (CD) method [77–79]. Each method has a different applicability.

The ED method simulates very hard particles and operates with instant binary collisions. Therefore, it works very well for systems with a low particle density, i.e. gas-like situations. However, for dense states, where clusters of contacting grains can appear, the simulation becomes critically slow, a phenomenon known as inelastic collapse [75]. Although numerical solutions exists to avoid the inelastic collaps [80], this method is not the most suitable for dense systems.

The simulation of dense granular systems is often a computational challenge, as usually the situation occurs, where dry friction and many long lasting contacts between hard particles are present. Using the soft particles molecular dynamics (MD) method, where the velocities are modeled as smooth functions of time (even for collisions), the simulation of very hard particles becomes problematic. Small time steps of the integration must be used to resolve the collisions between the particles, resulting in a slow simulation. A further difficulty in MD is encountered for dry friction, where it is not obvious how to distinguish between sliding and non-sliding contacts. The concept of the contact dynamics (CD) method overcomes the above mentioned difficulties. The CD method is discussed more detailed in the next section.

It is worth noting, that beside the DEM methods other simulation techniques are used in research of granular media, like cellular automaton modeling [81, 82] or finite element methods (FEM) [83]. A good overview on computational methods used for simulations of granular media is given in Refs. [74, 84].

### 4.4.2 The contact dynamics method

The algorithm for contact dynamics simulations has been described in the early 1980s by Lötstedt [85, 86], while its first application to granular media was done by M. Jean and J.J. Moreau [78, 79, 87] in the 1990s. CD as discrete element method provides the dynamics by integrating the equations of motion for each particle and takes, besides external fields (e.g. constant forces, gravity), the interaction between particles into account. The essential difference to MD is, that the particles are considered as perfectly rigid and the interactions are handled by means of constraint forces. For this, an implicit time step algorithm (here implicit Euler-Method [40]) is used. Thus, the contact forces are calculated by virtue of their effect, not by virtue of their cause as it is in MD. Furthermore, the infinitely steep graph of Coulomb friction and the perfect volume exclusion are implemented as a set of inequalities and no regularization is needed, as would be the case for MD.

The concept of using constraint forces leads to the following problem: The force at a contact also depends on other forces acting on the two particles, e.g. due to other adjacent contact forces. Therefore, in the presence of more than one contact per particle the force at each contact can not be calculated locally. The force calculation has to be done globally consistent at each time step. This can be done with an iterative scheme (*iterative solver*). The iterative scheme demands the most computational effort of this method, but in exchange with the implicit time stepping algorithm a relatively large time step is allowed. The resulting dynamics is non-smooth and contains sudden velocity jumps due to shocks at collisions. This is in contrast to the soft particle MD, where the velocities are modeled as smooth functions of time (even for collisions). The consequence is, that in soft particle MD a smaller time step with increasing particle stiffness is required.

The application of constraint forces and torques as well as the implicit time stepping scheme make this method particularly suitable for the implementation of threshold dynamics, i.e. also for the previously introduced contact laws, and for the proper treatment of static forces and torques in blocked or jammed states [88–92]. The CD method provides realistic dynamics for

various granular systems and is especially efficient for simulating frictional multi-contact situations of rigid particles.

More detailed descriptions of the CD algorithm can be found in [15,49,73,93–96]. These works contain the description of the basic 2D and 3D algorithm for ordinary granular materials, an analysis of the method and its application to nano-particles. Usually, CD models normal interactions with zero Newton restitution [94], but a finite Newton restitution is possible as well [97]. Even the handling of deformable bodies in CD with minor modifications has been shown [79].

### Convergence criterion and pseudo elastic behavior

The iterative solver for the contact force calculation is one the main issues in contact dynamics. To achieve perfect fulfillment of the constraints an infinite number of iterations would be needed. Thus, a criterion for stopping the iteration process is used. One can think of two different kinds of criterions: the iteration stops after a fixed number of iterations or a convergence criterion decides when to stop the iteration process. A fixed number of iterations per time step has the advantage of simplicity and makes the algorithm more transparent, providing better understanding of the method. A convergence criterion is applied inside the iteration loop and decides whether the contact force-system has reached an adequate consistent state or more iterations are needed. Thus, the number of iterations usually vary in every time step. In principle, one can distinguish between local and global convergence criteria. The local criterion checks for the relative change of the contact force, $\Delta F$, between two successive iteration steps. If at each contact $\Delta F$ is smaller than a given accuracy value the criterion is fulfilled, the iteration loop stops and the time evolution proceeds one step. The global criterion checks for the average relative change of all contact forces. For cases where the convergence of forces is slow or maybe not given, the iteration loop is stopped after a given fixed number of iterations. Usually this number is much larger, than the average number of iterations per time step needed by the convergence criterion. In [94] the local and global convergence criteria were investigated and it was found that both criteria work with similar accuracy, but differ in efficiency. However, the efficiency and choice of a criterion depends on the specific simulated system and the required accuracy level.

The finite number of iterations has a serious consequence on the global behavior of the system: it can behave quasielastically, although every contact

(or particle) is assumed to be perfectly rigid. Due to the finite number of iterations, the contact forces may not reach their ideal value to fulfill the constraints perfectly in every time step. Such errors for the normal contact force (perfect volume exclusion constraint) result in damped force oscillations and macroscopically in a quasielastic behavior [58]. To reduce this effect down to a negligible level one can use the following relation derived by Unger et al. [58, 93]:

$$N_I > \alpha(L/d)^2 \ . \tag{4.4}$$

That means, that the number of iterations $N_I$ should be larger than the proportionality constant $\alpha$ times the square of system size $L$ divided by the particle diameter $d$. The constant $\alpha$ is for homogenous (two or three dimensional) systems of order 1 [58]. If contact dynamics simulations are done with a fixed number of iterations, then $N_I$ should be the minimum number of iterations. If a convergence criterion is used, the required force accuracy parameter should be chosen such that the iteration loop is not stopped before $N_I$ iterations were done. Kadau compared in REF. [15] simulation results obtained by using a convergence criterion and by using a fixed number of iterations for a uniaxial compaction of a cohesive packing. The final porosity of the packing and the final position of the compacting piston showed no significant differences for the two criterions.

## 4.5 Simulated systems: ballistic deposits

The systems considered here consist of spherical particles of the same radius $R$. A ballistic deposit with a low density serves as a suitable initial configuration to investigate the effect of contact torques on the compactibility. Nano-particles can be extracted out of gas flow from filter processes [98,99], where they build tree-like structures similar to those of ballistic deposits [14, 100, 101]. The initial configuration of a ballistic deposit is prepared as follows: particles fall vertically towards a horizontal plane, one by one with randomly chosen $x-y$-coordinates. As soon as a falling particle comes closer to the deposit or substrate than a capture radius $r_{\text{capt}}$, the contact is established immediately, the particle sticks irreversibly. Then the next particle is dropped, until the deposit reaches the desired height. This procedure leads to building of particle chains (the tree-like structure). The process of ballistic deposition is illustrated on the left side in FIG. 4.5. The capture radius $r_{\text{capt}}$ influences the typical distance between two particle chains and

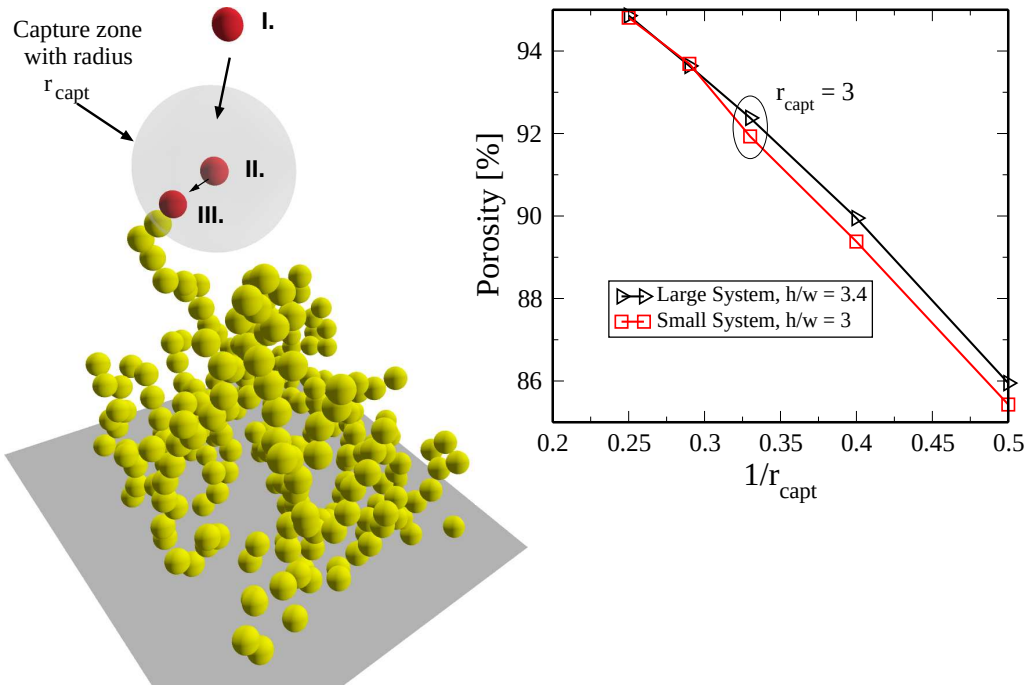


Figure 4.5: The ballistic deposition in three dimension is illustrated on the left side: I.) A particle falls vertically from a random $x-y$-position into the system. II.) On its way down, it sticks to the particle which comes first in contact with its enveloping sphere having the capture radius $r_{\text{capt}}$. III.) It is stuck on the shortest way to the particle. The graph on the right side shows the porosity in a ballistic deposit as function of the inverse capture radius.

the density of the deposit depends approximately linearly on $1/r_{\text{capt}}$ [15], i.e. with increasing capture radius the density is reduced. The graph on the right side in FIG. 4.5 shows this behavior. Due to the random character of the ballistic deposition procedure, the number of particles for systems of the same size differs slightly. Thus, for each data point in the graph the average over five different ballistic deposits was taken.

The chosen systems for the simulations were produced with $r_{\text{capt}} = 3R$, i.e. with a porosity of approximately 92%. Such a high porosity can be found in nanopowder fillings (cf. SEC. 4.1). The uniaxial compression of the ballistic deposit is simulated by a piston moving along the $z$-direction towards the bottom plane, while periodic boundary conditions in $x$- and $y$-direction are applied. Gravity is neglected and the piston compresses with a constant pressure $F/L_xL_y$. Two systems differing in size and number of particles have been simulated. The first system, referred to as "*small*" system, has a lateral

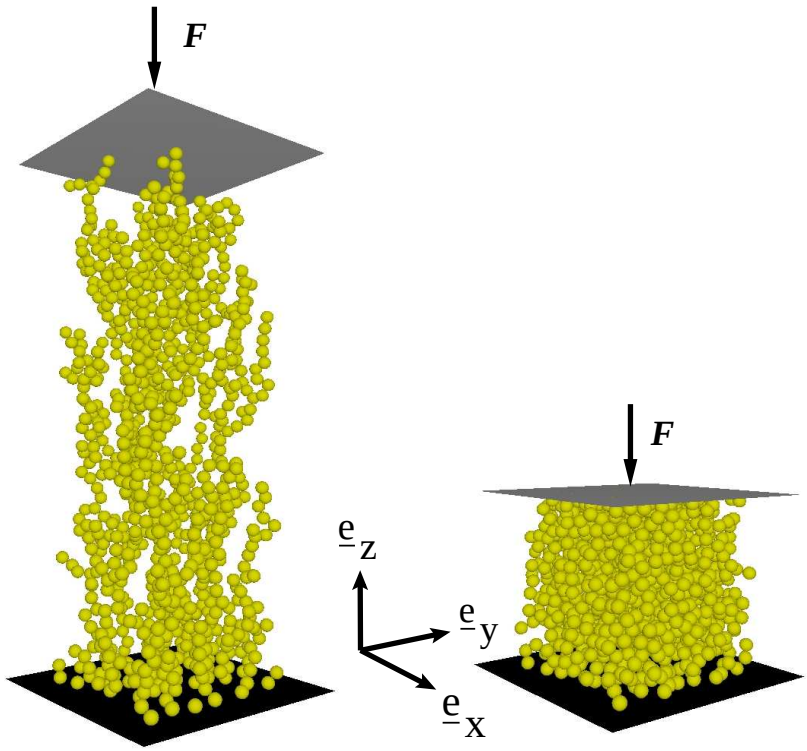


Figure 4.6: On the left side the initial arrangement with 1015 ballistically deposited particles is shown. The final (blocked) configuration of the same system compressed by the external force $F$ is shown on the right side.

size of $L_x = L_y = 20R$ and a height of $L_z = 61.5R$, whereas the second system has $L_x = L_y = 25R$ and $L_z = 87.5R$ and is referred to as "*large*" system. The small system contains 470 particles, while the large system consists of 1015 particles. For the height $L_z$ the initial piston position (at $t = 0$) was taken, where it nearly touches the highest particle. In FIG. 4.6 the ballistic deposit of the large system is shown before compaction (initial state) and compactified (final blocked state).

The simulation was stopped, when the system reached a blocked state. This was identified by checking the piston position. If it has not changed over a certain number of time steps, a blocked state was assumed. The piston has a mass of $1000\rho R^3$, where $\rho$ denotes the mass density of the particles. The pressure on the piston was set to $F_{\mathrm{coh}}/(400R^2)$ for both systems. Thus, the force value $F$ on the piston is different for the small and large system.

The typical distance between branches of the ballistic deposits is of the order of $5R$, therefore the compacting pressure is relatively weak, as the typical

load on a single branch is $F_{\mathrm{coh}}25/400 = F_{\mathrm{coh}}/16$. That is much smaller than the intrinsic force scale given by the cohesion force $F_{\mathrm{coh}}$.

## 4.6 Simulation results

The compactibility was investigated for various values of the rolling friction coefficient, $\mu_{\mathrm{t}}$, and torsion friction coefficient $\mu_{\mathrm{n}}$, while the coefficient of sliding friction, $\mu = 0.3$, was kept constant.

### 4.6.1 Final porosity

Based on the final z-position of the piston, $L_{\mathrm{z,final}}$, the porosity $E$ of the blocked states was measured:

$$E = 1 - \frac{V_{\mathrm{particles}}}{L_x L_y L_{z,\mathrm{final}}} \,, \tag{4.5}$$

i.e. the relative free-volume in the system (here $V_{\mathrm{particles}}$ denotes the total volume taken by the rigid particles). The three dimensional surface plots in FIG. 4.7 show that contact torques have significant effect on the compactification. Whereas without rolling and torsion friction the final porosity $E_0$ is about 54% for the applied weak compaction pressure, porosities as high as 82% are stable for $\mu_{\mathrm{t}} = \mu_{\mathrm{n}} = 1$. The effect on the porosity is quantitatively nearly the same for both systems. For the small system it was averaged over two simulations runs for each data point, while for the large system each data point is based on one simulation run. The small system showed relatively small fluctuations ($\approx 2\%$) in the values for the porosity. Assuming a smooth dependence of the porosity on the friction parameters, one can estimate the error bars from the figures.

The porosity added due to rolling and torsion friction,

$$E_1(\mu_{\mathrm{t}}, \mu_{\mathrm{n}}) = E - E_0, \tag{4.6}$$

saturates in the region where the coefficients $\mu_{\mathrm{t}}$ and $\mu_{\mathrm{n}}$ are larger than 0.4. More than $E_1(1,1) \approx 28\%$ cannot be achieved based on the contact torques, not even if one increases the threshold values far beyond the physically meaningful range. The maximum final porosity ($\approx 82\%$) is approximately ten percent less than the one of the initial configuration ($\approx 92\%$). Thus, the

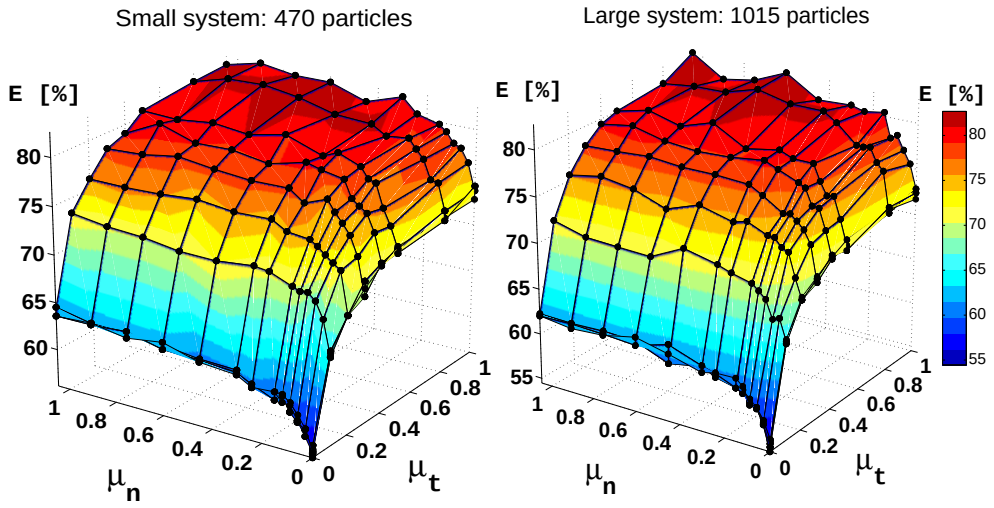


Figure 4.7: The final porosity $E$ of the compacted systems (small and large) is shown for various values of rolling ($\mu_\mathrm{t}$) and torsion resistance ($\mu_\mathrm{n}$).

suppression of rolling and torsion degrees of freedom alone does not suffice to avoid compaction completely.

Qualitatively, rolling friction alone ($\mu_\mathrm{n} = 0$) as well as torsion friction alone ($\mu_\mathrm{t} = 0$) have similar effects on the porosity. Quantitatively one finds, that $E_1(1,0) \approx 18\%$ is about twice as big as $E_1(0,1) \approx 8\%$. The reason is not clear, but it is intriguing to notice that rolling friction $\mu_\mathrm{t}$ suppresses two degrees of freedom, while $\mu_\mathrm{n}$ suppresses only one. The ratio $E_1(\tilde{\mu},0)/E_1(0,\tilde{\mu}) \approx 2$ is roughly independent of $\tilde{\mu}$.

### Additivity of porosity

An interesting property of the function $E_1(\mu_\mathrm{t},\mu_\mathrm{n})$ is, that it can be very well represented by the following sum:

$$E_1(\mu_\mathrm{t},\mu_\mathrm{n}) = E_1(\mu_\mathrm{t},0) + E_1(0,\mu_\mathrm{n}) \ . \tag{4.7}$$

This shows that rolling and torsion friction contribute independently to the porosity. The difference $|\Delta E|$ between the two sides in Eq. (4.7) is less than about 3%, and $\Delta E$ fluctuates around zero with no apparent systematics. The final porosity $E$ can then be written as:

$$E = E_0 + E_1(\mu_\mathrm{t},0) + E_1(0,\mu_\mathrm{n}) \ . \tag{4.8}$$

This property can not be extended to sliding friction. That means, the final porosity can *not* be written as the following sum:

$$E = E_0(\mu, 0, 0) + E_1(0, \mu_\mathrm{t}, 0) + E_1(0, 0, \mu_\mathrm{n}) \ . \tag{4.9}$$

The contributions from $E_1(0, \mu_\mathrm{t}, 0)$ and $E_1(0, 0, \mu_\mathrm{n})$ are nearly zero, because in the absence of sliding friction ($\mu = 0$), while the cohesion force remains unchanged, the supression of the contact torques alone, can not increase the porosity significantly. If torsion and rolling friction are present and sliding friction is not, the particles easily slide relatively to each other and the system can be compactified to a low porosity state. Thus, the final porosity $E$ achieved for the triple $(\mu, \mu_\mathrm{t}, \mu_\mathrm{n})$ is not a simple sum of independent porosity contributions.

### 4.6.2 Mechanical stress

How the static response of the large system to the external load differs with and without contact torques shall be discussed here. For this the macroscopic stress tensor was measured, which can be defined as followed [102]:

$$\sigma_{ij} = -\frac{1}{V}\sum_{c^{(+)}} F_i^c \, l_j^c - \frac{1}{V}\sum_{c^{(-)}} F_i^c \, l_j^c = \sigma_{ij}^+ + \sigma_{ij}^- \, , \tag{4.10}$$

where only the contacts under compression ($\sigma_{ij}^+$) or the ones under tension ($\sigma_{ij}^-$) were taken separately into account. Here $l_j^c$ is the $j$th component of the interstice vector connecting the centers of the particles at contact $c$.

The $zz$-components of the stress tensor are shown in Tab. (4.1), where the resulting stress $\sigma_{zz} = F/L_x L_y$ is of course determined by the pressure on the piston, which is the same for all cases and is taken as unit stress. In the zero-torque case more than twice of the external pressure is provided by the contacts under compression, because a sufficient amount of tension must be allowed in the system in order to stabilize the pores. This internal counter-stress is diminished significantly by rolling friction, whereas torsion friction alone has little effect on the partial stresses $\sigma_{zz}^+$ and $\sigma_{zz}^-$.

In the absence of contact torques, strong tensile contact forces appear and seem to be crucial for stabilizing the compressive force lines against buckling in the porous system. This pore stabilization mechanism has also been found in two-dimensional systems [14]. Of course, the contribution of the compressive forces to the macroscopic stress tensor overcompensates the one of the

| $\mu_t$ | $\mu_n$ | $\sigma_{zz}$ | $\sigma_{zz}^+$ | $\sigma_{zz}^-$ |
|---|---|---|---|---|
| 0.0 | 0.0 | 1.0 | 2.2 | -1.2 |
| 0.1 | 0.1 | 1.0 | 1.4 | -0.4 |
| 0.3 | 0.3 | 1.0 | 1.1 | -0.1 |
| 1.0 | 1.0 | 1.0 | 1.1 | -0.1 |
| 0.0 | 0.3 | 1.0 | 2.2 | -1.2 |
| 0.0 | 1.0 | 1.0 | 1.9 | -0.9 |
| 0.3 | 0.0 | 1.0 | 1.2 | -0.2 |
| 1.0 | 0.0 | 1.0 | 1.4 | -0.4 |

Table 4.1: The influence of the normal and tangential contact torques on the stress transmission along the direction of the uniaxial compression is shown. $\sigma_{zz}^+$ and $\sigma_{zz}^-$ are containing only contributions of the compressive and the tensile contacts, respectively.

tensile forces in order to balance the external load (see TAB. 4.1). In the case where contact torques are allowed, rolling and torsion friction already stabilize the force lines against buckling, before significant tensile forces develop. This does not mean that cohesion is superfluous in this case as it is also responsible for the enhanced threshold values of the contact torques (EQ. (4.2)).

## 4.7 Summary

Three dimensional contact dynamics simulations of cohesive powders were studied, where the porosity under weak uniaxial compression was of main interest. It was focused on the effect of contact torques which suppress relative *torsion* and *rolling* of the adjacent particles. Furthermore, it was found that the presence of contact torques has enormous impact on reducing the final density of the system.

A remarkable feature is the additivity found in the porosity, i.e. the porosity is well represented as the sum of independent contributions of the torsion and rolling friction. But it is not valid to extend this with sliding friction, i.e. extend the function for the porosity with $\mu$. Thus, it seems that the property of independent free volume additivity is a property of the pair $(\mu_t, \mu_n)$ alone and not extendable with or transferable to other relative motion modes.

In addition the characteristics of the stress transmission is altered: Without torsion and rolling friction strong tensile forces develop and play important

role in the mechanical stabilization. These tensile contacts, however, cancel a large part (more than half) of the pressure exerted by compressive forces and only the remaining part is utilized to resolve the external load. This situation is changed by switching on contact torques, which reduce tensile forces significantly in the system. In that case the stress due to the compressive contacts corresponds approximately to the external load and only a small part of this stress is "wasted" to overcompensate tensile forces.

Additionally, an even *larger* system with 4193 particles has been simulated for the parameter range $\mu_\mathrm{t} = \mu_\mathrm{n} = 0..1$ and $\mu = 0.3$. The compacting pressure was chosen to that of the small and large system. The aspect ratio was $h/w = 3.5$ and the initial porosity of 92.3% was similar to that of the other two systems. The final porosity ranges from $\approx 54\%$ to $\approx 82\%$, i.e. the same range as shown in figure FIG. 4.7. Finally, one can conclude, that the obtained results are independent of the system size and slightly different aspect ratios.

The CompactDisc enclosed to this work includes movies, which show the uniaxial compaction of the ballistic deposit for four different combinations of $\mu_n$ and $\mu_t$. The contents of this CompactDisc is described in APP. B.

# Chapter 5

# Conclusions and Outlook

## 5.1 Coupling of dynamic friction force and torque

The dynamic coupling between sliding friction and torsion friction with a power-law velocity dependent friction law was subject of Chap. 3. The most intriguing result was, that for positive exponents $\alpha < 1$ the dynamical coupling leads to a decrease of friction force and torque, while for $\alpha > 1$ it leads to an increase of both. This has direct consequences on the dynamics of a sliding and rotating disk, particularly on its final motion modes. If $\alpha < 1$ both motions stop together independent of the initial velocities. On the other hand, if $\alpha > 1$, one of the motions will become dominant and only for a specific initial velocity ratio both motions vanish together. For $\alpha = 1$ the friction force and torque are decoupled and this case provides no special dynamical behaviour.

It could be shown, that the disregard of coupling would lead to an overestimation of friction in case of $\alpha < 1$ and to an underestimation of friction for $\alpha > 1$. In Ref. [12] an estimation for dry powders settling and chute flow shows that in case of Coulomb friction ($\alpha = 0$) friction would be overestimated by as much as $30\% - 50\%$, assuming that for faceted particles the velocity ratio is $\varepsilon \approx 1$ .

The investigation of final motion modes is an interesting task. In the inverse sliding problem [30, 31] the knowledge on final motion modes finds a practical application. The analysis of the final motion modes for a non-uniform

pressure distribution at the contact area, where the net lateral friction force then is nonzero and has to be taken into account, is an interesting (future) extension.

A preliminary analysis of friction force and torque for radially outward increasing and decreasing pressure distribution showed in case of $\alpha = 0$, that the friction force remains unaltered, while the value of the friction torque at $\varepsilon = 0$ increases and decreases, respectively. At $\varepsilon = \infty$ the friction torque is not changed. Compared to the uniform pressure distribution the curves are qualitatively the same. For $\alpha > 0$ a more detailed analysis is currently under investigation.

The presented review of research on ice curling can be taken as an inspiration to do an analysis for a velocity dependence with negative $\alpha$. As first step and for the sake of simplicity this can be done for the uniform pressure distribution and then for a non-uniform pressure distribution. It is expected that this contributes to the understanding of the dynamics (final motion modes) of the curling rock on ice.

## 5.2 Contact torques in nanopowders

The effect of contact torques on the final porosity of uniaxially compacted nano-powders was discussed in Chap. 4. There it was found that rolling (tangential friction torque) and torsion friction (normal friction torque) contribute independently to the final porosity so that the final porosity can be expressed as a sum of all contributions. Further, it was found that the presence of rolling and torsion friction significantly reduces tensile forces in the (final) system.

The phenomenological model for torsion friction, and also for sliding and rolling friction can be regarded as a first approach of contact laws for contacts between nano-particles. Atomistically founded contact laws are not available up to now. Further, it is unclear how friction force and friction torque are coupled (in both cases of static and dynamic friction) for contacts on the atomic scale, which was one of the reasons why frictional coupling of sliding and torsion was not considered in that chapter.

Another reason was that the implementation of frictional coupling into the contact dynamics method (CD) would not be a simple task. At first sight the strategy how to handle the coupling within the concept of CD has to

be clarified and if the CD method remains stable and reliable with such an extension, not to mention the required significantly larger (computational) effort [103]. For fixed rolling friction coefficient $\mu_t$ and torsion friction coefficients $\mu_n$ the final porosity depends on the ratio of compacting pressure and cohesion strength [15, 104, 105]. Here $\mu_t$ and $\mu_n$ were varied for one value of this ratio. Thus, it would be interesting to do the same analysis for different pressure-cohesion ratios.

The implemented friction law for rolling friction in the contact dynamics code is technically restricted to a contact between particles of nearly equal size (for an explanation of this see [15]), thus the simulations were done for monodisperse systems. For the other friction laws (sliding, torsion, normal force) such a technical restriction does not exist, so that an extension of rolling friction to contacts between particles of (arbitrary) different size would give the possibility to investigate the influence of polydispersity on the final porosity and particularly the role of contact torques. It would be interesting to know, for example, if the additivity of porosity is retained.
It is worth noting, that recently advances were made to allow rolling friction for contacts between particles of different size in 2D contact dynamics simulations. If this extension is also possible for 3D contact dynamics simulations is not clarified up to now [106].

## 5.3 A further perspective: torsion friction on the atomic scale

An experimental tool exists which allows to detect (frictional) forces on the atomic scale: The Atomic Force Microscopy (AFM), which was introduced in 1986 [8]. AFM allows to detect sub-nanonewton frictional forces acting between a sample surface and a sharp tip, which is mounted on a soft leaf spring, the so-called cantilever. Usually the tip moves relative to the substrate and typically has a size of 10 to 100 nm [9]. With AFM many experimental results about atomic-scale friction have been obtained: in 1987 Mate et al. used a tungsten tip on graphite and observed two important effects [107]: a saw-tooth pattern of lateral forces (stick-slip) and hysteresis between forward and backward scans (friction loop). A rather linear dependence of friction on normal force with friction coefficient $\mu = 0.01$ was also found. After this pioneering work, friction on the atomic scale was observed several times under different conditions. The velocity dependence of friction on the atomic scale was studied by Gnecco et al. on NaCl [108]. They found

that atomic friction increases logarithmically with the sliding velocity. A logarithmic dependence on velocity and an atomic-scale stick-slip process was also reported by Bennewitz et al. on Cu(111) [1] [110].

Inspired by the experimental setup of the AFM many atomistic computer simulations were done modeling such a tip-sample (substrate) system. This atomic-scale sliding friction has been studied by molecular dynamics (MD) simulations by several authors: Landman et al. found atomic-scale stick and slip behaviour when shearing a silicon tip on a silicon (111) surface and a $CaF_2$ tip on a $CaF_2$ substrate [111, 112]. Stick and slip was also observed by Niemien et al. for a copper tip on a copper (100) surface [113], and by Sørensen et al. for a flat copper tip (111) on a copper surface (111) [114]. Ref. [115] gives a good review on experimental and theoretical results of friction on the nanometer scale.

Most theoretical works and simulations consider the shearing and sliding of the tip in translational direction. A rotation of the tip in normal direction to the substrate (torsion) was not considered up to now. Experimentally this is problematic as normally the cantilever used in atomic force microscopy can only detect normal and lateral forces. Thus a comparison between theoretical and experimental results of torsional rotation is not possible. But the investigation of this torsional movement of the tip is interesting at least for the following reasons: a contact law for torsion friction based on atomistic investigations is missing. Such a contact law would be interesting for example for the contact dynamics simulations (Chap. 4) of nano-particles, where a phenomenological contact law has to be used. Furthermore, the effect of load, commensurability and other properties on the sliding friction force were widely investigated, but such investigations for torsion friction are missing.

This is taken as motivation for this theoretical investigation of atomic-scale torsion friction. A tip in contact with a flat substrate surface is simulated using the molecular dynamics (MD) method. A molecular dynamics simulation code has been written, the features of which will now be described briefly. A more detailed description of these features can be found in Refs. [116, 117].

For the interactions between the atoms the Lennard-Jones (pair-)potential is used here:

$$U(r_{ij}) = 4\epsilon \left[ \left( \frac{\sigma}{r_{ij}} \right)^{12} - \left( \frac{\sigma}{r_{ij}} \right)^{6} \right]$$

[1] The numbers in (111) represent the Miller indices h,k and l: (hkl) [109].

Here $r_{ij}$ denotes the distance between two atoms. For large inter-atomic distances the term proportional to $1/r_{ij}^6$ in $U(r_{ij})$ dominates and constitutes the attractive part due to van der Waals dispersion forces. These are rather weak interactions, which however dominate the bonding character of closed-shell systems. At short distances the term proportional to $1/r_{ij}^{12}$ is dominant, which models the repulsion between atoms when they are brought very close to each other. Its physical origin is related to the Pauli principle: When the electronic clouds surrounding the atoms start to overlap, the energy of the system increases sharply [116]. The parameter $\epsilon$ denotes the minimum potential energy at the equilibrium distance $d = 2^{1/6}\sigma$, while $\sigma$ defines the characteristic range of interaction. The Lennard-Jones potential models the interactions between noble gas atoms very well, but it fails to describe properly the interactions of e.g. metals, which is always a problem of pair-potentials [118]. The units of the physical quantities are measured in $m$, $\epsilon$ and $\sigma$ and corresponding combinations of these. For example forces are measured in units of $\epsilon/\sigma$ and time in $\sigma\sqrt{m/\epsilon}$. For typical values of $m$, $\epsilon$ and $\sigma$ [116] the order of magnitude for forces is nanonewton (nN) and for time is picoseconds (ps).

Usually molecular dynamic (MD) simulations are classical simulations, meaning that the time evolution of atoms are described by using Newton's equation of motion. The corresponding differential equations of second order are discretized with respect to the time and as finite difference method the *leap-frog* algorithm was implemented. Periodic boundary conditions with a cubic unit cell in all directions $(x, y, z)$ can be applied, while the *minimum image convention* is considered. For the atomic interactions only atomic pairs are taken into account which are closer than a cut-off distance $r_C$, the so-called *cut-off radius*. With the use of the *linked cell* method the computational effort for the pair search for the interaction force calculation scales proportional with the number of atoms $N$, instead of scaling proportional with $N^2$ [116]. To maintain a constant temperature of the system or for a certain group of atoms two temperature coupling methods have been implemented: The Nosé-Hoover thermostat [117–119] and Langevin dynamics [9].

The simulated system is shown in FIG. 5.1, where a sphere represents an atom. The asperity and substrate consist of the closest-packed atomic layers of the face centered cubic (fcc) crystal structure, i.e. the (111) layers of a fcc crystal. The two red colored layers at the top of the tip are only fixed in $z$ direction, while the two black colored layers at the bottom of the substrate are fixed completely. The two red colored layers will be subject to external forces. The two green layers in tip and substrate can be coupled to a heat bath either

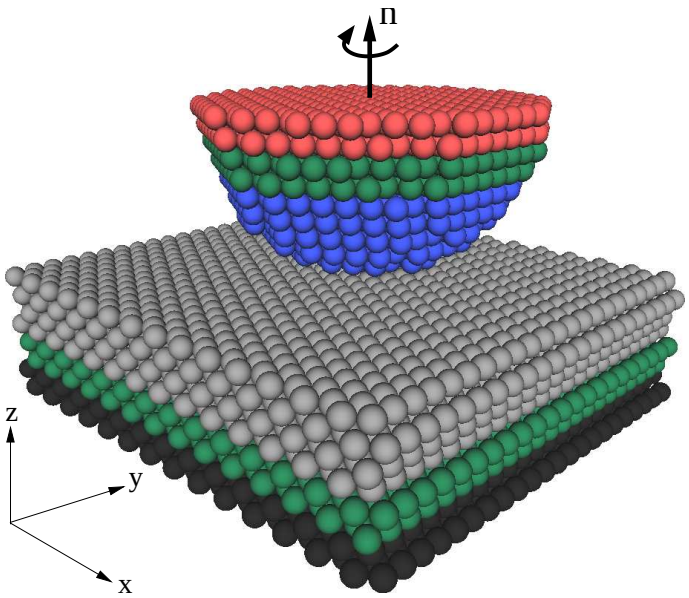


Figure 5.1: The simulated system: the asperity and substrate consists of (111) fcc-layers stacked upon each other. The red colored atoms were fixed in $z$ direction and the black colored atoms were fixed in all directions. The green colored atoms are coupled to a heat bath, while the blue and gray atoms were free of constraints. The rotation axis $\mathbf{n}$ is indicated, around which the red colored layers rotate.

with the Nosé-Hoover thermostat or Langevin dynamics. This mimics the flow of heat into the surrounding material of the experimental setup, which is not explicitly simulated. Furthermore, the heating and possibly melting of the system due to applied external forces is avoided. For the blue and gray colored atoms no constraints are given. In $x-$ and $y-$direction periodic boundary conditions [117] are applied and the total number of atoms is 6330.

The simulated system was equilibrated to the temperature of $T = 0.1\ \epsilon/k_B$ using the Nosé-Hoover thermostat. After that, an external force of strength $\lambda$ was applied on each red colored atom in such a way that the angular acceleration was the same for all red colored atoms. With an additional damping force a smooth (angular) acceleration of the red top layers is provided and torsional oscillations are suppressed. The first results of the simulations for different values of $\lambda$ are shown in FIG. 5.2. The graph shows the time evolution of the torsion angle $\Delta\varphi$, i.e. the angle the red colored atoms were rotated from their initial position. After time $t = 200$ the external force was switched off and the two red colored top layers could relax. It can be recognized that for the external force $\lambda = 0.017$ the two top layers were rotated

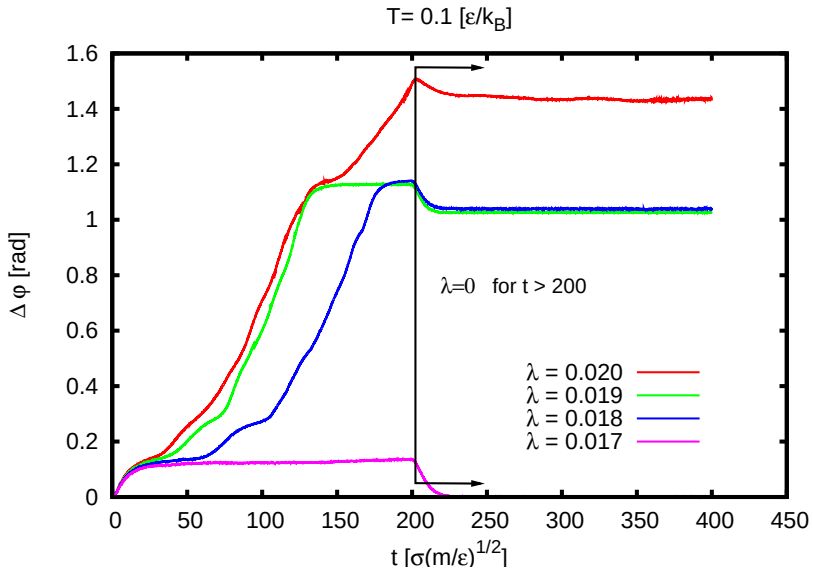


Figure 5.2: The time evolution of the torsion angle for different force strengths $\lambda$. After time $t = 200$ the force strength was set to zero, $\lambda = 0$.

reversibly as the torsion angle $\Delta\varphi$ returns to zero after this external force was switched off ($t > 200$). This is not the case for forces with $\lambda \geq 0.018$. The two red colored top layers rotate much farther and after switching off the external force they rotate back a little bit, but do not turn back to their initial position. Thus the rotation of the two top layers was irreversible.

The plateaus in the graph indicate that the tip locks in at certain torsion angles. Which layers are responsible for this and what mechanism causes this behaviour is the task for further analysis. A visual impression of the rotation dynamics can be obtained from movies of these simulations. Two movies for $\lambda = 0.017$ and $\lambda = 0.02$ are included on the attached CompactDisc (for its contents see App. B), which show the case of reversible and irreversible torsional rotation of the two red colored top layers. To follow the dynamics of the rotation more easily for each of the three different groups of tip-layers an atom was chosen and colored yellow.

The research on atomic-scale torsion friction is in progress and the investigation of the effect of load and different temperatures on torsion friction is a future task. With the written molecular dynamics code it is at the moment only possible to simulate one sort of atoms. Thus the interaction between tip and substrate is the same as within tip or substrate. An extension to include different sorts of atoms is another future task. Then it is possible to simulate

tip and substrate made of "different materials". Furthermore it is worth to consider a change of the interaction potential from the Lennard-Jones pair-potential to a potential which allows to simulate the materials used in AFM more realistically.

# Appendix A

# Derivation of friction force and torque for odd $\alpha$

In this appendix the friction force and torque for odd exponents $\alpha > 0$ are calculated explicitley.

The local friction force $d\mathbf{f}_\alpha$ used in SEC. 3.2.1 was:

$$d\mathbf{f}_\alpha = -\gamma^\alpha \frac{F_\mathrm{n}}{\pi}(\omega_\mathrm{n} R_\mathrm{c})^\alpha |\varepsilon \mathbf{e}_v + \tilde{r}\mathbf{e}_\varphi|^{\alpha-1}(\varepsilon \mathbf{e}_v + \tilde{r}\mathbf{e}_\varphi)\ \tilde{r}d\tilde{r}d\varphi. \tag{A.1}$$

With restricting the real exponent $\alpha$ to odd values, one can make the following substitution $\alpha = 2n+1$ in $d\mathbf{f}_\alpha$ and then it is:

$$\begin{aligned} d\mathbf{f}_{2n+1} &= -\gamma_{2n+1}\frac{F_\mathrm{n}}{\pi}(\omega_\mathrm{n} R_\mathrm{c})^{2n+1}|\varepsilon \mathbf{e}_v + \tilde{r}\mathbf{e}_\varphi|^{2n}(\varepsilon \mathbf{e}_v + \tilde{r}\mathbf{e}_\varphi)\ \tilde{r}d\tilde{r}d\varphi \\ &= -\gamma_{2n+1}\frac{F_\mathrm{n}}{\pi}(\omega_\mathrm{n} R_\mathrm{c})^{2n+1}\underbrace{(\varepsilon \mathbf{e}_v + \tilde{r}\mathbf{e}_\varphi)^{2n+1}}_{\tilde{\mathbf{v}}^{2n+1}}\tilde{r}d\tilde{r}d\varphi \end{aligned} \tag{A.2}$$

The expansion of the above defined dimensionless velocity $\tilde{\mathbf{v}}^{2n+1}$ gives:

$$\begin{aligned} \tilde{\mathbf{v}}^{2n+1} &= (\tilde{\mathbf{v}}^2)^n\tilde{\mathbf{v}} \\ &= ((\varepsilon \mathbf{e}_v + \tilde{r}\mathbf{e}_\varphi)^2)^n\tilde{\mathbf{v}} \\ &= (\underbrace{\varepsilon^2}_{a} + \underbrace{\tilde{r}^2 - 2\varepsilon\tilde{r}\sin\varphi}_{b})^n\tilde{\mathbf{v}} \end{aligned} \tag{A.3}$$

With the two scalars $a$ and $b$ one can use the binomial relation for $(a+b)^n$ [37]:

$$(a+b)^n = \sum_{k=0}^{n}\frac{n!}{(n-k)!k!}a^{n-k}b^k$$

The binomial relation used twice gives:

$$\begin{aligned}\tilde{\mathbf{v}}^{2n+1} = (\tilde{\mathbf{v}}^2)^n\tilde{\mathbf{v}} &= \sum_{k=0}^{n}\frac{n!}{(n-k)!k!}(\varepsilon^2)^{n-k}(\underbrace{\tilde{r}^2}_{a'}+\underbrace{(-2\varepsilon\tilde{r}\sin\varphi)}_{b'})^k\tilde{\mathbf{v}} \\ &= \sum_{k=0}^{n}\frac{n!}{(n-k)!k!}(\varepsilon^2)^{n-k} \qquad (A.4) \\ &\quad\cdot\sum_{l=0}^{k}\frac{k!}{(k-l)!l!}(\tilde{r}^2)^{k-l}(-2\varepsilon\tilde{r}\sin\varphi)^l\begin{pmatrix}\varepsilon-\tilde{r}\sin\varphi\\ \tilde{r}\cos\varphi\\ 0\end{pmatrix}\end{aligned}$$

This expression for $\tilde{\mathbf{v}}^{2n+1}$ is inserted in Eq. (A.2).
The first component of the net sliding friction force $\mathbf{F}_{2n+1}$ gives then:

$$\begin{aligned}\mathbf{F}_{2n+1}\cdot\mathbf{e}_v &= -\gamma_{2n+1}\frac{F_\mathrm{n}}{\pi}(\omega_\mathrm{n}R_\mathrm{c})^{2n+1}\int_0^1\int_0^{2\pi}\tilde{\mathbf{v}}^{2n+1}\tilde{r}d\tilde{r}d\varphi \\ &= -\gamma_{2n+1}\frac{F_\mathrm{n}}{\pi}(\omega_\mathrm{n}R_\mathrm{c})^{2n+1}n!\int_0^1\int_0^{2\pi}\sum_{k=0}^{n}\frac{(\varepsilon^2)^{n-k}}{(n-k)!}\sum_{l=0}^{k}\frac{(-2)^l(\tilde{r}^2)^{k-l}}{(k-l)!l!} \\ &\quad\cdot\left(\varepsilon^{(l+1)}\tilde{r}^l\sin^l\varphi-\varepsilon^l\tilde{r}^{(l+1)}\sin^{l+1}\varphi\right)\tilde{r}d\tilde{r}d\varphi\ .\end{aligned}$$

It is allowed here to permutate integration and sum, so that the integration over $\tilde{r}$ results in:

$$\begin{aligned}\mathbf{F}_{2n+1}\cdot\mathbf{e}_v &= -\gamma_{2n+1}\frac{F_\mathrm{n}}{\pi}(\omega_\mathrm{n}R_\mathrm{c})^{2n+1}n!\sum_{k=0}^{n}\frac{(\varepsilon^2)^{n-k}}{(n-k)!}\sum_{l=0}^{k}\frac{(-2)^l\varepsilon^l}{(k-l)!l!} \qquad (A.5) \\ &\quad\left(\frac{\varepsilon}{2k-l+2}\int_0^{2\pi}\sin^l\varphi d\varphi-\frac{1}{2k-l+3}\int_0^{2\pi}\sin^{l+1}\varphi d\varphi\right)\end{aligned}$$

The integration over $\varphi$ affects only the two terms in paranthesis. The integrands contain the sin function with the exponent $l$ and $l+1$, respectively. It depends now on the exponent if a term vanishes over integration or gives a finite value. For an odd exponent the term is zero after integration, while for an even exponent the integration gives the finite value $\pi$. Finally, the two terms contribute in alternating order with their coefficients at the integrals to the double sum.

Finall, the first component of the sliding friction force $\mathbf{F}_n$ is:

$$\mathbf{F}_{2n+1}\cdot\mathbf{e}_v = -\gamma_{2n+1}F_\mathrm{n}(\omega_\mathrm{n}R_\mathrm{c})^{2n+1}\mathcal{F}_{\mathrm{v},2n+1}(\varepsilon) \qquad (A.6)$$

with $\mathcal{F}_{\mathrm{v},2n+1}(\varepsilon)$ defined as:

$$\mathcal{F}_{\mathrm{v},2n+1}(\varepsilon) = n! \sum_{k=0}^{n} \frac{(\varepsilon^2)^{n-k}}{(n-k)!} \cdot \tag{A.7}$$

$$\sum_{l=0}^{k} \frac{(-2)^l \varepsilon^l}{(k-l)!l!} \cdot \begin{cases} \dfrac{2\varepsilon}{2k-l+2} = \dfrac{\varepsilon}{k+1} \ , & l = 0 \\ \dfrac{2\varepsilon}{2k-l+2} \dfrac{1 \cdot 3 \cdot 5, \ldots, (l-1)}{2 \cdot 4 \cdot 6 \cdot 8, \ldots, l} \ , & l \text{ even} \\ \dfrac{-2}{2k-l+3} \dfrac{1 \cdot 3 \cdot 5, \ldots, l}{2 \cdot 4 \cdot 6 \cdot 8, \ldots, (l+1)} \ , & l \text{ odd} \end{cases}$$

The second component for the sliding friction force (the $\mathbf{e}_\perp$ component) looks written explicitley:

$$\begin{aligned} \mathbf{F}_{2n+1} \cdot \mathbf{e}_\perp &= -\gamma_{2n+1} \frac{F_\mathrm{n}}{\pi} (\omega_\mathrm{n} R_\mathrm{c})^{2n+1} \int_0^1 \int_0^{2\pi} \tilde{\mathbf{v}}^{2n+1} \tilde{r} d\tilde{r} d\varphi \\ &= -\gamma_{2n+1} \frac{F_\mathrm{n}}{\pi} (\omega_\mathrm{n} R_\mathrm{c})^{2n+1} n! \int_0^1 \int_0^{2\pi} \sum_{k=0}^{n} \frac{(\varepsilon^2)^{n-k}}{(n-k)!} \sum_{l=0}^{k} \frac{(-2)^l (\tilde{r}^2)^{k-l}}{(k-l)!l!} \\ &\quad \cdot \left( \varepsilon^l \tilde{r}^{(l+1)} \sin^l \varphi \cos \varphi \right) \tilde{r} d\tilde{r} d\varphi \ . \end{aligned}$$

If one takes only the the integration over $\varphi$ into account, one can recognize that:

$$\begin{aligned} \int_0^{2\pi} \sin^l \varphi \cos \varphi d\varphi &= \frac{1}{l+1} \int_0^{2\pi} \frac{d}{d\varphi} \sin^{l+1} \varphi d\varphi \\ &= \frac{1}{l+1} \sin^{l+1} \varphi \Big|_0^{2\pi} = 0 \ , \ \forall \ l > 0 \end{aligned}$$

That means, that the integration over $\varphi$ results in a completely vanishing component $\mathbf{F}_{2n+1} \cdot \mathbf{e}_\perp$. Thus, the net lateral sliding friction force is zero for all values of $n$. With numerical calculations it can be shown, that this is also valid for every real exponent $\alpha$. This is due to the symmetry of the pressure distribution as it was discussed in Sec. 3.5

For the net friction torque the following integral has to be calculated:

$$\begin{aligned}
\mathbf{T}_{2n+1} &= R_\mathrm{c} \int_0^1 \int_0^{2\pi} \tilde{\mathbf{r}} \times d\mathbf{f}_{2n+1} \\
&= -\gamma_{2n+1} \frac{F_\mathrm{n} R_\mathrm{c}}{\pi} (\omega_\mathrm{n} R_\mathrm{c})^{2n+1} \int_0^1 \int_0^{2\pi} (\tilde{\mathbf{r}} \times \tilde{\mathbf{v}})(\tilde{\mathbf{v}}^2)^n \tilde{r} d\tilde{r} d\varphi \\
&= -\gamma_{2n+1} \frac{F_\mathrm{n} R_\mathrm{c}}{\pi} (\omega_\mathrm{n} R_\mathrm{c})^{2n+1} \int_0^1 \int_0^{2\pi} (\tilde{\mathbf{v}}^2)^n (\tilde{r}\mathbf{e}_r \times (\varepsilon \mathbf{e}_v + \tilde{r}\mathbf{e}_\varphi)) \tilde{r} d\tilde{r} d\varphi
\end{aligned}$$

With the two properties of the cross product between the unit vectors

$$\begin{aligned}
\mathbf{e}_r \times \mathbf{e}_v &= (-\sin\varphi)\mathbf{e}_\omega \ , \\
\mathbf{e}_r \times \mathbf{e}_\varphi &= \mathbf{e}_\omega
\end{aligned}$$

only the $\mathbf{e}_\omega$ component remains for the friction torque and one can write:

$$\mathbf{T}_{2n+1} \cdot \mathbf{e}_\omega = -\gamma_{2n+1} \frac{F_\mathrm{n} R_\mathrm{c}}{\pi} (\omega_\mathrm{n} R_\mathrm{c})^{2n+1} \int_0^1 \int_0^{2\pi} (\tilde{\mathbf{v}}^2)^n \left[\tilde{r}^2 - \varepsilon \tilde{r} \sin\varphi\right] \tilde{r} d\tilde{r} d\varphi$$

For $(\tilde{\mathbf{v}}^2)^n$ its double sum representation (Eq. (A.4)) is used and after integration over $\tilde{r}$ one ends up with an expression for $\mathbf{T}_{2n+1}$ that is similar to that of the first component of sliding friction force:

$$\begin{aligned}
\mathbf{T}_{2n+1} \cdot \mathbf{e}_\omega = -\gamma_{2n+1} \frac{F_\mathrm{n} R_\mathrm{c}}{\pi} (\omega_\mathrm{n} R_\mathrm{c})^{2n+1} n! \sum_{k=0}^{n} \frac{(\varepsilon^2)^{n-k}}{(n-k)!} \sum_{l=0}^{k} \frac{(-2)^l \varepsilon^l}{(k-l)! l!} \\
\left( \frac{1}{2k-l+4} \int_0^{2\pi} \sin^l \varphi d\varphi - \frac{\varepsilon}{2k-l+3} \int_0^{2\pi} \sin^{l+1} \varphi d\varphi \right)
\end{aligned}$$

Therefore, for the same reasons as discussed for the sliding friction force one can write directly:

$$\mathbf{T}_{2n+1} \cdot \mathbf{e}_\omega = -\gamma_{2n+1} F_\mathrm{n} R_\mathrm{c} (\omega_\mathrm{n} R_\mathrm{c})^{2n+1} \mathcal{T}_{\mathrm{n},n}(\varepsilon) \tag{A.8}$$

with $\mathcal{T}_{\mathrm{n},2n+1}(\varepsilon)$ defined by:

$$\mathcal{T}_{\mathrm{n},2n+1}(\varepsilon) = n! \sum_{k=0}^{n} \frac{(\varepsilon^2)^{n-k}}{(n-k)!} \cdot \tag{A.9}$$

$$\sum_{l=0}^{k} \frac{(-2)^l \varepsilon^l}{(k-l)!l!} \cdot \begin{cases} \dfrac{2}{2k-l+4} = \dfrac{1}{k+2}\,, & l = 0 \\ \dfrac{2}{2k-l+4} \dfrac{1 \cdot 3 \cdot 5, \ldots, (l-1)}{2 \cdot 4 \cdot 6 \cdot 8, \ldots, l}, & l \text{ even} \\ \dfrac{(-\varepsilon)}{2k-l+3} \dfrac{1 \cdot 3 \cdot 5, \ldots, l}{2 \cdot 4 \cdot 6 \cdot 8, \ldots, (l+1)}\,, & l \text{ odd} \end{cases}$$

If one sets $n = 0$ ($\alpha = 1$) or $n = 1$ ($\alpha = 3$) in these general expressions for friction force and torque, then the same expressions derived explicitley in Sec. 3.2.4 and Sec. 3.2.5, respectively, will be obtained.

# List of integrals

Below some solutions of integrals containing the trigonometric functions sin and cos are listed, which appeared in the calculations for the friction force and torque.

$$\int_0^{2\pi} \sin\varphi \mathrm{d}\varphi = 0, \quad \int_0^{2\pi} \cos\varphi \mathrm{d}\varphi = 0$$

$$\int_0^{2\pi} \sin^3\varphi \mathrm{d}\varphi = 0, \quad \int_0^{2\pi} \cos^2\varphi \mathrm{d}\varphi = 0$$

$$\int_0^{2\pi} \sin\varphi \cos^2\varphi \mathrm{d}\varphi = 0$$

$$\int_0^{2\pi} \sin\varphi \cos\varphi \mathrm{d}\varphi = 0$$

$$\int_0^{2\pi} \sin^2\varphi \mathrm{d}\varphi = \frac{1}{2}\varphi - \frac{1}{4}\sin 2\varphi \Big|_0^{2\pi} = \pi$$

# Appendix B

# Contents of CompactDisc

The enclosed CompactDisc contains movies in MPEG format. These movies show the dynamics of the corresponding selected simulations.

## Movies to Contact Dynamics simulations

Here are listed the movies obtained from the contact dynamics simulations of the uniaxial compaction of the ballistic deposit with 1015 spherical nano-particles (Chap. 4). Filenames ending with "_spheres.mpg" show solid spheres representing the nano-particles, while filenames ending with "_spheres_ctctF.mpg" show transparent spheres and the contact normal force network. The contact normal force network is represented by solid cylinders, which diameter represent the strength of the normal force. Red cylinders indicate repulsive forces, while blue cylinders indicate attractive forces. The corresponding normal forces were normalized to the mean repulsive and attractive force, respectively.

Four different pairs of ($\mu_{\mathrm{n}}$,$\mu_{\mathrm{t}}$) have been selected for the movies, while the other parameter values were fixed. For their values it is referred to Sec. 4.5.

- **mt_0_mn_0_spheres.mpg,**
  **mt_0_mn_0_spheres_ctctF.mpg:**
  The uniaxial compaction of the ballistic deposit with the following parameter values: $\mu_{\mathrm{t}} = 0.0,\ \mu_{\mathrm{n}} = 0.0$.

- **mt_1_mn_0_spheres.mpg,**
  **mt_1_mn_0_spheres_ctctF.mpg:**
  The uniaxial compaction of the ballistic deposit with the following parameter values: $\mu_t = 1.0,\ \mu_n = 0.0$.

- **mt_0_mn_1_spheres.mpg,**
  **mt_0_mn_1_spheres_ctctF.mpg:**
  The uniaxial compaction of the ballistic deposit with the following parameter values: $\mu_t = 0.0,\ \mu_n = 1.0$.

- **mt_1_mn_1_spheres.mpg,**
  **mt_1_mn_1_spheres_ctctF.mpg:**
  The uniaxial compaction of the ballistic deposit with the following parameter values: $\mu_t = 1.0,\ \mu_n = 1.0$.

# Movies on atomic-scale torsion friction

Here are listed the movies obtained from the molecular dynamics simulations of static atomic torsion friction (SEC. 5.3).

- **Tip_substrate_0.017.mpg:**
  On the atoms of the two top layers of the tip (red colored layers, see 5.1) a low external force value $0.017\epsilon/\sigma$ [1] was applied, so that the torsional rotation of the top layers is reversible: After switching off the external force the top layers rotate back to their initial position.

- **Tip_substrate_0.020.mpg:**
  On the atoms of the two top layers of the tip (red colored layers, see 5.1) an external force value of $0.020\epsilon/\sigma$ was applied, so that the torsional rotation of the top layers is irreversible: After switching off the external force the top layers do not rotate back to their initial position.

To follow the rotation of the tip more easily, one atom of each of the three different groups of tip-layers (red,green,blue colored atoms) was colored yellow.

[1] $\epsilon$ and $\sigma$ are the parameters of the Lennard-Jones potential and can be taken as energy ($\epsilon$) and length ($\sigma$) unit (see SEC. 5.3).

# Acknowledgments

At first, I want to express my gratitude to Prof. Dr. D.E. Wolf for giving me the possibility to work on the subjects of this thesis, for his support, inspiration and the many discussions on results and further steps.
I am very grateful to Tamás Unger for a fruitful collaboration and many illuminating and stimulating discussions.

I thank Dirk Kadau for the successful collaboration, good teamwork and being a humorous office mate.

Further, I thank Zeno Farkas for interesting discussions and helping me doing first steps in molecular dynamics simulations. Furthermore I want to thank Prof. Dr. J. Kertész, Tamás Unger, Sandor Fazekas, János Török (thanks for the delicious "kávé") for all the pleasant, interesting and successful stays as research guest in Budapest.

A special (and huge) thanks goes to Stephan Dammer: thanks for the good company ("XBlast") and many physics discussions not only during our physics courses and Ph.D. time.

I thank Dirk Kadau, Jochen Werth, Frank Westerhoff and Dominik Schwesig for being nice office mates and creating a comfortable working atmosphere (especially a cheerful one in work-filled times). Also I want to thank H. Beyer, Jochen Werth and Lothar Brendel for administrating our computer network and providing help at any time, H. Münstermann for help in bureaucratic questions and all the other collegues of the Comphys – Group.
Further I want to express my thanks and best wishes as well to all the non-mentioned.

This work was funded by the Graduate College 277 *Structure and Dynamics of Heterogenous Systems* of the German Research Foundation (DFG).

For careful proofreading of various parts of this work I am grateful to Kevin Johnson, Dirk Kadau, Tamás Unger and Lothar Brendel.

Finally, I want to thank Camilla and my family who showed constant interest, faith, support and patience during the long time of finishing this work.

# Bibliography


[1] B. N. J. Persson, *Sliding Friction of Lubricated Surfaces*, in Persson and Tosatti [5].

[2] B. Persson, *Sliding Friction*, Springer-Verlag Berlin Heidelberg New York, 2nd edn. 2000.

[3] E. Rabinowicz, *Friction and Wear of Materials*, Wiley, New York 1965.

[4] D. F. More, *Principles and Applications of Tribology*, Pergamon, London 1975.

[5] B. Persson and E. Tosatti, eds., *Physics of Sliding Friction*, NATO ASI Series, Series E: Applied Sciences - Vol. 311, Kluwer Acad. Publ., Dordrecht 1996.

[6] F. Bowden and D. Tabor, *The Friction and Lubrication of Solids*, Clarendon Press, Oxford 1964.

[7] I. Singer and H. Pollock, eds., *Fundamentals on Friction: Macroscopic and Microscopic Processes*, vol. 220 of *NATO ASI Series: Series E: Applied Sciences*, Kluwer Academic Publishers 1992.

[8] G. Binnig, C. Quate and C. Gerber, *Atomic Force Microscope*, Phys. Rev. Lett. **56**, 930 (1986).

[9] C. Fusco, *Friction and diffusion dynamics of adsorbates at surfaces*, Ph.D. thesis, University of Nijmegen, The Netherlands 2005.

[10] N. V. Brilliantov and T. Pöschel, *Rolling friction of a viscous sphere on a hard plane*, Europhys. Lett. **42**, 511–516 (1998).

[11] N. V. Brilliantov and T. Pöschel, *Rolling as a "continuing collision"*, Eur. Phys. J. B **12**, 299–301 (1999).

[12] Z. Farkas, G. Bartels, T. Unger and D. E. Wolf, *Frictional Coupling between Sliding and Spinning Motion*, Phys. Rev. Lett. **90**, 248302 (2003).

[13] D. Kadau, G. Bartels, L. Brendel and D. E. Wolf, *Contact Dynamics Simulations of Compacting Cohesive Granular Systems*, Comp. Phys. Comm. **147**, 190–193 (2002).

[14] D. Kadau, G. Bartels, L. Brendel and D. E. Wolf, *Pore Stabilization in Cohesive Granular Systems*, Phase Trans. **76**, 315–331 (2003).

[15] D. Kadau, *Porosität in kohäsiven granularen Pulvern und Nano-Pulvern*, Ph.D. thesis, University Duisburg-Essen 2003.

[16] *Nano-World Friction-Module*, World Wide Web Resource, URL: http://www.nano-world.org/frictionmodule/ (2005).

[17] *The MacTutor History of Mathematics archive*, World Wide Web Resource, URL: http://www-history.mcs.st-andrews.ac.uk/Mathematicians/Euler.html (2005).

[18] M. H. Müser, L. Wenning and M. O. Robbins, *Simple Microscopic Theory of Amontons's Laws for Static Friction*, Phys. Rev. Lett. **86**, 1295 (2001).

[19] C. A. Coulomb, *Théorie des machines simples en ayant égard au frottement de leurs parties et à la roideur des cordages*, Mémoires des mathématique et de physique présentés à l'Académie des Sciences (1781).

[20] *The MacTutor History of Mathematics archive*, World Wide Web Resource, URL: http://www-history.mcs.st-andrews.ac.uk/history/PictDisplay/Coulomb.html (2005).

[21] D. Dowson, *History of Tribology*, Longman, New York 1979.

[22] K. L. Johnson, *Contact Mechanics*, Cambridge University Press 1985.

[23] J. Greenwood, *Contact of Rough Surfaces*, in Singer and Pollock [7].

[24] F. Heslot, T. Baumberger, B. Perrin, B. Caroli and C. Caroli, *Creep, stick-slip, and dry-friction dynamics: Experiments and a heuristic model*, Phys. Rev. E **49**, 4973–4988 (1994).

[25] T. Baumberger, *Dry Friction at Low Velocities*, in Persson and Tosatti [5], 1–26.

[26] H. A. Stuart, *Kurzes Lehrbuch der Physik*, Springer 1992.

[27] K. Voyenli and E. Eriksen, *On the motion of an ice hockey puck*, American Journal of Physics **53**, 1149 (1985).

[28] S. Goyal, A. Ruina and J. Papadopoulos, *Planar sliding with dry friction. Part 1. Limit surface and moment function*, Wear **143**, 307–330 (1991).

[29] S. Goyal, A. Ruina and J. Papadopoulos, *Planar sliding with dry friction. Part 2. Dynamics of motion*, Wear **143**, 331–352 (1991).

[30] W. Huang. *On Performability Theory and the Inverse Sliding Problem*, Tech. Rep. CMU-RI-TR-94-05, Robotics Institute, Carnegie Mellon University, Pittsburgh, PA (March 1994).

[31] W. Huang, *Impulsive Manipulation*, Ph.D. thesis, Robotics Institute, Carnegie Mellon University, Pittsburgh, PA August 1997.

[32] S. Dahmen, Z. Farkas, H. Hinrichsen and D. E. Wolf, *Macroscopic diagnostics of microscopic friction phenomena*, Phys. Rev. E **71**, 066602 (2005).

[33] S. R. Dahmen, H. Hinrichsen, A. Lysov and D. E. Wolf, *Coupling between static friction force and torque for a tripod*, J. Stat. Mech. P03004 (March 2005).

[34] S. M. Rubinstein, G. Cohen and J. Fineberg, *Detachment fronts and the onset of dynamic friction*, Nature **430**, 1005 (2004).

[35] I. S. Gradshteyn and I. M. Ryzhik, *Table of Integrals, Series, and Products*, New York: Academic Press 1980.

[36] Silvio Dahmen, Private communication, 2005.

[37] I. N. Bronstein and K. A. Semendajew, *Taschenbuch der Mathematik*, Harri Deutsch, Frankfurt a. M. 1995.

[38] H. Kuchling, *Taschenbuch der Physik*, Fachbuchverlag, Leipzig - Köln 1995, 15., verbesserte Auflage.

[39] E. W. Weisstein, *"Autonomous."*, From MathWorld–A Wolfram Web Resource. http://mathworld.wolfram.com/Autonomous.html.

[40] W. H. Press, S. A. Teukolsky, W. T. Vetterling and B. P. Flannery, *Numerical Recipes in C - The Art of Scientific Computing*, Cambridge University Press 1992.

[41] L. D. Landau and E. M. Lifshitz, *Theory of Elasticity*, Pergamon Press, London 1959.

[42] P. M. Gerhart, R. J. Gross and J. I. Hochstein, *Fundamentals of Fluid Mechanics*, Addison-Wesley, Reading 1992.

[43] A. R. Penner, *The physics of sliding cylinders and curling rocks*, Am. J. Phys. **69**, 332–339 (2001).

[44] M. R. Shegelski and R. Holenstein, *Rapidly rotating sliding cylinders: Trajectories with large lateral displacements*, Can. J. Phys. **80** (2002).

[45] *Wikipedia, the free encyclopedia*, World Wide Web Resource, URL: http://en.wikipedia.org/wiki/Curling.

[46] E. Jensen and M. R. Shegelski, *The motion of curling rocks: Experimental investigation and semi-phenomenological description*, Can. J. Phys. **82**, 791–809 (2004).

[47] World Wide Web Resource. URL: www.seed.slb.com/en/scictr/watch/curling/.

[48] M. Mulvoy and E. Richardson, *Curling: Techniques and Strategy*, Lippincott, New York 1973.

[49] D. Wolf, *Modelling and Computer Simulation of Granular Media*, in *Computational Physics: Selected Methods - Simple Exercises - Serious Applications*, edited by K. Hoffmann and M. Schreiber, 64–94, Springer, Heidelberg 1996.

[50] H. Jaeger and S. Nagel, *Physics of the granular State*, Science **255**, 1523 (1992).

[51] E. R. Bagnold, *Physics of Blown Sand and Sand Dunes*, Chapman and Hall, London 1941.

[52] H. J. Herrmann, *Die wunderbare Welt der Schüttgüter*, Phys. Bl. **11**, 1083 (1995).

[53] M. Satake and J. T. Jenkins, eds., *Micromechanics of Granular Materials*, Elsevier, Amsterdam 1988.

[54] R. M. Nedderman, *Statics And Kinematics Of Granular Materials*, Cambridge University Press 1992.

[55] J. Duran, *Sands, Powders and Grains*, Springer, Berlin 2000.

[56] A. Metha, ed., *Granular Matter, An Interdisciplinary Approach*, Springer Verlag, New York 1994.

[57] D. Kolymbas, *Constitutive Modelling of Granular Materials*, Springer, Berlin 2000.

[58] T. Unger, *Characterization of static and dynamic structures in granular materials*, Ph.D. thesis, Budapest University of Technology and Economics, Hungary 2004.

[59] D. J. Hornbaker, R. Albert, I. Albert, A. L. Barabási and P. Schiffer, *Why sand castles stand: an experimental study of wet granular media*, Nature **387**, 765 (1997).

[60] P. Tegzes, R. Albert, M. Paskvan, A.-L. Barabasi, T. Vicsek and P. Schiffer, *Liquid-induced transitions in granular media*, Phys. Rev. E **60**, 5823 (1999).

[61] S. Ross and J. Morrison, *Colloidal Systems and Interfaces*, John Willey & Sons, New York 1988.

[62] J. R. Groza, *Nanosintering*, Nanostruc. Mat. **12**, 987–992 (1999).

[63] G. Skandan, H. Hahn, B. H. Kear, M. Roddy and W. H. Roddy, *The effect of applied stress on densification of nanostructured zirconia during sinter-forging*, Mat. Lett. **20**, 305 (1994).

[64] H. Hahn, *Unique Features and Properties of Nanostructured Materials*, Advanced Engineering Materials **5**, 277 (2003).

[65] M. K. Kennedy, F. E. Kruis and H. Fissan, *Gas phase synthesis of size selected $SnO_2$ nanoparticles for gas sensor applications*, Mater. Sci. Forum **343-346**, 949–954 (2003).

[66] M. K. Kennedy, F. E. Kruis, H. Fissan and B. R. Mehta, *A fully-automated gas-sensing and electronic parameter measurement setup for miniaturized nanoparticle gas sensors*, Rev. Sci. Instr. **74**, 4908 – 4915 (2003).

[67] S. Stappert, *Herstellung und Sinterung von gesputterten Nanopartikeln*, Master's thesis, Gerhard-Mercator-Universität Duisburg 2000.

[68] M. E. Cates, J. P. Wittmer, J. P. Bouchaud and P. Claudin, *Jamming, Force Chains, and Fragile Matter*, Phys. Rev. Lett. **81**, 1841 (1998).

[69] L. E. Silbert, D. Ertas, G. S. Grest, T. C. Halsey and D. Levine, *Geometry of frictionless and frictional sphere packings*, Phys. Rev. E **65**, 031304 (2002).

[70] H. A. Makse, J. Brujic and S. F. Edwards, *Statistical Mechanics of Jammed Matter*, in *The Physics of Granular Media*, edited by H. Hinrichsen and D. E. Wolf. Wiley-VCH, Weinheim 2004.

[71] J. B. Knight, C. G. Fandrich, C. N. Lau, H. M. Jaeger and S. R. Nagel, *Density relaxation in a vibrated granular material*, Phys. Rev. E **51**, 3957–3963 (1995).

[72] E. Caglioti, V. Loreto, H. J. Herrmann and M. Nicodemi, *A "Tetris-Like" Model for the Compaction of Dry Granular Media*, Phys. Rev. Lett. **79**, 1575 (1997).

[73] T. Unger and J. Kertész, *The Contact Dynamics Method for Granular Media*, in *Modeling of Complex Systems*, 116–138, American Institute of Physics, Melville, New York 2003, cond-mat/0211696.

[74] G. Barker, *Computer Simulations of Granular Materials*, in Metha [84].

[75] S. McNamara and W. R. Young, *Inelastic collapse in two dimensions*, Phys. Rev. E **50** (1994).

[76] P. Cundall and O. Strack, *A discrete model for granular assemblies*, Geotechnique **29**, 47–65 (1979).

[77] J. Moreau and P. Panagiotopoulos, eds., *Nonsmooth Mechanics and Applications*, vol. 302 of *CISM Courses and Lectures*, Springer-Verlag, Wien, New York 1988.

[78] M. Jean and J. J. Moreau, *Unilaterality and dry friction in the dynamics of rigid body collections*, in *Proceedings of Contact Mechanics International Symposium*, 31–48, Presses Polytechniques et Universitaires Romandes, Lausanne, Switzerland 1992.

[79] M. Jean, *The non-smooth contact dynamics method*, Comput. Methods Appl. Engrg. **177**, 235–257 (1999).

[80] S. Luding, E. Clément, A. Blumen, J. Rajchenbach and J. Duran, *Studies of columns of beads under external vibrations*, Phys. Rev. E **49**, 1634 (1994).

[81] A. Karolyi and J. Kertesz, *Granular medium lattice gas model: the algorithm*, Comput. Phys. Commun. **121-122**, 290–293 (1999).

[82] D. Volk, G. Baumann, D. E. Wolf, G. Törner and M. Schreckenberg, *Simulating Granular Media Using Cellular Automata*, in *Traffic and Granular Flow '97*, edited by M. Schreckenberg and D. E. Wolf, 145–150, Springer, Singapur 1998.

[83] S. B. Savage, *Modeling and Granular Material Boundary Value Problems*, NATO ASI Series, Series E: Applied Sciences - Vol. 350, Kluwer Acad. Publ., Dordrecht 1998.

[84] A. Metha, ed., *Granular Matter, An Interdisciplinary Approach*, Springer Verlag, New York 1994.

[85] P. Lötstedt, *Coulomb friction in two dimensional rigid body systems*, Z. f. Angewandte Math. und Mech. **61**, 605–615 (1981).

[86] P. Lötstedt, *Mechanical systems of rigid bodies subject to unilateral constraints*, SIAM J. Appl. Math. **42**, 281–296 (1982).

[87] J. Moreau, *Some numerical methods in multibody dynamics: application to granular materials*, Eur J Mech, A/Solids **13**, 93–114 (1994).

[88] F.Radjai, D. Wolf, S. Roux, M. Jean and J. Moreau, *Force Networks in Granular Packings*, in *Friction, Arching, Contact Dynamics*, edited by D. E. Wolf and P. Grassberger, World Scientific Publishing Co. Pte. Ltd., Singapore 1997.

[89] F. Radjai and D. E. Wolf, *Features of static pressure in dense granular media*, in *Granular Matter*, vol. 1, 3–8. Springer-Verlag 1998.

[90] F. Radjai, D. E. Wolf, M. Jean and J. J. Moreau, *Bimodal Character of Stress Transmission in Granular Packings*, Phys. Rev. Lett. **80**, 61 (1998).

[91] F. Radjai, M. Jean, J. J. Moreau and S. Roux, *Force Distribution in Dense Two-Dimensional Granular Systems*, Phys. Rev. Lett. **77**, 274 (1996).

[92] F. Radjai, *Multicontact dynamics of granular Systems*, Computer Physics Communications **121-122**, 294–298 (1999).

[93] T. Unger, L. Brendel, D. E. Wolf and J. Kertész, *Elastic behavior in Contact Dynamics of rigid particles*, Phys. Rev. E **65** (2002).

[94] G. Bartels, *Die Kontakt-Dynamik Methode: Konvergenzkriterien und eine Anwendung*, Master's thesis, Gerhard-Mercator Universität Duisburg 2001.

[95] F. Radjai, L. Brendel and S. Roux, *Nonsmoothness, indeterminacy, and friction in two dimensional arrays of rigid particles*, Phys. Rev. E **54**, 861 (1996).

[96] D. E. W. L. Brendel, T. Unger, *The Physics of Granular Media* 325–343 (2004).

[97] F. Radjai, S. Roux and J. J. Moreau, *Contact forces in a granular packing*, Chaos **9**, 544–550 (1999).

[98] M. Krafczyk, P. Lehmann, O. Filippova, D. Hänel and U. Lantermann, *Lattice Boltzmann Simulations of Complex Multiphase Flows*, in *Multifield Problems*, 50–57, Springer, Berlin 2000.

[99] O. Filippova and D. Hänel, *Lattice Boltzmann Simulations of Gas-Particle Flow in Filters*, Comp. and Fluids **26**, 697–712 (1997).

[100] R. Jullien and P. Meakin, *Simple Three-Dimensional Models for Ballistic Deposition with Restructuring*, Europhys. Lett. **4**, 1385–1390 (1987).

[101] P. Meakin and R. Jullien, *Ballistic deposition with sticky and non-sticky particles*, Physica A **175**, 211–221 (1991).

[102] J. Christoffersen, M. M. Mehrabadi and S. Nemat-Nasser, *A micromechanical description of granular material behavior*, J. Appl. Mech. **48**, 339 (1981).

[103] T. Unger and Z. Farkas, Private communication, (2005).

[104] K. Johnson, D. Kadau and D. E. Wolf, *Simulation of three dimensional cohesive powder compaction* (2005), In Preparation.

[105] K. Johnson, Private communication, (2005).

[106] L. Brendel, Private communication, (2005).

[107] C. M. Mate, G. M. McClelland, R. Erlandsson and S. Chiang, *Atomic-scale friction of a tungsten tip on a graphite surface*, Phys. Rev. Lett. **59**, 1942–1945 (1987).

[108] E. Gnecco, R. Bennewitz, T. Gyalog, C. Loppacher, M. Bammerlin, E. Meyer and H.-J. Güntherodt, *Velocity Dependence of Atomic Friction*, Phys. Rev. Lett. **84** (2000).

[109] H. Ibach and H. Lüth, *Festkörperphysik: Einführung in die Grundlagen*, Springer 1999.

[110] R. Bennewitz, T. Gyalog, M. Guggisberg, M. Bammerling, E. Meyer and H. Güntherodt, *Atomic-scale stick-slip processes on Cu(111)*, Phys. Rev. B **60**, R11 301 (1999).

[111] U. Landman, W. Luedtke and M. Ribarsky, J. Vac. Sci. Technol. A **7**, 2829 (1989).

[112] U. Landman, W. D. Luedtke and J. Gao, *Atomic-Scale Issues in Tribology: Interfacial Junctions and Nano-elastohydrodynamics*, Langmuir **12**, 4514–4528 (1996).

[113] J. Nieminen, A. Sutton and J. Pethica, Acta Metall. Mater. **40**, 2503 (1992).

[114] M. R. Sørensen, K. W. Jacobsen and P. Stoltze, *Simulations of atomic-scale sliding friction*, Phys. Rev. B **53**, 2101–2113 (1996).

[115] E. Gnecco, R. Bennewitz, T. Gyalog and E. Meyer, *Friction experiments on the nanometre scale*, J. Phys.: Condens. Matter **13**, R619–R642 (2001), Topical Review.

[116] R. Haberlandt, S. Fritzsche, G. Peinel and K. Heinzinger, *Molekulardynamik - Grundlagen und Anwendungen*, Vieweg, Braunschweig 1995.

[117] M. Allen and D. Tildesley, *Computer Simulation of Liquids*, Clarendon Press, Oxford 1987.

[118] K. Kadau, *Molekulardynamik-Simulationen von strukturellen Phasenumwandlungen in Festköpern, Nanopartikeln und ultradünnen Filmen*, Ph.D. thesis, Gehard-Mercator-Universität Duisburg 2001.

[119] D. J. Evans and B. L. Holian, *The Nosé-Hoover thermostat*, J. Chem. Phys. **83**, 4069–4074 (1985).

# Curriculum vitae

## Persönliche Daten

| | |
|---|---|
| Name: | Guido Bartels |
| Geburtsdatum: | 18.09.1974 |
| Geburtstort: | Moers |

## Schulbildung und Ersatzdienst

| | |
|---|---|
| 1981 – 1985 | Gemeinschaftsgrundschule Van-Gogh-Straße, Duisburg-Rheinhausen |
| 1985 – 1994 | Krupp-Gymnasium, Duisburg-Rheinhausen, Abschluss Abitur |
| 1994 – 1995 | Zivildienst |

## Hochschulstudium

| | |
|---|---|
| 1995 – 2001 | Physikstudium an der Gerhard-Mercator-Universität - Gesamthochschule Duisburg |
| Mai 2001 | Abschluss des Studiums als Diplom-Physiker<br>Thema der Diplomarbeit:<br>*Die Kontakt-Dynamik Methode: Konvergenzkriterien und eine Anwendung* |
| seit Juni 2001 | Promotionsstudium Physik an der Gerhard-Mercator-Universität Duisburg (bis Ende 2002) bzw. Universität Duisburg-Essen (ab 2003) |

Duisburg, 29. September 2005

# Publications

## Journal Articles

- *The effect of contact torques on porosity of cohesive powders*
  G. Bartels, T. Unger, D. Kadau , D. E. Wolf and J. Kertész
  Granular Matter, **7**, 139-143, (2005)

- *Frictional Coupling between Sliding and Spinning Motion*
  Z. Farkas, G. Bartels, T. Unger and D. E. Wolf
  Phys. Rev. Lett., **90**, 248302, (2003)

- *Pore Stabilization in Cohesive Granular Systems*
  D. Kadau, G. Bartels, L. Brendel and D. E. Wolf
  Phase Trans., **76**, 315-331, (2003)

- *Macroscopic and Microscopic Investigation on the History Dependence of the Mechanical Properties of Powders*
  D. Kadau, L. Brendel, G. Bartels, D. E. Wolf,
  M. Morgeneyer and J. Schwedes
  Chemical Engineering Transactions, **3**, 979-984, (2003)

- *Contact Dynamics Simulations of Compacting Cohesive Granular Systems*
  D. Kadau, G. Bartels, L. Brendel and D. E. Wolf
  Comp. Phys. Comm., **147**, 190-193, (2002)

# Presentations

- *Influence of gravity on the Compaction of Granular Materials*, G. Bartels, D. Kadau, L. Brendel and D.E. Wolf, Press Curing: 1st Annual Report Meeting, Duisburg, Germany, September 2000 (Oral).

- *Contact Dynamics Simulations of Compacting Cohesive Granular Systems*, D. Kadau, G. Bartels, L. Brendel and D. E. Wolf, Conference on Computational Physics 2001 (CCP2001), Aachen, Germany, September 2001 (Poster)

- *Role of Torsionmoments at Particle-Contact in Nano-powders*, G. Bartels, T. Unger, D. Kadau and D.E. Wolf, DPG Spring Meeting 2003, Dresden, Germany, March 2003 (Poster).

- *Solid Friction: Force and Torque, Static and Dynamic*, G. Bartels, S. Dahmen, Z. Farkas, T. Unger and D.E. Wolf, International Symposium on Structure and Dynamics of Heterogenous Systems - SDHS'03, Duisburg, Germany, November 2003 (Poster).

- *Static Friction on Atomic Scale*, G. Bartels and D.E. Wolf, Press Curing: 3rd Annual Report Meeting, Duisburg, Germany, March 2004 (Oral).

- *Dry Solid Friction: Force and Torque, Static and Dynamic*, G. Bartels, S. Dahmen, Z. Farkas and D.E. Wolf, International Workshop of SFB 616 *Energy dissipation at surfaces*, Wesseling, Germany, September 2004 (Poster).

- *Molecular Dynamics Simulations of Atomic Scale Friction*, G.Bartels and D.E. Wolf, Groupseminar of AG Prof. Möller, Essen, Germany, Dezember 2004 (Oral).

- *Theorie und Computersimulation von Reibungsphänomen*, G. Bartels, C. Fusco and D.E. Wolf, Assessement of SFB 616 *Energy dissipation at surfaces*, Duisburg, Germany, April 2005 (Poster).